Autophagy in motion: neuronal activity and behavior guide long-distance autophagic vesicle transport in *Locus coeruleus* axons projecting to the prefrontal cortex

Thesis

for the degree of

Doktor rerum naturalium
(Dr. rer. nat.)

approved by the Faculty of Natural Sciences of Otto von Guericke
University Magdeburg

by: M.Sc. Ahmed Adel Ahmed Aly
Born on 06 -10-1995 in Cairo (Egypt)

Examiners: **Prof. Dr. rer. nat. Constanze Seidenbecher**
Prof. Dr. rer. nat. habil. Natalia Kononenko

Submitted on 18/03/2025
Defended on 06/11/2025

Aly, Ahmed
Autophagy in motion: neuronal activity and behavior guide long-distance autophagic vesicle transport in Locus coeruleus axons projecting to the prefrontal cortex
Dissertation, Fakultät für Naturwissenschaften
Otto-von-Guencke-Universität Magdeburg

Table of Contents

Summary

Autophagy is a complex intracellular process that enables cells to sequester damaged proteins, toxic metabolic byproducts, and other cellular components for subsequent degradation or recycling. Its efficiency is particularly crucial for neurons, which are required to function throughout the entire lifespan of an organism. In fact, insufficient autophagy is frequently associated with neurodegeneration in context of both disease and aging.

Noradrenergic neurons of the *locus coeruleus (LC-NE)* are exceptionally vulnerable to degeneration, and both the endo-lysosomal system and autophagy pathways play a role in eliminating polymerized catecholamine derivatives. Moreover, the *LC-NE* is among the first brain regions affected by the accumulation of beta-amyloid deposits, resulting in Alzheimer`s disease. *LC-NE* neurons extend long, extensively branched axons throughout the brain, and their reliance on volume transmission suggests that presynaptic regulatory mechanisms, particularly those involving adrenergic G-protein-coupled receptors, govern autophagic vesicle (AV) trafficking in *LC-NE* axons to ensure timely cargo degradation. Interestingly, a tightly regulated exchange of membranous compartments between adjacent neuronal populations, specifically the *LC-NE* and the *(Me5) neurons*, has been suggested preventing *LC-NE* neurodegeneration.

My thesis explores network-related cellular mechanisms regulating neuronal proteostasis in the *locus coeruleus* via autophagy. Using state-of-the-art technologies like *in vivo* imaging and *in vivo* fiber-mediated photoconversion I investigated two key aspects of autophagy regulation in noradrenergic axons: (1) how neuronal activity, behavior, and norepinephrine release influence the trafficking pattern and velocity of autophagic vesicles in distal axons; (2) the role of the endo-lysosomal system and autophagy in cargo disposal within the somato-dendritic region of the *LC-NE* .

I found that during their navigation through the distal *LC* axons projecting to the PFC, AVs exhibit distinct trafficking velocities and directions *in vivo* under conditions of spontaneous *LC-NE* activity. These AVs can be categorized into three distinct populations: (i) slow bidirectional, (ii) fast bidirectional, and (iii) slow unidirectional. Next, I found that the chemogenetic inhibition of *LC-NE* activity unifies the trafficking directionality of LC3B-positive vesicles, promoting a shift from bidirectional to unidirectional motility within *LC-NE* axons projecting to the *PFC in vivo*. Inhibition changes the representation of distinct populations of autophagic vesicles classified as (i) slow unidirectional, (ii) fast unidirectional, and (iii) extra fast unidirectional.

Using optical fiber-mediated photoconversion of mEos4-LC3B at the distal axons targeting the *PFC*, I observed photoconverted "red" LC3B-positive puncta in the somata of *LC-NE* neurons. This suggests that the shift in directionality from anterograde to retrograde is associated with the delivery of autophagic vesicles to the cell soma of *LC-NE* neurons. Additionally, mEos4-LC3B vesicles were SIPA1L2-positive, suggesting that LC3B+ vesicles are amphisomes - hybrid organelles on the autophagy pathway. Conversely, stimulation of *LC-NE* activity through stress-induced behavior, mimicked by exposure to a novel environment, altered AV trafficking by reducing the number of AVs reaching the cell soma from distal axons projecting to the *PFC*.

By employing LC-NE-specific labeling, I found that β2ARs are presynaptically expressed at distal LC axons projecting to the PFC. To elucidate whether AV trafficking is regulated by an autocrine mechanism and to identify the temporal correlations between AV trafficking

patterns, such as stopovers and mobilizations, and NE release, an innovative NE sensor (GRABNE2h) was employed alongside a fluorescent AV marker (mRuby3-LC3). The findings revealed that AV trafficking initiation follows a significant reduction in NE release, whereas mobile AVs tend to pause when NE levels increase at the imaged distal axon.

The investigation into molecular mechanisms of AV motility regulation reveals that Spinophilin, a regulatory subunit of PP1, associates with both, SIPA1L2 and dynein adaptor Snapin, and might provide local regulation for Snapin dephosphorylation, facilitating its reassociation with motor complex and subsequent vesicle mobilization.

I identified previously overlooked, significant differences in lysosomal machinery between tyrosine hydroxylase-positive neurons of the *LC-NE* and neighboring mesencephalic trigeminal neurons *(Me5).* The levels for the autophagy receptor p62 are also differentially regulated across these neuronal nuclei. *LC-NE*-specific viral transduction with the mRuby3-LC3B autophagy marker revealed the presence of mRuby3-LC3B puncta within the adjacent *Me5* somata. My findings suggest a functional interplay between these neuronal populations, indicating that *LC-NE* neurons may utilize secretory autophagy as an alternative pathway for cargo disposal when their intrinsic degradative capacity is compromized. Finally, I found that under *LC-NE* inactivation, Sec22b puncta, a marker for secretory autophagy, were scarcely detectable. These findings support the notion that the activity state of *LC-NE* neurons may regulate secretory autophagy and membrane exchange between *LC-NE* and *Me5* neurons. Thus, *Me5* neurons may facilitate the clearance of damaged proteins and metabolites from *LC-NE* neurons, highlighting a potential **cooperative mechanism** in maintaining neuronal proteostasis.

Overall, my results indicate the *LC-NE* employ a different logistics for the trafficking of autophagic vesicles for somatic delivery at diverse activity states, regulated by the autocrine mechanism. Retrograde transport and AV velocities appeared to be enhanced during *LC-NE* inactivation, potentially reflecting REM sleep conditions, during which AVs exhibit increased velocity in reaching the somata. The suggested molecular mechanism for mobilization might involve Spinophilin and PP1-mediated effect of Snapin dephosphorylation, requiring reassociation with the dynein motor. A cell-to-cell communication between *LC-NE* and *Me5* might serve as a compensatory system providing digestive assistance for highly demanding neurons such as *LC-NE.*

Zusammenfassung:

Autophagie ist ein komplexer intrazellulärer Prozess, der es Zellen ermöglicht, beschädigte Proteine, toxische Stoffwechselnebenprodukte und andere zelluläre Bestandteile zu isolieren, um sie anschließend abzubauen oder zu recyceln. Seine Effizienz ist besonders entscheidend für Neuronen, die während der gesamten Lebensdauer eines Organismus funktionsfähig bleiben müssen. Tatsächlich wird eine unzureichende Autophagie häufig mit Neurodegeneration im Zusammenhang mit Krankheiten als auch mit dem Alterungsprozess in Verbindung gebracht.

Noradrenerge Neuronen des *Locus coeruleus (LC-NE)* sind außergewöhnlich anfällig für Degeneration, wobei sowohl das endo-lysosomale System als auch Autophagie-wege eine Rolle beim Abbau polymerisierter Katecholamin-Derivate spielen. Darüber hinaus gehört der *LC* zu den ersten Hirnregionen, die von der Akkumulation von Beta-Amyloid-Ablagerungen betroffen sind, was zur Alzheimer-Krankheit führt. *LC-NE*-Neuronen projizieren lange, stark verzweigte Axone in das gesamte Gehirn, und ihre Wirkung über Volumenübertragung legt nahe, dass präsynaptische Regulationsmechanismen – insbesondere jene, die adrenerge G-Protein-gekoppelte Rezeptoren einbeziehen – den Transport autophagischer Vesikel (AV) in *LC-NE*-Axonen steuern, um einen zeitgerechten Cargo-Abbau sicherzustellen. Interessanterweise wurde ein streng regulierter Austausch membranöser Kompartimente zwischen benachbarten Neuronenpopulationen, speziell zwischen dem LC-NE und dem mesenzephalen Trigeminuskern *(Me5),* als Mechanismus vorgeschlagen, der einer LC-NE-Neurodegeneration vorbeugen könnte. Meine Dissertation untersucht netzwerkbezogene zelluläre Mechanismen, die die neuronale Proteostase im Locus coeruleus über Autophagie regulieren.

Mithilfe modernster Technologien wie In-vivo-Bildgebung und in-vivo faservermittelter Photokonversion habe ich zwei zentrale Aspekte der Autophagieregulation in noradrenergen Axonen untersucht: Wie neuronale Aktivität, Verhalten und Noradrenalinfreisetzung das Transportmuster und die Geschwindigkeit autophagischer Vesikel in distalen Axonen beeinflussen, und die Rolle des endo-lysosomalen Systems und der Autophagie beim Cargo-Abbau im somato-dendritischen Bereich des *LC-NE*. Ich stellte fest, dass AVs während ihrer Navigation durch die distalen *LC*-Axonen, die zum präfrontalen Kortex (*PFC*) projizieren, in vivo unter Bedingungen spontaner *LC-NE*-Aktivität unterschiedliche Transportgeschwindigkeiten und -richtungen aufweisen. Diese AVs können in drei unterschiedliche Populationen eingeteilt werden: (i) langsam bidirektional, (ii) schnell bidirektional und (iii) langsam unidirektional. Weiterhin ergab sich, dass die chemogenetische Hemmung der *LC-NE*-Aktivität die Transportrichtungs-bestimmung der LC3B-positiven Vesikel vereinheitlicht, indem sie einen Wechsel von bidirektionaler zu unidirektionaler Motilität innerhalb der *LC-NE*-Axonen, die zum *PFC* projizieren, in vivo fördert. Unter der Hemmung verhalten sich die Populationen autophagischer Vesikel als (i) langsam unidirektional, (ii) schnell unidirektional und (iii) extra schnell unidirektional. Mithilfe der optischen faservermittelten Photokonversion von mEos4-LC3B in den distalen Axonen, die den PFC erreichen, beobachtete ich photokonvertierte „rote" LC3B$^+$ Punkta in den Zellkörpern der *LC-NE*-Neuronen. Dies legt nahe, dass der Richtungswechsel von anterograd zu retrograd mit dem Transport autophagischer Vesikel in den Zellkörper der LC-NE-Neuronen verbunden ist. Zusätzlich waren mEos4-LC3B-Vesikel SIPA1L2-positiv, was darauf hindeutet, dass sie Amphisomen – hybride Organellen des Autophagiewegs – darstellen. Im

Gegensatz dazu führte die Stimulation der *LC-NE*-Aktivität durch stressinduziertes Verhalten, simuliert durch die Exposition in einer neuartigen Umgebung, zu einer veränderten AV-Trafficking-Dynamik, indem die Anzahl der AVs, die von distalen Axonen zum PFC den Zellkörper erreichen, reduziert wurde. Durch *LC-NE*-spezifische Markierung stellte ich fest, dass β2ARs präsynaptisch in den distalen LC-Axonen, die zum PFC projizieren, exprimiert werden. Um zu klären, ob das AV-Trafficking durch einen autokrinen Mechanismus reguliert wird und um die zeitlichen Zusammenhänge zwischen AV-Trafficking-Mustern – wie Zwischenstopps und Mobilisierungen – und der Noradrenalinfreisetzung zu identifizieren, setzte ich einen innovativen Noradrenalin-Sensor (GRABNE2h) zusammen mit einem fluoreszierenden AV-Marker (mRuby3-LC3) ein. Die Ergebnisse zeigten, dass die Initiierung des AV-Traffickings einer signifikanten Reduktion der Noradrenalinfreisetzung folgt, während mobile AVs dazu neigen, anzuhalten, wenn die Noradrenalinspiegel im distalen Axon ansteigen. Die Untersuchung der molekularen Mechanismen der Regulation der AV-Motilität ergab, dass Spinophilin, eine regulatorische Untereinheit von PP1, sowohl mit SIPA1L2 als auch mit dem Dynein-Adaptor Snapin assoziiert und möglicherweise eine lokale Regulation der Snapin-Dephosphorylierung ermöglicht, wodurch dessen erneute Assoziation mit dem Motorkomplex und die anschließende Vesikelmobilisierung erleichtert wird. Ich identifizierte bislang übersehene, signifikante Unterschiede in der lysosomalen Maschinerie zwischen Tyrosinhydroxylase-positiven Neuronen des *LC-NE* und benachbarten *Me5* Neuronen. Auch die Spiegel des Autophagie-Rezeptors p62 sind in diesen neuronalen Kernen unterschiedlich reguliert. Durch *LC-NE*-spezifische virale Transduktion mit dem mRuby3-LC3B-Autophagie-Marker zeigte ich mRuby3-LC3B-Punkta in den benachbarten Me5-Zellkörpern. Meine Ergebnisse deuten auf ein funktionelles Zusammenspiel zwischen diesen Neuronenpopulationen hin, d.h. dass *LC-NE*-Neuronen sekretorische Autophagie als alternativen Weg zur Frachtentsorgung nutzen könnten, wenn ihre intrinsische Abbaukapazität beeinträchtigt ist. Schließlich fand ich, dass unter *LC-NE*-Inaktivierung Sec22b-Punkta, ein Marker für sekretorische Autophagie, kaum nachweisbar waren. Diese Befunde stützen die Annahme, dass der Aktivitätszustand der *LC-NE*-Neuronen die sekretorische Autophagie und den Membranaustausch zwischen *LC-NE*- und *Me5*-Neuronen regulieren könnte.

Daher könnten *Me5*-Neuronen den Abbau beschädigter Proteine und Metaboliten aus *LC-NE*-Neuronen erleichtern und damit einen potenziellen kooperativen Mechanismus zur Aufrechterhaltung der neuronalen Proteostase darstellen. Insgesamt deuten meine Ergebnisse darauf hin, dass *LC-NE*-Neuronen unterschiedliche Logistikstrategien für den Transport autophagischer Vesikel zur somatischen Cargo-Entsorgung bei unterschiedlichen Aktivitätszuständen anwenden, die durch einen autokrinen Mechanismus reguliert werden. Der retrograde Transport und die Geschwindigkeiten der AVs scheinen unter *LC-NE*-Inaktivierung erhöht zu sein, was möglicherweise REM-Schlafbedingungen widerspiegelt, während derer AVs mit erhöhter Geschwindigkeit die Zellkörper erreichen. Der molekulare Mechanismus für die Mobilisierung könnte den Spinophilin- und PP1-vermittelten Effekt der Snapin-Dephosphorylierung beinhalten, der für die erneute Assoziation mit dem Dynein-Motor erforderlich ist. Die Zell-Zell-Kommunikation zwischen *LC-NE* und *Me5* könnte als kompensatorisches System dienen, um stark beanspruchte Neuronen wie *LC-NE* zu unterstützen.

1. Introduction

1.1. Neuronal autophagy

1.1.1. Diverse forms of autophagy and their interplay in neuronal function and proteostasis

A complex cellular process that encompasses the sequestration of damaged proteins, toxic metabolic byproducts, and other intracellular components, including protein aggregates and dysfunctional organelles, for targeted degradation and recycling is collectively termed ''Autophagy,'' a term derived from the Greek words ''auto'' (self) and ''phagy'' (to eat), signifying ''self-eating.''

Autophagy is required in neurodevelopment as well as in the maintenance of neuronal homeostasis (Stavoe and Holzbaur, 2019). As such, autophagy represents a highly organized cellular clearance mechanism, and its efficiency is particularly critical for neurons, which must sustain functionality throughout the organism's entire lifespan due to their post-mitotic nature.

The post-mitotic nature of neurons, unlike dividing cells, makes them particularly susceptible to the accumulation of protein aggregates, as they cannot dilute these aggregates through cell division. This inability leads to the accumulation of aggregates in both neurites and the neuronal soma (Hara et al., 2006; Komatsu et al., 2006; Komatsu et al., 2007; Menzies et al., 2017). Additionally neurons present a unique array of challenges, including high metabolic demands (e.g., Harris et al., 2012) and elevated membrane turnover due to the continuous release and recycling of synaptic vesicles - features not shared by any other cell type. Consequently, autophagy becomes indispensable for the efficient regulation of neuronal proteostasis and this necessity is particularly pronounced in the presynaptic compartment, where the lifespan of presynaptic proteins varies significantly, with half-lives ranging from a few hours to several days (Hakim et al., 2016; Fornasiero et al., 2018; Cohen and Ziv, 2019). These timeframes are remarkably short compared to the overall lifespan of neurons and synapses, therefore, the replacement of presynaptic proteins must occur in a highly specific and tightly coordinated manner (Gundelfinger et al., 2022). In fact, insufficient autophagy is frequently associated with neurodegeneration in context of both disease and aging (Nixon, 2013; Nixon & Rubinsztein, 2024).

Three main degradative systems regulate synaptic proteome turnover: the ubiquitin-proteasome system (UPS) (Rinetti and Schweizer, 2010; Lazarevic et al., 2011; Waites et al., 2013; Cohen and Ziv, 2017; Soykan et al., 2021), the endo-lysosomal pathway, and autophagy-related mechanisms, which function through degradative membranous organelles (Azarnia Tehran et al., 2018; Lie & Nixon 2018, Winckler et al. 2018; Jin et al., 2018; Boecker and Holzbaur, 2019; Kuijpers et al., 2020; Lieberman and Sulzer, 2020; Andres-Alonso et al., 2021; Soykan et al., 2021; *Fig. 1a*). Several autophagic degradative pathways, which utilize lysosomal hydrolases to degrade proteins and other cellular constituents, can operate in parallel. These pathways include **macroautophagy**, commonly referred to simply as autophagy (delivery of cytosolic contents to the lysosome by autophagosomes), **microautophagy** (inward invagination of the lysosomal membrane) and **chaperone-mediated autophagy**, shortly **CMA** (direct translocation across the lysosomal membrane) (Mizushima & Levine, 2010; Stavoe and Holzbaur, 2019). Another emerging function of neuronal autophagy is the secretion of specific cargo into the extracellular milieu, a process known as **secretory autophagy** (Dupont, et al., 2011; Kim et al., 2021; Nakamura, et al., 2024; Hutchings et al., 2024; Hartmann et al., 2024; Tan et al., 2022; Martinelli et al., 2021; Chang, et al., 2024).

Iriguingly, evidences suggest proteolytic crosstalk between the ubiquitin-proteasome system, endo-lysosomal degradation, and autophagy at the synapse (*Fig. 1b*). For instance, the giant active zone scaffolding protein Bassoon (Bsn) appears to play a pivotal role in the coordination of degradative pathways at the synapse, interacting with components of both the proteasomal and autophagosomal systems (*Fig. 1b*) (Okerlund et al., 2017).

Macroautophagy is an evolutionarily conserved degradation and recycling process utilized by various cell types, including neurons and glial cells, to deliver cytoplasmic contents such as toxic or defective proteins and organelles to lysosomes for degradation (Mizushima & Komatsu, 2011; Lee et al., 2013; Dikic & Elazar, 2018; Stavoe & Holzbaur, 2019; Nishimura & Tooze, 2020; Zhao & Zhang, 2019; Aman et al., 2021; Gundelfinger et al., 2022; Diao et al., 2024). It is characterized by the sequestration of cytoplasmic substrates within endomembranes, followed by the formation of cytosolic double-membrane vesicles known as autophagosomes (*Fig. 2*).

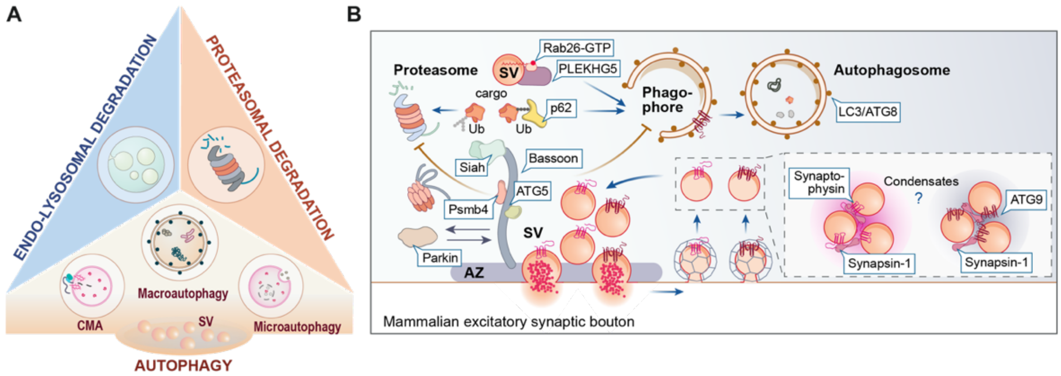

Figure 1| Proteolytic crosstalk between the ubiquitin-proteasome system, endo-lysosomal degradation and autophagy at the synapse

(A) The primary degradative pathways at the presynapse include proteasomal degradation via the UPS, endo-lysosomal degradation (Korolchuk, et al., 2010) and various forms of autophagy, such as macroautophagy, microautophagy and chaperone-mediated autophagy (CMA) as revealed by proteomic analyses (Weingarten et al., 2014; van Oostrum, et al., 2023). (B). Bassoon associates with ATG5 and the proteasome subunit Psmb4, while also interacting with the ubiquitin (Ub) E3 ligase Siah1 and functionally engaging with Parkin-mediated degradation pathways. Furthermore, entire organelles, such as synaptic vesicles, can be targeted to the phagophore through the action of the small GTPase Rab26 and its guanine nucleotide exchange factor, PLEKHG5. Synaptic vesicles and ATG9-positive vesicles exhibit similar morphology and share exo-endocytosis pathways but are distinct organelles. Their segregation at the perisynaptic endocytic zone may be mediated by liquid-phase separation, as the SV protein synaptophysin and ATG9 are capable of forming separate condensates with synapsin (Choi et al., 2024). "SV" refer to synaptic vesicles. The figure is adapted from Gundelfinger et al. 2022; Karpova et al., 2025).

This process is subsequently followed by complex vesicular fusion with lysosomes, ensuring the timely degradation of the sequestered material. Macroautophagy operates in both bulk and selective modes via autophagy adaptors, also known as receptors (Andrea K et al. 2019). Selective autophagy pathways, such as ER-phagy, aggrephagy, mitophagy, pexophagy, exophagy and potentially others, engage selective autophagy receptors (SARs) which recognize and bind to specific cellular cargo (reviewed in Ming-Yue Wu, et al., 2024).

Microautophagy involves the direct engulfment of cellular components by the lysosome through membrane invagination (Wang et al., 2022; Oliver Schmidt, David Teis 2012). The endosomal sorting complexes required for transport (ESCRT) complex is the best-characterized example of a membrane deformation or invagination process involved in the formation of multivesicular bodies (MVBs) and intraluminal vesicles (ILVs), which, in turn, play a key role in endocytic degradation and endosomal microautophagy (Yoshihiko & Tomohiko 2024).

CMA is a more selective type of microautophagy where KFERQ-like motifs containing proteins are targeted and transported directly across the lysosomal membrane via the chaperone Hsc70/HSPA8 (*Fig. 2*) and its co-chaperones, such as the carboxyl terminus of Hsc70-interacting protein (CHIP), heat shock protein 40 (Hsp40, also known as DNABJ1), and Hsp70-Hsp90.

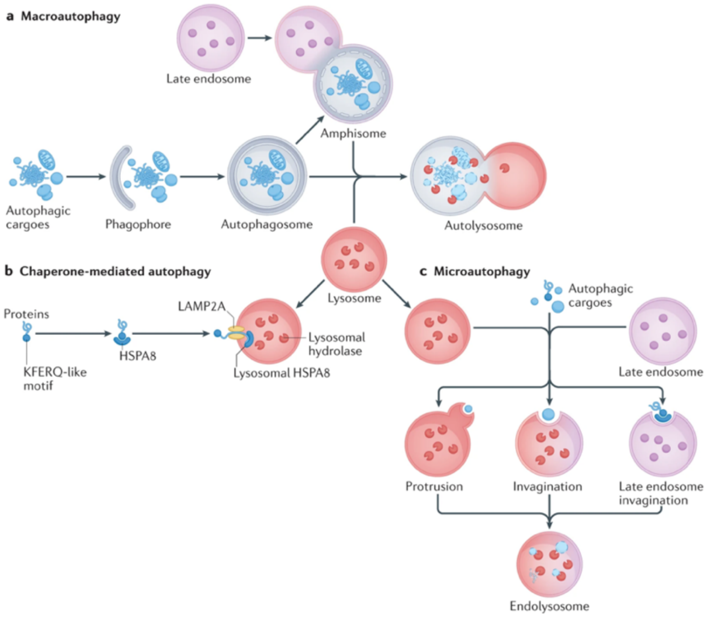

Figure 2| A schematic illustration highlighting the key features of macroautophagy and microautophagy

Although distinct in their biogenesis, both pathways share the defining features of cargo collection and transport into specialized membrane-bound organelles, which ultimately fuse with lysosomes to facilitate cargo degradation. In macroautophagy (A), cargoes are enclosed by a phagophore, which expands into a double-membrane autophagosome through membrane recruitment. The autophagosome fuses with lysosomes either directly or via intermediate formation of hybrid organelles so called amphisomes to form autolysosomes, where cargoes are degraded. In chaperone-mediated autophagy (B), cytosolic proteins with KFERQ-like motifs are recognized by Hsc70/HSPA8 and delivered to lysosomes via LAMP2A and lysosomal Hsc70/HSPA8 for degradation. In microautophagy (C), lysosomes and late endosomes directly engulf cargoes through membrane invagination, degrading them in the endolysosomal lumen. The figure is adapted from Wang et al., 2022.

Microautophagy has been implicated in the turnover of a specific subset of presynaptic proteins in *Drosophila melanigaster* (Uytterhoeven et al., 2015). This process is orchestrated by Hsc70-4, a chaperone that, in addition to its conventional chaperone activity, facilitates endosomal membrane deformation and microautophagy within synapses. The activity of Hsc70-4 selectively governs the turnover of Unc-13/Munc13 and EndoA synaptic proteins, which contain microautophagy recognition motifs. However, not all proteins with these motifs are targeted by Hsc70-4, underscoring the remarkable specificity of distinct degradation pathways in regulating the turnover of individual proteins. Notably, Hsc70-4-mediated membrane deformation enhances the readily releasable pool of synaptic vesicles and promotes neurotransmitter release, suggesting that endosomal microautophagy supports synaptic transmission by efficiently removing damaged or aged proteins (Uytterhoeven et al., 2015). Given the abundance of microautophagy recognition motifs among synaptic proteins, as well as the presence of Hsc70 and associated co-chaperones in vertebrate synapses, this pathway may represent a highly efficient mechanism for the selective and precise removal of individual proteins from the synaptic compartment (Andres-Alonso et al., 2021).

Recent study has established a direct link between CMA in neuronal dendrites and activity-dependent lysosomal secretion for neuronal protein disposal (Grochowska et al., 2022; Grochowska et al., 2023), emphasizing that two pathways may converge. Specifically, the lysosome-associated membrane protein 2A (LAMP2A) acts as the CMA receptor, facilitating the loading of CMA substrates. In contrast, the association of LAMP2B with the SH3-GK domain of SAP102/Dlg3 anchors exocytotic lysosomes to GluN2B-containing NMDARs. Upon NMDAR activation, this specialized subpopulation of lysosomes fuses with the plasma membrane, releasing CMA substrates into the extracellular milieu (Grochowska et al., 2023).

In contrast to conventional **macroautophagy**, **secretory autophagy** is a non-lytic type of autophagy pathway in which autophagosomes fuse with the plasma membrane rather than with lysosomes and secrete their cargo into the extracellular milieu (Ponpuak, M. et al. 2015), occurring both under normal conditions and during disease (Cadwell & Debnath, 2018).

Recent studies suggest that **secretory autophagy** in non-neuronal cells depends on the LC3-conjugation machinery to regulate the selective loading of specific proteins into extracellular vesicles (EVs) (Leidal et al., 2020) and serves as an alternative pathway for maintaining intracellular proteostasis in response to compromised lysosomal function and impaired degradation (Solvik et al., 2022).

Neurons utilize **secretory autophagy** to facilitate the release of toxic proteins (Nakamura et al., 2024). Additionally, it may function as a rapid response mechanism, enabling the secretion of signaling molecules and extracellular vesicles to regulate synaptic plasticity and promote neuronal survival (Chang et al., 2024). Furthermore, **secretory autophagy** has been implicated in the extracellular release of inflammation-related cargo, including IL-1β, HMGB1, and MMP9, as well as organelles such as mitochondria (Dupont et al., 2011; Kim et al., 2021; Martinelli et al., 2021; Tan et al., 2022).

LC3-dependent extracellular vesicle loading and secretion (LDELS) is a secretory autophagy pathway in which the macroautophagy machinery facilitates the packaging of cytosolic cargos, such as RNA-binding proteins, into EVs for secretion outside the cell (Gardner et al., 2022). The transferrin receptor (TFRC) has been identified as a transmembrane cargo secreted via EVs within the LDELS pathway. Specifically, TFRC secretion via EVs requires components of the MAP1LC3/LC3-conjugation machinery but occurs independently of other ATGs involved in classical autophagosome formation. Additionally, the packaging and secretion of this transmembrane protein into EVs depend on multiple components of the ESCRT pathway and the small GTPase RAB27A. This pathway utilizes a pool of LC3 localized at single-membrane endosomes, rather than double-membrane autophagosomes. Thus, LDELS shares similarities with other autophagy-related pathways that involve the conjugation of ATG8 to single membranes (CASM) (Durgan et al., 2021; Gardner et al., 2022).

The functional interplay **between degradative** and **secretory autophagy** in neurons and non-neuronal cells, as well as the mechanisms of fusion between autophagosomes and either lysosomes or the plasma membrane, will be addressed below.

1.1.2. Canonical autophagy pathway and endolysosomal membrane dynamics

Autophagy is initiated by the assembly of a pre-autophagosomal structure, referred to as the initiation site, primarily near the endoplasmic reticulum (Hollenstein & Kraft, 2020) (*Fig. 3*), where the Unc51-like complex, composed of ULK1, ATG13, FIP200, and ATG101, becomes activated. Under nutrient-rich conditions, mTORC1 phosphorylates and inhibits the ULK1 complex to prevent autophagy activation.

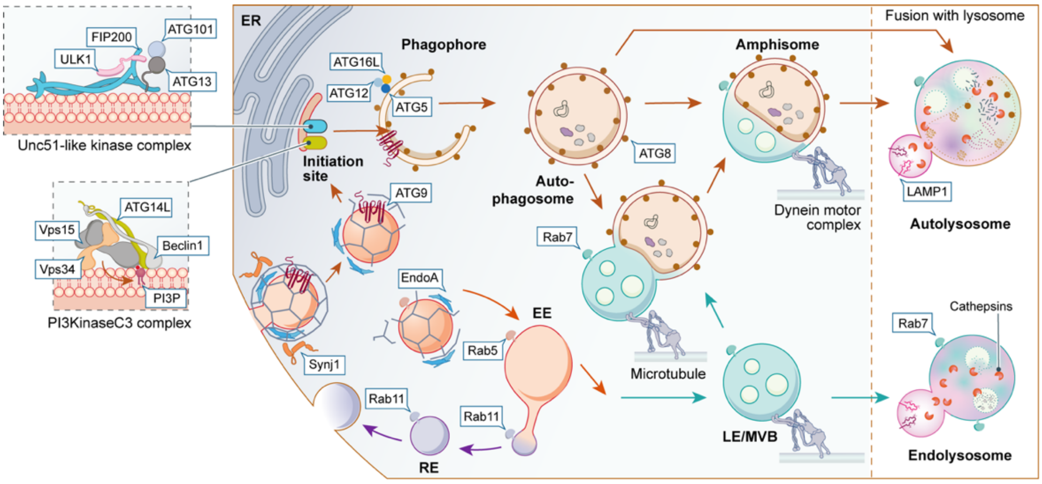

Figure 3| ***Mechanism of autophagosomal biogensis and endolysosomal membrane dynamics*** *(adapted from Grochowska et al., 2022 and Karpova et al., 2025). Explanation is in the text.*

Conversely, during nutrient starvation or cellular stress, mTORC1 activity is inhibited, leading to the activation of the ULK1 complex. This activation recruits additional proteins to assist in initiating autophagosome formation. Notably, at this nexus, the phosphorylation-mediated activation of ULK1 facilitates the assembly of other autophagy-related complexes and activates downstream signaling pathways essential for phagophore formation (Kim et al., 2011). The second critical component of the initiation site is the PI3KC3 complex I, composed of Vps34, Vps15, Beclin-1, and ATG14L, which synthesizes the signaling lipid phosphatidylinositol 3-phosphate [PI(3)P]. PI(3)P serves as a crucial signaling lipid that mediates the recruitment of a series of autophagy-related proteins, such as WIPI and ATG proteins, necessary for the formation of the phagophore, the primary isolation membrane of the autophagosome (*Fig. 3*). The regulation of this lipid signaling pathway is tightly controlled to <u>ensure phagophore formation occurs only when needed and in the appropriate spatial context</u> (Mizushima et al., 2011). A further critical player in the initial stages of phagophore nucleation and expansion is the lipid scramblase ATG9, which is delivered via ATG9 containing vesicles. Endophilin A (EndoA) and Synaptojanin 1 (Synj1) are involved in the recycling of ATG9 vesicles (*Fig. 3*).

A complex consisting of ATG5, ATG12, and ATG16L1 facilitates autophagosome formation by conjugating ATG8 family members (e.g., LC3 and GABARAP proteins) to phosphatidylethanolamine within the phagophore membrane (Kabeya et al., 2000;

Galluzzi et al. 2017). Sealed autophagosomes can undergo fusion with lysosomes to form autolysosomes (Feng et al., 2013) or with Rab7-positive late endosomes/multivesicular bodies (LE/MVB) to generate signaling organelles known as amphisomes (Filimonenko et al., 2007). Autophagosome formation is closely linked to endocytic pathways, including the sorting of proteins and lipids from early endosomes (EE) to recycling endosomes (RE) or late endosomes (LE) for degradation, a process mediated by small Rab GTPases.

In neurons, LE/multi-vesicular bodies (MVBs) are transported retrogradely to the soma via dynein motors, where they fuse with degradative lysosomes to form endolysosomes. Amphisomes arise from the fusion of LE/MVB with autophagosomes, a critical step that enables autophagosomes to acquire motors necessary for retrograde transport (Filimonenko et al., 2007; Maday, Holzbaur, 2016). Upon reaching the soma, these organelles ultimately fuse with acidic lysosomes, forming autolysosomes to facilitate cargo degradation. The lysosomal degradation ultimately leads to the retrieval of crucial cellular components, such as amino acids, lipids, and sugars, which are recycled back into the cytoplasm to support other cellular activities. This last step is the most important part in the proper functioning of cellular homeostasis and in the assurance that a cell could procure resources when subjected to stress conditions (Nakamura & Yoshimori, 2017).

1.1.3. Constitutive versus induced autophagy in neurons

There are both **constitutive** and **induced** pathways for autophagy in neurons (Stavoe & Holzbaur, 2019). Constitutive autophagosome formation has been observed in developing axons of mammalian neurons in primary culture (Maday & Holzbaur, 2016) and *C. elegans in vivo* (Stavoe et al., 2016), highlighting its role in maintaining neuronal and synaptic homeostasis (Karpova et al., 2025). In contrast, the potential for autophagy induction in the presynaptic compartment by starvation, commonly a trigger in non-neuronal cells, remains debated (Stavoe & Holzbaur, 2019). Beyond constitutive processes, various autophagy-inducing pathways influence synaptic structure and function. For example, rapamycin, an mTORC1 inhibitor, induces autophagic vacuole formation in dopaminergic axons and impairs neurotransmitter release (Hernandez et al., 2012). In hippocampal neurons, nutrient deprivation activates mTOR-dependent autophagy, leading to presynaptic structural and functional changes (Catanese et al., 2018). Locally, Reactive Oxygen Species (ROS) can also trigger autophagy in presynaptic boutons (Hoffmann et al., 2019). Furthermore, KCl-induced depolarization increases LC3-positive structures in axonal terminals and other neuronal compartments in rodent hippocampal cultures (Wang et al., 2015), and activity-induced autophagosome formation has been observed at presynapses of AIY neurons in *C. elegans* (Hill et al., 2019). Although somewhat discrepant with the previous studies, chemical induction of long-term depression (chem-LTD) through low-dose NMDA application (Shehata et al., 2012) or chronic silencing via TTX (Wang et al., 2023) also globally induces autophagy in primary rodent neurons, likely via mTORC1 inhibition.

1.1.4. Bulk versus selective autophagy, selective autophagy receptors

Autophagy can be classified as **non-selective**, characterized by the indiscriminate engulfment of cytosolic components, typically in response to nutrient deprivation, such as ATP depletion, glucose limitation, or amino acid insufficiency (Mizushima et al., 2004). This process, commonly referred to as **bulk autophagy**, serves as a survival mechanism under metabolic stress (Vargas et al., 2022). In contrast, **selective autophagy** targets specific cellular components for degradation, including damaged organelles (e.g., mitophagy, lysophagy, ER-phagy, ribophagy), aggregated proteins and RNA aggregates (aggrephagy), lipid droplets (lipophagy) and invading pathogens (xenophagy). Several autophagy receptors have been identified that confer cargo specificity by recognizing and facilitating the selective engulfment of these substrates. Accordingly, the term **"selective autophagy"** describes a degradative pathway that precisely identifies and removes designated cargo through the autophagy machinery, employing **selective autophagy receptor** (SARs) proteins (Conway et al., 2020; Vargas et al., 2022). **Selective autophagy** requires precise recognition of specific cargo, a process that is often mediated through cargo ubiquitylation (Gubas et al., 2022), a mechanism absent in bulk autophagy (Vargas et al., 2022).

Autophagy receptor proteins associate with the lipidated form of the microtubule-associated protein 1 light chain 3b (LC3B -II), which is anchored to both the inner and outer membranes of the phagophore and remains associated after the closure of the autophagosome. These receptors are characterized by the presence of LC3-interacting region (LIR) domains, defined by the core motif [W/F/Y]0-X1-X2-

[L/V/I]3, where positions X0 and X3 are absolutely conserved. Additionally, they contain ubiquitin-binding domains that facilitate the bridging of cargo and lipidated LC3, thereby promoting the engulfment of autophagic cargo (Kirkin et al., 2019).

In recent years, substantial progress has been made in identifying ubiquitin-dependent selective autophagy receptors in both non-neuronal and neuronal cells, including sequestosome 1/p62 (SQSTM1), TAX1BP1, NDP52 (CALCOCO2), NBR1, and optineurin (OPTN), among others (Bjorkoy et al, 2005; Kirkin et al, 2009; Wild et al, 2011; Newman et al, 2012; Thurston et al, 2012; Lazarou et al, 2015; Johansen & Lamark, 2020; reviewed in Gatica et al., 2018; Rubinsztein et al., 2012; reviewed in Kumar et al., 2022).

Neurons, known for their high energy demands, depend significantly on adenosine triphosphate (ATP) produced by mitochondria (Lu et al., 2018). **Selective mitophagy** plays a crucial role in removing and recycling damaged mitochondria, while also regulating the biogenesis of new, fully functional mitochondria, thereby preserving healthy mitochondrial functions and activities (Reviewed in Picca et al., 2023). This process plays a crucial role in maintaining neuronal homeostasis and quality control (Evans & Holzbaur, 2020).

Mitophagy can be classified into two main categories: PINK1–Parkin-dependent and PINK1–Parkin-independent pathways. Adaptor proteins (SARs), including optineurin, NDP52, and p62, bind to polyubiquitinated (p-Ub) chains and are recognized by LC3. PINK1–Parkin-independent mitophagy pathways involve additional players, such as BCL2-interacting protein 3 (BNIP3), NIP3-like protein X (NIX), and FUN14 domain-containing protein 1 (FUNDC1), which can recruit LC3 independently of PINK1 and Parkin to promote mitophagosome formation (Terešak et al., 2022). A variety of other mitophagy receptors participate in the execution of mitophagy, including BCL2L13, FKBP8, PHB2, and cardiolipins, as well as the mitophagy–autophagy receptors AMBRA1, TAX1BP1, and NBR1 (Palikaras et al., 2018; Lou et al., 2020), in addition to GPR50 (Liu et al., 2024).

Neuronal **ER-phagy** has been recently implicated in controlling axonal ER calcium stores to regulate neurotransmission in healthy neurons and in the brain (Kuijpers et al., 2021). Furthermore, multiple ER-phagy receptors have been identified, including FAM134B/RETREG1 (Khaminets et al., 2015), SEC62 (Fumagalli et al., 2016), RTN1 (Mou et al., 2024), RTN3L (Grumati et al., 2017), CCPG1 (Smith et al., 2018), ATL3 (Chen et al., 2019), TEX264 (Chino et al., 2019), and FAM134A/RETREG2 and FAM134C/RETREG3(Reggio et al., 2021; Berkane et al., 2023; Hoyer et al., 2024), each contributing to the regulation of endoplasmic reticulum turnover through selective autophagy. Most ER-phagy receptors are connected to the ER via a transmembrane domain responsible for cargo binding, and they also possess an LIR -motif that enables interaction with members of the LC3/GABARAP protein family on the autophagic membrane.

Thus, the progressive expansion of the list of SARs highlights the growing complexity involved in the regulation of **selective autophagy**.

1.1.5 Cargo availability for phagophore engulfment

As discussed earlier, the regulation of lipid signaling pathways is tightly regulated to ensure that phagophore formation occurs only when necessary. In this context, a compelling hypothesis has recently been proposed by leading autophagy researchers, suggesting a mechanism that governs the contextual specificity of phagophore formation and cargo engulfment in neurons (*Fig. 4*). This hypothesis posits that at least **three distinct factors** contribute to cargo availability for phagophore engulfment, independently of the mechanisms driving autophagy induction (Karpova et al., 2025).

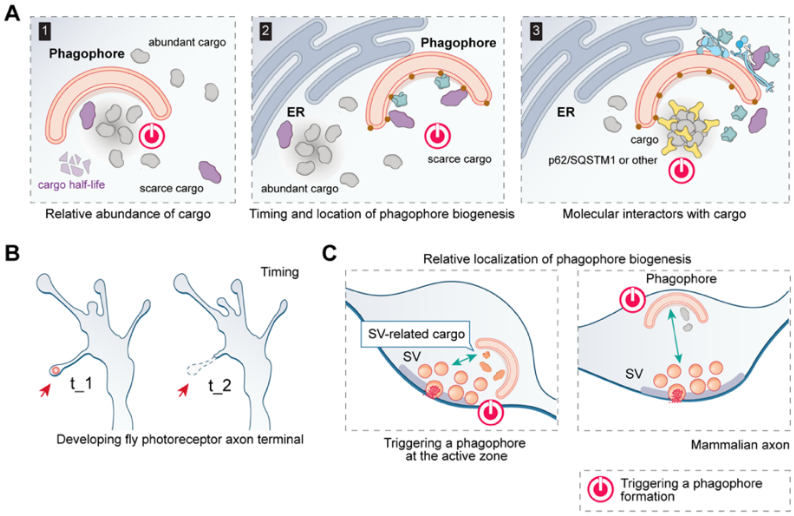

Figure 4| Contextual specificity of phagophore formation and cargo engulfment

(a) Factors that may simultaneously contribute to the selection of engulfed cargo and its accessibility could also promote phagophore formation in proximity to the cargo. Receptors such as p62/SQSTM1 play a dual role by directing phagophore recruitment and directly or indirectly facilitating autophagosome formation. (b) Autophagosome formation at the filopodial tips of developing axonal terminals in photoreceptors often leads to filopodia collapse, suggesting a

mechanism involving bulk engulfment of available cargo. (c) Phagophore formation initiated near synaptic release sites is more likely to engulf synaptic vesicle-related cargo compared to phagophores formed at more distal locations. (Adapted from Karpova et al., 2025)

First, the relative abundance of cargo, which is closely related to protein half-life; second, the timing and spatial location of autophagosome biogenesis relative to the localization of the cargo; and third, the direct or indirect molecular interaction of cargo with early-acting components of the autophagic machinery (e.g., autophagy adaptors or receptors) during phagophore formation (*Fig. 4A*). Additionally, the temporal and spatial regulation of autophagosome formation significantly constrains the pool of available cargo proteins (*Fig. 4B*). Consequently, it can be assumed that sub-compartment-specific proteomes quantitatively influence cargo composition, particularly when autophagosome induction is spatially and temporally controlled (*Fig. 4C*). For instance, activity-dependent autophagosome formation near presynaptic release sites would increase the likelihood of synaptic vesicle-related proteins being incorporated into the autophagosomal degradome (*Fig. 4C*).

1.1.6. The spatial organization of autophagy and autophagosomal transport in neurons

The main machinery for neuronal protein synthesis and degradation is localized within the neuronal soma, while synaptic junctions are often situated at considerable distances from the cell body. Consequently, precise regulation of **transport mechanisms** is essential to ensure the efficient delivery of newly synthesized proteins, the removal of misfolded proteins and damaged organelles, and the execution of somatic disposal processes, all of which are necessary to maintain proper neuronal function. The catabolic function of autophagosomes largely depends on their fusion with lysosomes, which are mainly present within the cell soma.

To reach lysosomes, autophagosomes utilize molecular motors for transport (Lee et al., 2011; Maday and Holzbaur, 2014; Maday et al., 2012; Maday and Holzbaur, 2016; Kulkarni and Maday, 2018). Both dynein (Jahreiss et al., 2008; Batlevi et al., 2010; Kimura et al., 2008; Cai & Ganesan, 2022) and kinesins (Maday et al., 2012) participate in the transport of autophagic vesicles along microtubules (reviewed in Kast & Dominguez, 2017), and both co-fractionate with axonal autophagosomes (Maday et al., 2012). Movement along microtubules occurs in a bidirectional, stop-and-go manner and is regulated by the alternating activities of a plus-end-directed kinesin motor and a minus-end-directed dynein-dynactin motor.

Additionally, autophagic vesicles navigate through the axons using **motor-adaptor-mediated strategies** (Cheng et al. 2015, Jordens et al. 2001, Wijdeven et al. 2016) and association with scaffolding proteins (Fu et al. 2014, Wong & Holzbaur 2014b), to enable fast and slow motility of autophagic vesicles, stationary pauses, prolonged stops with varying dwell times, and fusion with other organelles (Cason et al., 2021; Cason & Holzbaur, 2023).

Dynein is the primary motor responsible for driving the retrograde transport of autophagic vesicles from distal axons to the soma (Cai et al., 2010; Katsumata et al., 2010; Lee et al., 2011; Maday et al., 2012). The involvement of various dynein adaptors adds further complexity to the logistics of AV trafficking (Cheng et al., 2015; Andres-Alonso et al., 2019; Cai and Ganesan, 2022; reviewed in Nambiar & Manjithaya, 2024). Specifically, dynein adaptor **RILP** (Rab7-interacting lysosomal protein), implicated in endo-lysosomal mobilization during the host cell response to adenoviral and bacterial infections (Tan et al., 2011; Scherer et al., 2014; Harrison et al., 2004; Starr et al., 2008; Wozniak et al., 2016), is essential for the retrograde transport of neuronal autophagosomes. It associates with autophagosomes via LC3 and interacts with ATG5 on isolation membranes, preventing premature dynein recruitment and autophagosome transport (Khobrekar et al., 2020). Therefore, the sequential interactions of RILP with ATG5, LC3, and dynein serve to coordinate isolation membrane extension with the initiation of retrograde autophagosome motility. This mechanism ensures that, regardless of where autophagic events occur within the cell, the completed autophagosome promptly begins its transport to the cell body for degradation (Khobrekar et al., 2020).

The motility of newly formed autophagosomes at the distal axon tip may be driven by kinesin and myosin through their respective motor adaptors, **FYCO1** (FYVE and coiled-coil [CC] domain-containing protein 1) and **optineurin** (Pankiv et al., 2010; Tumbarello et al., 2012). FYCO1, which regulates kinesin activity, has been found to associate with LC3-, Rab7-, and PI3P-interacting proteins and is involved in the regulation of microtubule plus-end–directed transport of autophagic vesicles (Pankiv et al., 2010).

In distal axons, autophagosomes initially exhibit bidirectional movement or frequent back-and-forth motion, followed by processive retrograde transport (Fu & Holzbaur, 2014) and the scaffolding protein **MAPK8IP1/JIP1** is implicated in the regulation of autophagosome motility. MAPK8IP1/JIP1 is recruited to autophagosomes through direct binding to LC3, and its recruitment to **nascent** autophagosomes coincides with the initiation of unidirectional retrograde transport. Notably, depletion of MAPK8IP1/JIP1 leads to the accumulation of autophagosomes within this region (Fu et al., 2014). As a scaffolding protein, MAPK8IP1/JIP1 directly interacts with both kinesin-1 heavy chain (KIF5/KHC) and the DCTN1/p150Glued subunit of dynactin, an activator of dynein. However, MAPK8IP1/JIP1 cannot simultaneously bind to both motor complexes, resulting in the formation of two distinct MAPK8IP1/JIP1 complexes, one facilitating anterograde transport and the other promoting retrograde transport. The transition between these two complexes is regulated by phosphorylation of MAPK8IP1/JIP1 at S421, a MAPK8/JNK phosphorylation site located within the KIF5-binding domain. Maintaining MAPK8IP1/JIP1 in its non-phosphorylated state (as seen in the MAPK8IP1-S421A mutant) sustains retrograde autophagosome transport (Fu & Holzbaur, 2013). DUSP1/MKP1 (dual specificity phosphatase 1) robustly associates with MAPK8IP1/JIP1-positive autophagosomes along the axon, likely acting to maintain MAPK8IP1/JIP1 in its dephosphorylated state as autophagosomes are transported toward the cell body. Thus, phosphorylation of MAPK8IP1/JIP1 at S421 functions as a molecular switch, regulating the **directional movement** of autophagosomes along the axon (Fu et al., 2014). Surprisingly, both anterograde-directed KIF5/kinesin-1 motors and retrograde-directed dynein motors are tightly associated with axonal autophagosomes, even as these organelles move processively in the retrograde direction over long distances (Fu & Holzbaur, 2014). One proposed explanation is that autoinhibited KIF5 remains bound to the retrograde MAPK8IP1/JIP1 complex via its associated adaptor, K*LC-NE* (kinesin light chain), and that the local activation of KIF5 may be important for "circumnavigating road blocks along the axon" (Fu et al., 2014; Fu & Holzbaur, 2013). However, the potential involvement of neuronal activity in regulating this switching mechanism remains to be elucidated. In addition to MAPK8IP1/JIP1 mediating nascent autophagosome transport at the distal axons, a later study identified multiple dynein effectors on autophagosomes as they transit along the axons of primary neurons. In the mid-axon, autophagosomes require HAP1, a dynein activator that binds the dynein–dynactin complex through both canonical and noncanonical interactions, as well as Huntingtin (Htt, *Fig. 5*). Thus, both, HAP1 and Htt drive autophagosome transport in the mid-axons (Wong and Holzbaur, 2014; Cason et al., 2021).

c-Jun N-terminal kinase–interacting protein 3 (JIP3; also known as Sunday Driver/SYD or UNC-16) interacts with kinesin-1, dynein, and dynactin and was recently shown to facilitate autophagosome transport in *Caenorhabditis elegans*axons (Cavalli et al., 2005; Arimoto et al., 2011; Cockburn et al., 2018; Hill et al., 2019). In contrast to JIP1, JIP3 specifically regulates the transport of mature autolysosomes. Inhibiting autophagosomal transport disrupts maturation, while inhibiting autophagosomal maturation perturbs the association and function of dynein effectors. Thus, maturation and transport are tightly linked. These findings reveal a novel maturation-dependent dynein effector handoff on neuronal autophagosomes, which is essential for motility, cargo degradation, and the maintenance of axonal health (Cason et al., 2021; *Fig. 5*).

Axonal transport of autophagosomes is regulated by the dynein activators JIP3 and JIP4, as well as the small GTPases ARF6 and RAB10 (Cason & Holzbaur, 2023). JNK-interacting proteins 3 (JIP3) and 4 (JIP4) serve as activating adaptors for dynein and are regulated on autophagosomes and lysosomes by these small GTPases. Both ARF6 and RAB10 are essential for coordinating the opposing activities of bound dynein and kinesin motors. GTP-bound ARF6 promotes the formation of the JIP3/4–dynein–dynactin complex, while RAB10 is required to balance the functions of dynein and kinesin motors.

Another **motor-adaptor-mediated** strategy for navigating autophagic vesicles and amphisomes, hybrid organelles in the autophagy pathway, within axons involves **Snapin** (SNAP25-interacting protein). Snapin functions as an adaptor that recruits dynein motors to late endosomes and amphisomes by binding to the dynein intermediate chain (DIC) (Cai et al., 2010, *Fig. 5, Fig. 6*). Upon phosphorylation by PKA, Snapin dissociates from the motor, promoting organelle immobilization at synaptic botons (Chheda et al., 2001; Di Giovanni & Sheng, 2015; Andres-Alonso et al., 2019).

Axonal autophagosomes can fuse with late endosomes to form hybrid organelles known as **amphisomes**, which are then transported to the neuronal soma via a shared adaptor-motor mechanism acquired upon fusion (Cheng et al., 2015; Kononenko et al., 2017; Andres-Alonso et al., 2019; reviewed in Andres-Alonso et al., 2021; reviewed in Grochowska et al., 2022, reviewed in Karpova et al., 2025).

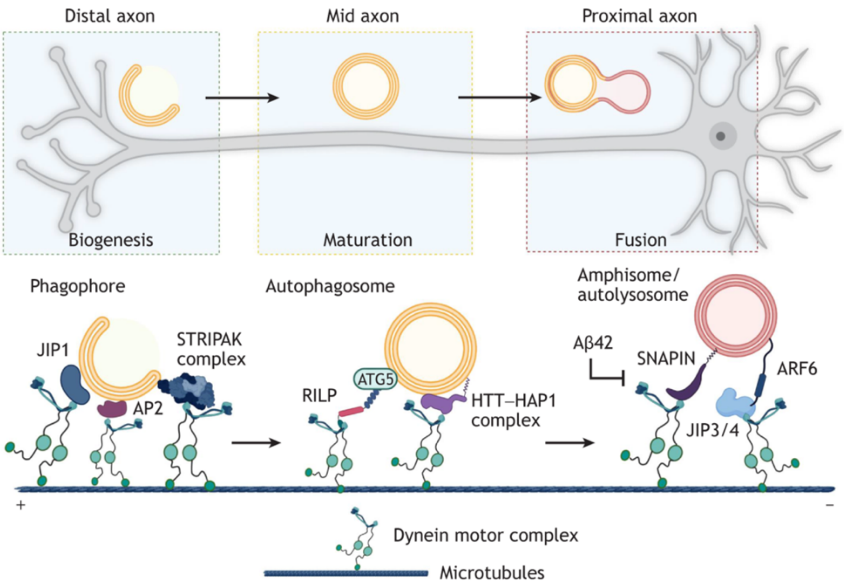

Figure 5| ***Dynein and its co-factors in neuronal autophagy***

As autophagosomes exit the distal axonal tip and navigate toward the soma for fusion with lysosomes, a sequential binding of JIP1, HAP1, and a complex containing JIP3 and/or JIP4 (hereafter referred to as JIP3/4) occurs. This process may be regulated by the incorporation or dissociation of additional factors on the autophagosomal membrane, which is influenced by the maturation status of the autophagosomes within the axon (Cason et al., 2021). Various other adaptors, including Rab-interacting lysosomal protein (RILP; Wijdeven et al., 2016; Khobrekar and Vallee, 2020; Khobrekar et al., 2020), oxysterol-binding protein homologue (ORP1L, also known as OSBPL1A; Wijdeven et al., 2016), the adaptor protein 2 (AP2) complex (Kononenko et al., 2017), SNAP-associated protein (SNAPIN), and the HTT–HAP1 complex, interact with various components of the dynein complex and autophagosomes, thereby facilitating retrograde transport in different cell types. (Adapted from Nambiar & Manjithaya, 2024).

Intriguingly, amphisome possess both degradative and signaling capacities (Andres-Alonso et al., 2019; reviewed in Andres-Alonso et al., 2021; Kuijpers et al., 2021), therefore are capable to stimulate synaptic vesicle release at synaptic boutons (Andres-Alonso et al., 2019). Stationary pauses of amphisomes at synaptic boutons have attracted particular interest and were recently shown to depend on two molecular mechanisms operating downstream of cAMP and PKA activation (*Fig. 6.* Andres-Alonso et al., 2019): (a) modulating the interaction of amphisomes with the dynein motor complex, a process facilitated by the motor adaptor protein Snapin (Cai et al., 2010; Xie et al., 2015; Andres-Alonso et al., 2019); and (b) regulating motor processivity by modulating the GTPase-activating protein (GAP) activity of RapGAP SIPA1L family members, which have been identified in association with the outer membrane leaflet of autophagosomes (Andres-Alonso et al., 2019; Goldsmith et al., 2022).

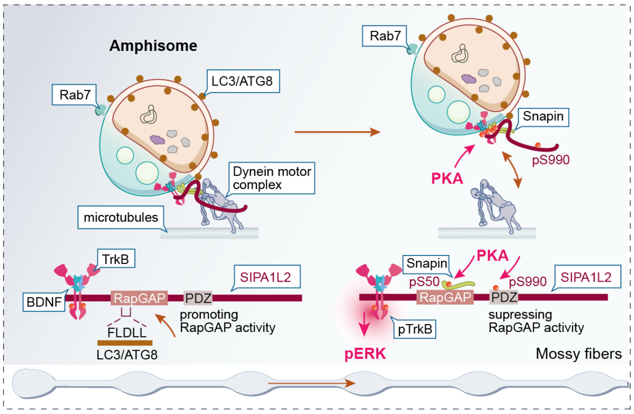

Figure 6| Molecular mechanism of amphisome immobilization/pausing at synaptic boutons.

(A) LC3B /Rab7-positive hybrid organelle, amphisome, retrogradely traffics along the axon and association of LC3B promotes RapGAP activity of SIPA1L2 ensuring its fast velocity. The PKA-dependent phosphorylation of the dynein adaptor Snapin, which results in the dissociation of SIPA1L2/Snapin complex from the Dynein intermediate chain (DIC), leads to the immobilization of amphisomes at synaptic boutons. (B) SIPA1L2 is a substrate for PKA, and the SIPA1L2 S990D mutant exhibited a downregulation of its RapGAP activity favoring ERK signaling involved in motor processivity (adapted from Andres-Alonso et al., 2019; Karpova et al., 2025).

After PKA-dependent pausing at synaptic boutons, LC3B -positive amphisomes resume their retrograde movement. Pharmacological inhibition of the PKA activity significantly reduces their dwell time (Andres-Alonso et al., 2019), suggesting that the reassembly of LC3B -positive vesicles with the motor complex for retrograde transport is dependent on the **dephosphorylation** of the PKA substrate, the motor-adaptor protein Snapin (Chheda et al., 2001; Di Giovanni & Sheng, 2015; Andres-Alonso et al., 2019), to allow for recoupling with DIC. Phosphatases from various families are abundant at synapses, where they regulate synaptic transmission and plasticity, and their phosphatase activity is tightly controlled (Foley et al., 2023; Woolfrey & Dell'Acqua, 2015). However, the specific phosphatase responsible for Snapin dephosphorylation and the promotion of Snapin-DIC recoupling remains to be identified.

The tethering of kinases and phosphatases, as well as GTPase-activating protein (GAP)- and guanine nucleotide exchange factors (GEF) activities to scaffold complexes, provides a mechanism by which the motors, cargo attachments, and directed transport of organelles on the autophagy pathway can be locally regulated (Fu et al., 2014; Chheda et al., 2001; Di Giovanni & Sheng, 2015; Andres-Alonso et al., 2019; Cason & Holzbaur, 2023). This finding was further supported by the identification of the scaffolding protein connector of kinase to AP-1 (CKA) as essential for autophagosome transport in neurons (Neisch et al., 2017; *Fig. 5*). Alongside other core components of the striatin-interacting phosphatase and kinase (STRIPAK) complex, CKA associates with dynein and directly binds to Atg8a, an autophagosomal protein. CKA functions as a regulatory subunit of PP2A, which is a component of the STRIPAK complex that modulates dynein activity by facilitating the axonal transport of dense core vesicles and autophagosomes in a PP2A-dependent manner (Neisch et al., 2017).

Although autophagosome formation has primarily been shown to occur in distal axons of both vertebrate and invertebrate neurons (Maday & Holzbaur, 2014; Soukup et al., 2016; Stavoe et al., 2016; Okerlund et al., 2017), there is evidence suggesting that similar processes occur in other cellular compartments, albeit with potentially distinct regulatory mechanisms. For instance, p62/SQSTM1, a widely used marker of autophagy that serves as a receptor for aggrephagy, accumulates in neuronal somata but not in axons when autophagy is compromised (Kuijpers et al., 2021; Liang et al., 2010). In contrast, the loss of neuronal ATG5, which impairs autophagy, leads to the extensive accumulation of tubular ER in axons, while the ER in somata and dendrites remains unaffected (Kuijpers et al., 2021; reviewd in Karpova et al., 2025). Recent evidence suggests that autophagy can also be initiated in the somatodendritic compartment, where it plays a crucial role in the turnover of postsynaptic proteins, thereby actively supporting long-term depression (LTD) (Kallergi et al., 2022; Keary et al., 2023; Shen et al., 2020) and regulating excitatory neurotransmission (Overhoff et al., 2022). Importantly, the movement of autophagic organelles within dendrites can be influenced by synaptic activity (Overhoff et al., 2022).

1.1.7. Autophagy in the regulation of synaptic function

Autophagy plays a critical role in the regulation of synaptic function, plasticity (Kallergi et al., 2022; Shen et al., 2020; Pan et al., 2021), and memory (Glatigny et al., 2019) by mediating the degradation of **synaptic cargos**, including major postsynaptic scaffolding proteins like PSD-95 and SHANK3. Impaired autophagy is frequently associated with neurodegeneration in the context of both aging and disease (Nixon, 2013; Tomoda et al., 2019; Nixon & Rubinsztein, 2024). Recent studies have specifically explored the role of autophagy in long-term depression (LTD), a form of synaptic plasticity governed by pre- and postsynaptic modifications in glutamatergic signaling (Kallergi et al., 2022; Shen et al., 2020; Pan et al., 2021). Following the induction of LTD, autophagic vesicles may form at the postsynapse, with key autophagy-related factors such as the ULK1 complex and ATG5 facilitating this process (Kallergi et al., 2022). This mechanism promotes the degradation of PSD-95 at synapses, thereby increasing the surface mobility of AMPA receptors (AMPARs) and enhancing their removal and degradation (*Fig. 7A*). Conversely, genetically induced upregulation of neuronal autophagy, specifically through targeting BDNF, has been shown to impair CA3-CA1 postsynaptic long-term potentiation (LTP) (Nikoletopoulou et al., 2017). Within the framework of BDNF-mediated synaptic plasticity, postsynaptic scaffolding proteins such as SHANK3, PSD-95, and PICK1 have been identified as cargo for autophagic degradation, suggesting that neuronal autophagy plays a pivotal role in regulating (post)synaptic plasticity by mediating the turnover of postsynaptic proteins via the lysosomal pathway (Kallergi et al., 2022).

Autophagy-deficient neurons completely suppress presynaptic long-term potentiation (mf-LTP) at mossy fiber synapses in the hippocampal CA3 region and exhibit axonal ER accumulation within synaptic boutons (*Fig. 7B*). This suggests that neuronal ER-phagy plays a critical role in regulating presynaptic excitatory neurotransmission by modulating ryanodine receptor (RyR)-mediated calcium release from axonal ER stores (Kuijpers et al., 2021). Furthermore, recent studies have identified specific subsets of ER membrane and lumenal proteins as preferred substrates for distinct autophagy receptors, highlighting the receptor-specific autophagic capture of ER in axons (Hoyer et al., 2024).

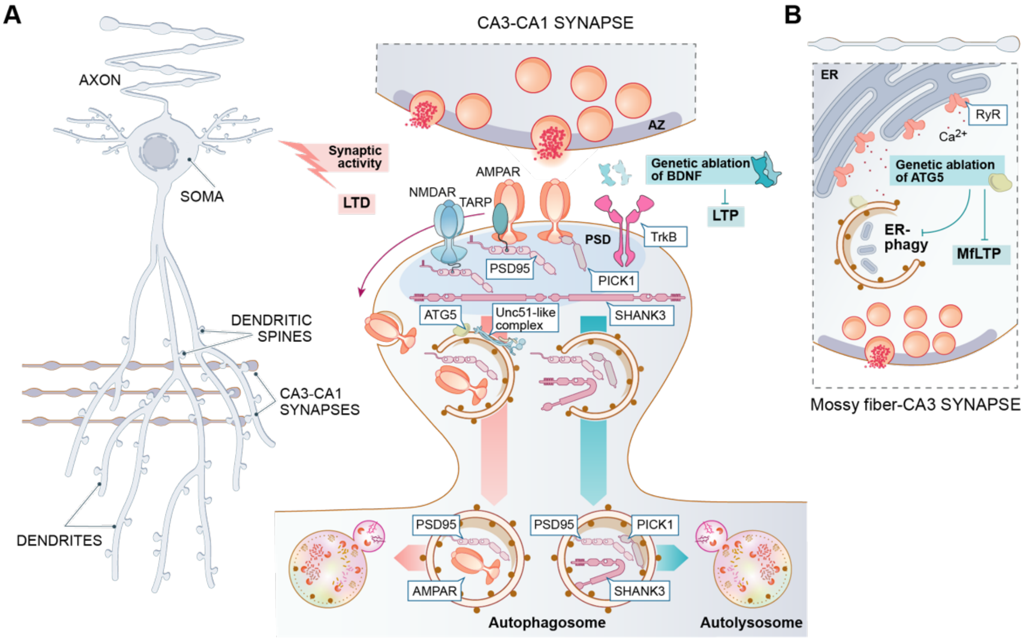

Figure 7| Regulation of autophagy in the context of synaptic functions

(Image adapted from Karpova et al., 2025. Explanations are provided in the text)

1.1.8. Secretory versus degradative autophagy

1.1.8.1. Differential regulation of SNARE proteins is defining autophagosome-plasma membrane and autophagosome–lysosome fusion

How **degradative autophagy** diverges from **secretory autophagy** is an intriguing question, particularly in the context of regulation of neuronal proteostasis. How neuronal activity and/or neuronal silencing controls the switch between these pathways remains largely unknown. Another unknown, how secretory autophagy is engaged, whether only under conditions of a compromised lysosomal system (e.g., damaged lysosomes or altered lysosomal function) or as an alternative mechanism for cargo disposal regulated in response to the specific extracellular stimuli and surface receptor activation.

In this chapter, I will summarize the current knowledge on the differential regulation of the fusion of autophagosomes with lysosomes and the plasma membrane, providing insights into the divergence between these two pathways.

The degradation of cytoplasmic components via autophagy requires the fusion of autophagosomes with lysosomes, a process mediated by the Soluble N-ethylmaleimide-sensitive factor Attachment Protein Receptor (SNARE) complex (Jian et al., 2024). It is well established that newly formed autophagosomes eventually acquire the Qa-SNARE **Syntaxin 17** (Stx17) (Itakura et al., 2012; Minton 2013; Tsuboyama et al., 2016; Li et al., 2020), which forms a stable binary complex with the Qbc-SNARE **SNAP-29** (Diao et al., 2015). Subsequently, the stabilization and tethering of this binary SNARE complex facilitate its pairing with the lysosomal R-SNARE **VAMP8**, driving the formation of a four-helix bundle SNARE complex that catalyzes fusion with lysosomes (Mizushima et al., 2011; Itakura et al., 2012; Hamasaki et al., 2013; Takats et al., 2014; Diao et al., 2015).

Intriguingly, recent evidence from non-neuronal autophagy research has revealed an alternative SNARE complex required for autophagosome-lysosome fusion, comprising Stx17-**SNAP47**-VAMP7/VAMP8 instead of the previously identified Stx17-**SNAP29**-VAMP7/VAMP8 complex (Jian et al., 2024). The involvement of these distinct SNARE complexes may differentiate starvation-induced **bulk autophagy** from **selective autophagy**, as the depletion of SNAP47 inhibits selective autophagy processes such as mitophagy, aggrephagy, and ER-phagy (Jian et al., 2024). Moreover, SNAP47 depletion also impairs starvation-induced autophagy to some extent, with this effect being further exacerbated by the simultaneous depletion of SNAP29 (Jian et al., 2024). These findings suggest that SNAP47 is indispensable for **selective autophagy** and operates in parallel with SNAP29 in **bulk autophagy** (Jian et al., 2024). In molecular turms, the regulation of bulk versus selective autophagy is distinguished by the post-translational modification of SNAP29 through O-linked-N-acetylglucosaminylation (O-GlcNAcylation), which inhibits the recruitment and function of SNAP29 in autophagosome-lysosome fusion (Jian et al., 2024).

In neurons, the fusion of amphisomes, a hybrid organnels on the autophagy pathway, with lysosomes is mediated by a similar SNARE complex (Stx17, SNAP29, and VAMP8), along with the HOPS tethering complex (Jiang et al., 2014), which facilitates cargo degradation and recycling (Cason et al., 2022). Additionally, recent studies have identified the involvement of YKT6, an R-SNARE protein, in the fusion process between autophagosomes and lysosomes (Matsui et al., 2018) and a critical SNARE involved in the lysosomal stress response (Cuddy et al., 2019).

On the other hand, the highly conserved SNARE family of eukaryotic proteins also mediates membrane fusion between organelles and the plasma membrane (Jahn et al., 2024) and similarly, **secretory autophagy** relies on a dedicated SNARE system

(Kimura et al., 2017), as well as specialized cytosolic **secretory autophagy cargo receptors**, such as TRIM16. Multiple lines of evidence suggest that Stx17, a SNARE protein essential for the formation of degradative autolysosomal compartments, is dispensable for **secretory autophagy** (Kimura et al., 2017a; Kimura et al., 2017b; Martinelli et al., 2021). Specifically, the primary differences between **degradative** and **secretory autophagy** may involve the differential utilization of SNARE proteins. While Stx17 is required for degradative autophagy, secretory autophagy relies on alternative SNAREs, such as **Sec22b/** SNAP-23 and SNAP-29/ syntaxin 3 or syntaxin 4 (Kimura et al., 2017; Martinelli et al., 2021). Concomitantly, multiple screening studies have identified **Sec22b** as being associated with extracellular vesicles (EVs) (Yamada et al., 2022), and several studies emphasize its role in the regulation of unconventional secretion (Yamada et al., 2022; Kowal et al., 2016).

Moreover, SNAP47 has also been identified as an R-SNARE **Sec22b** interactor (Huttlin et al., 2017), althought its role in secretory autophagy remains unknown. Whether this complex concomitantly influences the regulation of **selective** versus **bulk secretory autophagy** - analogous to **SNAP47** and **SNAP29's** role in **selective** versus **bulk degradative autophagy** (Jian et al., 2024) requires further investigation.

Despite the involvement of Sec22b in unconventional secretion (Yamada et al., 2022), its fusogenic role appears to be dependent on its association with specific syntaxins. For instance, the formation of a complex between Sec22b and Stx1, identified through a yeast two-hybrid screen in a human fetal brain cDNA library and confirmed by co-immunoprecipitation from mouse embryonic and adult brains, revealed a non-fusogenic Sec22b-Stx1 SNARE complex involved in plasma membrane expansion, which is critical for neurite growth (Perkovic et al., 2014). In addition to the Sec22b-Stx1 SNARE complex, Sec22b's involvement in the formation of SNARE complexes with SNAP23-syntaxin 18 (STX18), which mediates lipid droplet fusion (Fu et al., 2023), and SNAP23-STX3/STX4, which mediates secretory autophagy (Kimura et al., 2017a; Kimura et al., 2017b; Martinelli et al., 2021; Wu SY et al., 2024), suggests the presence of tightly regulated membrane fusion events governed by Sec22b's association with specific syntaxins.

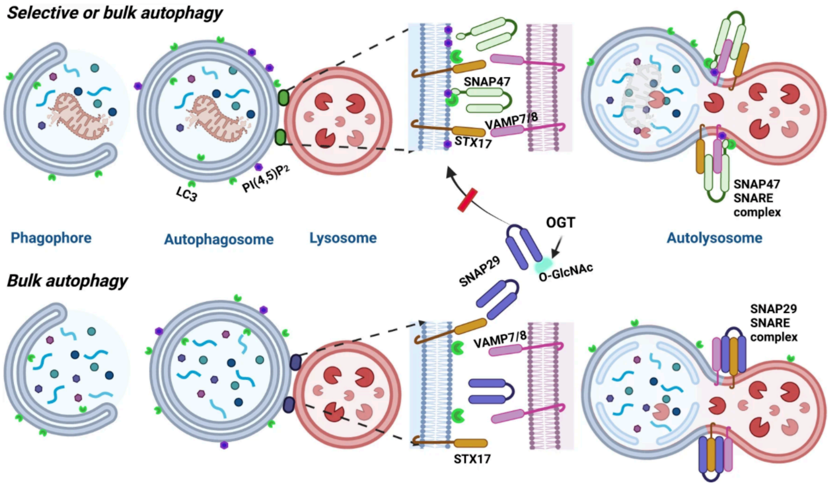

Figure 8| ***Diversity of SNARE complexes and posttranslational regulation of SNARE components in the control of autophagosomes-lysosomes fusion***

SNARE complex formed between STX17, VAMP7/8 and SNAP29 mediates autophagosome–lysosome fusion in bulk autophagy. Another SNAP29-containing complex (not shown) with YKT6 and STX7 has a similar function. The new SNARE complex between STX17, VAMP7/8 and SNAP47 mediates autophagosome–lysosome fusion in both bulk and selective autophagy. SNAP47 is recruited to autophagosomes through coincident detection of LC3 and PI(4,5)P2, whereas SNAP29 is excluded from participation in selective autophagy by OGT-mediated O-GlcNAcylation (adapted from Zhen & Stenmark, 2024).

Along with the utilization of distinct SNARE proteins that define the **switch** between **degradative** and **secretory autophagy**, specific post-translational modifications may fine-tune the balance between these processes. Additional insights into the mechanisms underlying this switch come from cancer research describing the impact of Stx17 post-translational modifications (Wei et al., 2024). Specifically, dephosphorylation of STX17 at Tyr157 and Tyr227 by protein tyrosine phosphatase 1B (PTP1B, encoded by *PTPN1*) favors this transition, as *PTPN1* knockout enhances the fusion between autophagosomes and lysosomes and PTP1B overexpression and tumor-derived extracellular vesicles can activate the secretory autophagy pathway (Wei et al., 2024).

1.1.8.2. The role of Sec22b in the nervous system

Although the origin of LC3B$^+$ Sec22b$^+$ carrier membranes and the role of the R-SNARE Sec22b in neuronal unconventional secretion (secretory autophagy) remain incompletely understood, accumulating evidence highlights its significance in neuronal function. Sec22b is highly enriched in axonal growth cones, where it contributes to neurite outgrowth (Perkovic et al., 2014). Additionally, large-scale nanoscopy and biochemical analyses of postsynaptic dendritic spines have identified Sec22b in both stubby and mushroom spines, suggesting a potential role in synaptic architecture and plasticity (Helm et al., 2021).

Intriguingly, the switch between **degradative** and **secretory autophagy** plays a crucial role in neural development and synaptic plasticity at the fly larval neuromuscular junction (NMJ) (Chang et al., 2024). Accordingly, neuronal activity enhances autophagy activation while concurrently suppressing degradative autophagy, thereby shifting the pathway toward autophagy-mediated secretion. Notably, presynaptic knockdown of SNAP29, Sec22, or Rab8, key regulators of the secretory autophagy pathway, completely disrupts activity-induced synaptic remodeling. This finding highlights **secretory autophagy** as a **transsynaptic signaling mechanism** that governs synaptic plasticity (Chang et al., 2024). In contrast, developmental synapse formation depends on protein turnover via the degradative autophagosome-lysosomal pathway (*Fig. 9*).

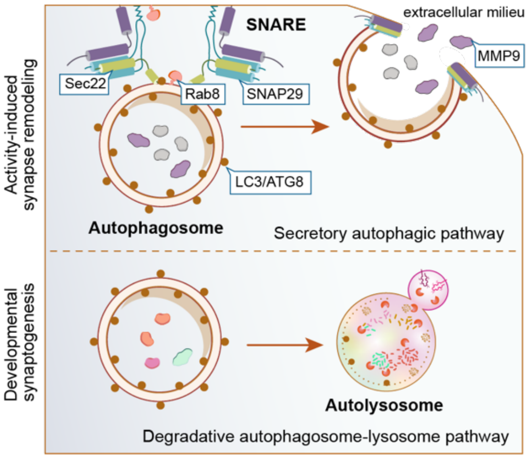

Figure 9| Secretory versus degradative autophagy

At the fly larval neuromuscular junction (NMJ), activity-induced synaptic remodeling depends on the secretory autophagy pathway involving the SNARE proteins SNAP29 and Sec22b and the small GTPase Rab8. In contrast, developmental synapse formation depends on protein turnover via the degradative autophagosome-lysosomal pathway (adapted from Karpova, et al., 2025)

The upregulation of Sec22b exerts a neuroprotective effect in a rat model of traumatic brain injury by promoting protective autophagy (Li et al., 2021). Conversely, an imbalance in the regulation of Sec22b and Ykt6 disrupts autophagosome axonal retrograde flux in neuronal ischemia–reperfusion injury (Li et al., 2022). Intriguingly, Affymetrix microarray data have identified *SEC22B* as a potential biomarker for Alzheimer's disease (AD) (Zhao et al., 2016). Furthermore, *SEC22B* expression is downregulated in the hippocampus of both aging and AD-affected brains (Berchtold et al., 2013; Zhao et al., 2016).

1.1.9. Regulation of axonal autophagic vesicle transport *in vivo*

Most of the current knowledge about autophagosomal trafficking is derived primarily from *in vitro* preparations, with limited insights from *in vivo* research. Consequently, our understanding of how network activity, behavior, and the sleep-wake cycle contribute to the regulation of autophagosomal transport, which is essential for maintaining neuronal proteostasis, remains incomplete.

Studying axonal autophagosome trafficking *in vivo* is challenging, particularly due to the complexities of axon-specific labeling strategies and the limited accessibility of axons for time-lapse imaging through a cranial window, given the constraints imposed by axonal topology as it traverses deep brain regions.

We recently highlighted technological advancements, particularly fiber-based in vivo imaging, for investigating membrane trafficking in relation to neuronal activity and animal behavior (Karpova, Aly et al., 2024). The ultra-thin laser-scanning endomicroscope enables subcellular resolution of membranous compartments, including vesicular structures as small as lysosomes (Stibůrek et al., 2023). This innovation offers new prospects for *in vivo* subcellular imaging, facilitating the exploration of multiple membranous compartments including autophagosomes, their functional properties, and trafficking dynamics in response to neuronal activity.

Recently, the transport of autophagic vesicles in acute optic nerve preparations was visualized using two-photon microscopy (Luo et al., 2024), with the objective tip immersed in physiological solution above the optic nerve. This suggests that the animal was imaged under deep anesthesia; however, the potential impact of anesthesia on autophagic vesicle trafficking under these conditions was not evaluated. The authors reported that the majority (85%) of autophagic vesicles were transported in the retrograde direction under these conditions. Assessment of trafficking velocities revealed higher values in the retrograde direction compared to the anterograde direction. Addtionally, optic nerve crush was found to disrupt the retrograde transport of autophagic vesicles, while anterograde transport remained unaffected for several hours (Luo et al., 2024).

These examples underscore the need for further *in vivo* investigations into the mechanisms of neuronal autophagy regulation and traficking within the context of complex brain function and behavior. One particularly compelling aspect of *in vivo* autophagy research is its potential to reveal detailed insights into specific cell types that are challenging to study in culture, especially those residing in hard-to-access brain regions. A notable example is noradrenergic neurons of the *locus coeruleus*, a brainstem structure that involved in the regulation of overall brain function and maintaining behavioral states like stress, sleep and wakefulness.

1.2. *Locus coeruleus*

The *locus coeruleus* comprises approximately 3,000 neurons in rodents (Sara, 2009) and fewer than 50,000 neurons in humans (Mouton et al., 1994). *LC-NE* neurons are characterized by relatively small cell bodies and extensively branched neuromodulator projections across diverse brain regions (reviewed in Chandler et al., 2019). These neurons are critically involved in modulating a wide range of functions, including wakefulness and sleep states, arousal, anxiety, attention, pain, mood, and the response to stress, thereby influencing animal behavior as well as various forms of learning and memory processes (Samuels et al., 2008; Sara, 2009; Wagatsuma et al., 2018; Suárez-Pereira et al., 2022; reviewed in Sara & Bouret, 2012; reviewed in Chandler et al., 2019; reviewed in Ross and Van Bockstaele, 2021).

1.2.1. Distinct modulatory functions of the *Locus coeruleus*

The *LC-NE* system is indispensable in physiological and stressful adaptive brain responses due to its widespread projection system and modular input-output organization, allowing for the task-specific activation of brain regions during the maintenance of homeostasis in dynamic situations (Ross, Bockstaele, 2021). The *LC-NE* system is also central in modulating attention, arousal, and states of vigilance (Zhang et al., 2023). *LC-NE* activity manipulations exert profound effects on these states; for example, the optogenetic activation of *LC-NE* neurons at a phasic activity pattern elicits the transition from sleep to wakefulness, whereas reduced activation, mimicking tonic *LC-NE* activity, disrupts delta and theta rhythms during sleep and increases sensory-evoked awakenings (Hayat et al., 2020). In contrast, inactivation of *LC-NE* activity results in reduced wakefulness duration, further identifying its role in vigilance maintenance (Aston-Jones & Bloom, 1981; Carter et al., 2010; Swift et al., 2018; Hayat et al., 2020).

The *LC-NE* neurons modulates arousal through reciprocal connections with the *PFC*. Concomitantly, these connections and the pattern of *LC-NE* activity determine arousal level during wakefulness (Hayat et al., 2020). Work in both mice and primates has described strong correlations between pupil area and arousal states (Breton-Provencher & Sur, 2019). The use of optogenetic activation and inactivation has demonstrated that increased or decreased arousal, respectively, may be induced by phasic *LC-NE* neurons. Prolonged phasic excitation of the *LC-NE* for more than one hour promotes arousal, but no similar effects have been found to result from tonic excitation (Reimer et al., 2016; Breton-Provencher & Sur, 2019; Joshi et al., 2016; Rajkowski et al., 1994). Sustained hyperactivation of *LC-NE* neurons promotes anxiety-like behavior and hyper-arousal, illustrating the inverted-U relationship between *NE* release and brain function (Valentino & Van Bockstaele, 2008; Yerkes & Dodson, 1908; Aston-Jones & Cohen, 2005; McGinley et al., 2015).

In attention regulation, the *LC-NE* system amplifies responses to goal-directed, high-salience information while suppressing low-salience stimuli (Zhang et al., 2023). This effect is largely due to *LC-NE* influence on *PFC* neuronal activity. The "glutamate amplifies noradrenergic effects" (GANE) model posits that increased glutamate at sites of arousal interacts with *NE* to form activity hotspots while suppressing lower-priority representations (Mather et al., 2016). *NE* also facilitates selective memory consolidation via synaptic plasticity, recruiting large-scale networks for long-term potentiation (LTP) and long-term depression (LTD). *LC-NE* activation during challenging tasks promotes sensory integration and behavioral outcomes (Aston-Jones & Cohen, 2005; Sara & Bouret, 2012; Robbins, 1984). Decreased *LC-NE* functionality with age is associated with a reduced ability in older adults to suppress non-salient information during arousal, contributing to cognitive difficulties (Lee et al., 2018).

Additionally, *LC-NE* system is critical to hippocampal function and the hippocampus receives very strong noradrenergic inputs from the *LC*. It has been implicated in spatial navigation, memory, and stress-related behaviors (Ross, Bockstaele, 2021). *LC-NE* activity controls hippocampal pyramidal cell firing through β-adrenergic receptors and affects the activity of inhibitory neurons via α-receptors, with α1 excitation and α2 inhibition (Pang & Rose, 1987; Bergles et al., 1996; Takeuchi et al., 2016). This system has been shown to impact memory process by facilitating synaptic plasticity in support of memory formation responsive to stress. *NE* acts together with dopamine (DA) to encode the salience of aversive experience (Hansen & Manahan-Vaughan, 2015; Nguyen & Connor, 2019; Lim et al., 2010; Lemon et al., 2009; Maity et al., 2015).

The neuromodulation of the amygdala by *LC-NE* projections, integrating sensory information from the cortex and thalamus, generates stress-related responses (Borodovitsyna et al., 2020). *NE* released by *LC-NE* controls neuronal activity in the *BLA* in stressful situations and conditions, which induces aversion, enhances anxiety-like behavior, and impairs extinction learning (Llorca-Torralba et al., 2019; Giustino et al., 2020). Concomitantly, chemogenetic inactivation of the *LC-BLA* pathway reduces pain-induced anxiety and fear learning (Llorca-Torralba et al., 2019). The *LC-NE* system takes part in the antiepileptic effects as well: *NE* is released within the cortex from *LC-NE* axons and, acting by volume transmission upon neuronal, glial, and vascular activities, it decreases seizure duration and propagation (Wahis, Holt, 2021). *LC-NE* lesion enhances seizures, eventually transforming the scattered events into status epilepticus (Giorgi et al., 2003; Giorgi et al., 2006; Giorgi et al., 2008). Co-released neuropeptides like galanin and neuropeptide Y converge to dampen seizure activity, further supporting the role of *LC-NE* (Mazarati et al., 1998; Mazarati et al., 2004).

Acute nociceptive inputs from the spinal cord to the *LC-NE* via the nucleus paragigantocellularis ensue in descending action of *LC-NE* axons on the spinal cord and medulla, exerting an analgesic effect (Kimura & Nakamura, 1985; Craig, 1992; Palkovits et al., 1995; Ennis et al., 1992). Lesions or inactivation of the *LC-NE* promoted acute pain responses; hence, pain sensitivity was highly increased during disrupted *LC-NA* circuitry (Jasmin et al., 2003; Tsuruoka et al., 2003; Bodnar et al., 1978). On the other hand, chemogenetic activation of the *LC-NE* induces anxiogenic and vigilant states, matching those occurring during natural stress responses. Activated *LC-PFC* circuitry induced anxiety-like behavior in rats (Zerbi et al., 2019; McCall et al., 2015; Hirschberg et al., 2017). Those different *LC-NE* functions coming from the branch trajectories across the centeral nervous system (CNS) as different regulations (efferents) and feedback implications (afferents) projections.

1.2.2. Anatomy of the *LC-NE* projection: afferents and efferents

Among catecholaminergic neuronal groups, *LC-NE* neurons have widespread axonal projections as well as a metabolic burden due to catecholamine synthesis that require these conserved cellular maintenance pathways such as autophagy for managing damaged organelles and proteins (Kazumasa Wakamatsu et al., 2015).

The *LC-NE* system is essential for the modulation of brain responses under both stressful and normal conditions. Its widely dispersed projections and modular input-output structure allow for the task-dependent activation of regions of the brain, hence, maintaining homeostasis during dynamic situations. The *LC-NE* system modulates attention, arousal, and vigilance. The effects of manipulation of *LC-NE* activity are significantly immense for these states. Optogenetic activation of *LC-NE* neurons modelled phasically elicits transitions from sleep into wakefulness, whereas reduced activation modeling tonic *LC-NE* activity modifies delta and theta rhythms during sleep, causing increased sensory-evoked awakenings. Inactivation of *LC-NE* activity curtails wakefulness, hence, emphasizing its role in vigilance (Aston-Jones & Bloom, 1981; Carter et al., 2010; Swift et al., 2018; Hayat et al., 2020).

LC-NE activity is finely tuned by way of local release of norepinephrine as well as afferent inputs originating from almost all brain regions. The peri-*LC-NE* zones include GABAergic interneurons that modulate *LC-NE* activity (Aston-Jones et al., 1991, 2004; Jin et al., 2016). The *PFC* provides the most robust excitatory input, maintaining tonic activation (Arnsten & Goldman-Rakic, 1984; Sesack et al., 1989; Jodo & Aston-Jones, 1997). Reciprocal connections with the amygdala regulate fear and anxiety via corticotropin-releasing factor (CRF) (Cederbaum & Aghajanian, 1978; Charney et al., 1998; Wallace et al., 1989). Hypothalamic nuclei regulate sleep-wake patterns and sympathetic activity via *LC-NE* projections (Szymusiak & McGinty, 2008; De Lecea et al., 1998; Korotkova et al., 2005). Brainstem structures, such as the ventral tegmental area and dorsal raphe nucleus, communicate with the *LC-NE* to regulate arousal and REM sleep (Monti & Jantos, 2008; Canteras et al., 2010). *LC-NE* neurons receive acute noxious inputs originating from the spinal cord via the nucleus paragigantocellularis and respond by descending *LC-NE* axons exerting analgesic effects on the spinal cord and medulla (Kimura & Nakamura, 1985; Craig, 1992; Palkovits et al., 1995).

LC-NE neurons exhibit distinct phasic and tonic modes of activity. The phasic mode consists of brief bursts of action potentials following the presentation of salient stimuli or top-down signals from the PFC (Aston-Jones & Bloom, 1981, 2005; Berridge & Waterhouse, 2003). Tonic mode consists of a slow, stochastic rate of firing that is positively correlated with states of arousal and task flexibility during wakefulness (Aston-Jones et al., 1997, 2005; Berridge & Waterhouse, 2003). During stress and anxiety, the *LC-NE* displays high tonic activity (Kane et al., 2017).

The *LC-NE* system regulates the state of arousal also through its reciprocal interactions with the PFC. Pupil size was positively related to states of arousal, and the optogenetic excitation of *LC-NE* neurons enhanced, whereas inactivation reduced states of arousal (Reimer et al., 2016; Breton-Provencher & Sur, 2019). Sustained phasic activation of *LC-NE* enhances arousal, while sustained tonic activation of *LC-NE* does not. This hyperactivation of *LC-NE* neurons yields anxiogenic behavior, demonstrating an inverted-U relationship between NE release and brain functioning (Valentino & Van Bockstaele, 2008; Yerkes & Dodson, 1908; Aston-Jones & Cohen, 2005).

In attention regulation, the *LC-NE* system enables high-salience information processing to suppress low-salience stimuli, mainly due to its action on PFC. GANE model posits that glutamate interacts with NE to amplify activity hotspots while suppressing less relevant information (Mather et al., 2016). *LC-NE* activity promotes the processing of sensory integration and the behavioral outcomes during challenging tasks (Aston-Jones & Cohen, 2005; Sara & Bouret, 2012). Lower age-related declines in *LC-NE* functionality reduce the capacity of suppression of information that is not salient during arousal and contributes to cognitive impairments (Lee et al., 2018).

LC-NE system profoundly affects hippocampal function through spatial navigation, memory, and stress-related behaviors. *LC-NE* activity was demonstrated to modulate hippocampal neurons by stimulating both β-adrenergic and α-adrenergic receptors, thereby influencing synaptic plasticity and memory processes (Pang & Rose, 1987; Bergles et al., 1996; Takeuchi et al., 2016). Norepinephrine was demonstrated to interact with dopamine to encode salience and aversive experiences involved in the formations of stress-responsive memory (Hansen & Manahan-Vaughan, 2015; Nguyen & Connor, 2019).

LC-NE projections to the amygdala integrate sensory information to generate stress-related responses. NE release in the basolateral amygdala conditions aversion, increases anxiety-like behavior, and impairs extinction learning (Llorca-Torralba et al., 2019; Giustino et al., 2020). Moreover, chemogenetic inactivation of the LC-BLA pathway reduced pain-induced anxiety and fear learning when induced by pain (Llorca-Torralba et al., 2019).

Antiepileptic action is also a kind of neuromodulation mediated via LC. Release of NE reduces seizure duration and propagation, while *LC-NE* lesions enhanced seizure activity (Giorgi et al., 2003, 2006, 2008). This action was further dampened by co-released neuropeptides galanin and neuropeptide Y (Mazarati et al., 1998, 2004).

The reciprocal connections of *LC-NE* with different regions outline that *LC-NE* has a leading role within a wide neuromodulatory network involved in arousal, attention, stress, pain modulation, and general neuromodulation.

Besides that, the autophagy pathways are also associated with the progressive accumulation of catecholamine by-products conferring on *LC-NE* neurons their dark blue color-for example, neuromelanin. This is relevant because dysfunction of these pathways could link to neurodegenerative diseases such as Alzheimer's and Parkinson's disease, wherein the noradrenergic system has been described to often play a role in. (Theofilas et al. 2017)

1.2.3. The role of endo-lysosomal system and autophagy in the *locus coeruleus*:

LC-NE neurons among the most burdened cells in the central nervous system, are characterized by their high sensitivity to neurodegeneration in both Alzheimer’s and Parkinson’s disease. Age- and disease-dependent modifications in their endo-lysosomal system and neuroprotective autophagy suggest that both systems are critically involved in the elimination of polymerized catecholamine derivatives, such as neuromelanin (NM), an early biomarker of Parkinson's disease (Zucca et al., 2018; Yamaguchi et al., 2018; reviewed in Lu et al., 2020; Rubinsztein & Nixon, 2024). In this context, autophagy plays a crucial role in maintaining the viability of noradrenergic neurons under various stressful conditions, including those induced by pharmacological and neurotoxic agents (Ferrucci et al., 2013; reviewed in Limanaqi et al., 2020). Recent snRNA-seq profiling of the neurotypical adult human *LC-NE* aimed at comparing *NE*-positive neurons, identified and characterized by their gene expression signatures in the *LC-NE* versus the surrounding regions, found the autophagy marker mRNA **MAP1LC3B** among the top 70 significantly elevated genes (Weber et al., 2023), indicating a high demand for autophagy regulation in these neurons.

The activity of *LC-NE* neurons is intricately linked to the modulation of wakefulness and various sleep phases, which, in turn, correlates with the oscillatory amplitude of NE release, which plays a crucial role in shaping the microarchitecture of sleep associated with memory performance (Kjaerby et al., 2022). Some studies address the role of insufficient sleep resulting in cognitive impairments (Tartar et al., 2009; Ramesh et al., 2012; Stickgold et al., 2013) and propose that it affects the clearance of metabolic wastes and disrupts intracellular protein degradation pathways, including endosome-autophagosome-lysosome (EAL) pathways as evident by accumulation and dysregulation of cellular LAMP1-positive lysosomes (Xie et al., 2013; Xie et al., 2022).

Oscillations of NE released from *LC-NE* synaptic boutons are detected by a family of adrenergic GPCRs, including β2- and α2-adrenergic receptors (AR), each with distinct functions. The activation of β2- and α2AR plays a pivotal role in modulating the wake-sleep cycle, with their activities and downstream signaling being differentially influenced by NE levels (Xu et al., 2003; Wang & Limbird, 2002; 2007; *Fig. 2*). Adrenergic signaling plays a critical role in maintaining wakefulness and regulating REM sleep, during which *LC-NE* neurons exhibit reduced activity (Aston-Jones & Bloom, 1981) and spontaneously released NE predominantly interacts with α2AR, initiating downstream Gαi/o-protein coupled signaling and leading to the inhibition of cAMP/PKA signaling (Saunders et al., 1999). Furthermore, the higher affinity of α2AR for NE compared to β2AR (Lakhlani et al., 1997) suggests that during wakefulness, elevated NE levels primarily activate β2AR, triggering downstream Gαs-protein coupled signaling and subsequently activating the cAMP/PKA pathway.

While the consequences of activating β2AR or α2AR on the membrane of *LC-NE* neurons remain unclear, their influence on autophagy processes in general is increasingly recognized. A growing body of evidence underscores the significance of β2ARs in regulating endo-lysosomal and autophagy-related processes in both non-neuronal cells and neurons. This regulatory role is recognized as vital for maintaining cellular proteostasis (Farah et al., 2014; Campos et al., 2020; reviewed in Giorgi et al., 2017; Lee et al., 2020). For instance, in the context of neurogenic myopathy, the activation of β2ARs by agonists in the skeletal muscles of mice serves as a protective measure against the disturbance of autophagy flux, thereby maintaining the integrity of skeletal muscle proteostasis and contractile properties (Campos et al., 2020). Similarly, the stimulation of β2AR with isoproterenol, norepinephrine, and salbutamol has been found to increase autophagy flux in cardiac fibroblasts (Aránguiz-Urroz et al., 2011). In line with this, in hepatic cells, the administration of the β2AR agonist clenbuterol stimulates autophagy flux, while the β2AR antagonist propranolol produces opposing effects (Farah et al., 2014). Multiple GPCRs, including AR, have been reported to be involved in autophagy regulation, highlighting the integration of several GPCRs and autophagy at both physiological and pathological levels (Reviewed in Öz-Arslan et al., 2024a, b). Remarkably, activation of β2AR by related agonists restores lysosomal proteolysis by re-acidifying lysosomes in the context of PSEN1 familial Alzheimer's disease (FAD). This activation rescues lysosomal hydrolase activity and autophagy flux, effectively reducing the abnormal accumulation of autophagic vesicles (Lee et al., 2020; Lee & Nixon, 2022). Therefore, <u>exploring of the impact of sleep on the regulation of neuronal proteostasis through autophagy is a captivating field of research</u>, with a potential for developing therapeutic applications aimed at enhancing sleep quality in preventing neurodegenerative processes.

1.2.4. Genetically Encoded Sensors for Neurotransmitter Dynamics

Genetically encoded sensors have transformed our understanding of neurotransmitter dynamics by providing real-time, spatiotemporal insights into synaptic communication and neuromodulation (Tian et al., 2009; Marvin et al., 2011). The evolution began with FRET-based sensors that suffered from sensitivity and temporal resolution limitations (Miyawaki et al., 1997). The second generation introduced single-fluorophore GRAB sensors based on G-protein-coupled receptor activation (Sun et al., 2018), exemplified by GRABNE2h with impressive performance metrics (230% $\Delta F/F_0$, nanomolar sensitivity, sub-second kinetics) (Feng et al., 2019). These sensors have illuminated key neurotransmitter functions: dopaminergic signaling in reward processing (GRAB_DA) (Patriarchi et al., 2018), serotonin's role in mood regulation (Unger et al., 2020), and acetylcholine's function in attention (Jing et al., 2020). Integration with electrophysiology and calcium imaging has revealed circuit-level mechanisms (Lin et al., 2020). GRABNE specifically has advanced understanding of norepinephrine's role in arousal and stress responses (Chen et al., 2021). In freely moving animals, these tools link neurotransmitter dynamics to complex behaviors like decision-making and memory formation (Zhang et al., 2021). Key discoveries include rhythmic norepinephrine release during sleep (Van Dort et al., 2015) and dopamine dynamics correlating with reward prediction error (Schultz et al., 1997). They've also provided insights into neuropsychiatric disorders (Ross et al., 2016; Stedehouder et al., 2021).

The field continues advancing toward finer temporal resolution, expanded neurotransmitter targets (Knoflach et al., 2001; Marvin et al., 2013), and multiplex imaging capabilities (Xie et al., 2021). When combined with optogenetics and chemogenetics, these tools enable simultaneous intervention and observation with unprecedented specificity (Deisseroth, 2011). GRABNE2h has proven particularly valuable for studying locus coeruleus activity, showing 10-15% $\Delta F/F_0$ during spontaneous activity (Chen et al., 2021) and providing critical insights into norepinephrine-driven modulation in the brain (Aston-Jones et al., 1991; Feng et al., 2019).

1.3. Cell-to-cell communication and non-cell autonomous autophagy

In recent years, it has become increasingly clear that a deeper understanding of cell-to-cell communication is essential for fully comprehending both homeostatic and pathological states of the brain. A critical aspect of this understanding is the role of autophagy in mediating these processes through its secretory function (Piletic et al., 2023). It has been proposed that **secretory autophagy**, facilitated by extracellular vesicle particles, serves as an alternative mechanism for clearing sequestered material and maintaining proteostasis in the event of endo-lysosomal dysfunction (Solvik et al., 2022; Burbidge et al., 2022; Cashikar and Hanson, 2019; Mauthe et al., 2018). Furthermore, it is conceivable that small extracellular vesicle particles mediate specific inter-neuronal communication, as recently suggested (reviewed in Nieves Torres & Lee, 2023).

Neurons of the *Me5* nucleus located adjacent to the *LC-NE* and receiving direct projections from *LC-NE* neurons (Takahashi et al., 2010), have been shown to relate to the *LC-NE* both anatomically and functionally through the exchange of membranous compartments (Goto et al., 2020). The neuronal cell bodies of *Me5* are significantly larger than the somata of *LC-NE* neurons, providing a greater capacity to accommodate endo-lysosomal and auto-lysosomal machinery that could potentially kick in on demand, functioning as an accessory digestive system to maintain *LC-NE* proteostasis.

However, it remains unclear whether the vesicular exchange between the *LC-NE* and *Me5* involves **secretory autophagy** mechanisms, what role heightened *LC-NE* activity plays in this process, and how *LC-NE* activity/ inactivity states regulate the exchange of membranous compartments originating from the *LC-NE* and taken up by *Me5*.

1.4. Aim of the thesis

The **overarching goal of my doctoral thesis** is to understand how network-related, cellular and molecular mechanisms regulate the waste clearance in *LC-NE* neurons through autophagy during different states of the *LC-NE* activity and various animal behaviors in wakefulness.

Based on the literature, I propose the following **molecular hypothesis**: During wakefulness and periods of high *LC-NE* activity, elevated *NE* release activates β2-adrenergic receptors (β2AR) as autoreceptors. This activation stimulates the cAMP/PKA pathway, leading to dissociation of autophagic vesicles from the dynein motor complex, resulting in vesicle immobilization or "stopping." Conversely, during sleep when *LC-NE* is relatively silent and *NE* release is low, α2-adrenergic receptors (α2AR) engage in a positive feedback mechanism that inhibits cAMP/PKA signaling, thereby promoting the reassociation of AVs with the dynein motor complex and enhancing retrograde trafficking (*Fig. 10*).

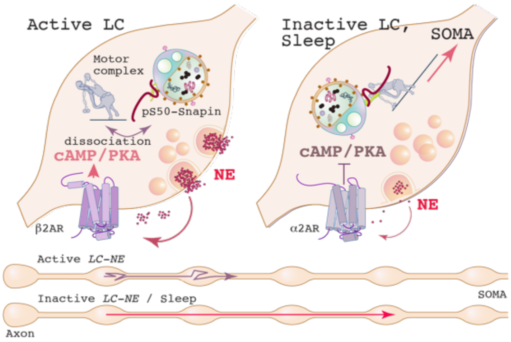

Figure 10| Molecular hypothesis of cAMP/PKA-dependent regulation of LC3B -positive vesicle trafficking in LC-NE axon *(Graphics used with permission from Dr. Anna Karpova).*

To prove this hypothesis, I investigated the dynamics of autophagic vesicles trafficking across *LC-NE* distal axons projecting to the PFC during different *LC-NE* activity states, addressing the following questions:

1. How do autophagic vesicles navigate through the long-ranging *LC-NE* axons during spontaneous *LC-NE* activity?

   I addressed this question by studying the LC3B-positive vesicle trafficking dynamics in distal *LC-NE* axons using an AAV-based labeling approach and *in vivo* two-photon microscopy through a transcranial window.

2. How does chemogenetic manipulation of *LC-NE* neurons impact autophagic vesicle trafficking velocity and trafficking patterns?

I hypothesize that *LC-NE* inactivation facilitates retrograde vesicle trafficking along distal axonal projections, accelerating the delivery of autophagic vesicles to *LC-NE* somata.

3. Do AVs necessitate to traffic all the way from rare terminal location (*PFC*) to the soma?

I investigated whether autophagic vesicles require complete retrograde transport to the cell soma for autolysosomal formation, or if this process can occur locally within axonal terminals where lysosomal vesicles may be present.

4. How do behavioral states, such as anxiety-like behavior versus spontaneous *LC-NE* activity, alter the dynamics of AV trafficking in distal *LC-NE* axons?

5. How does *NE* release regulate AV trafficking velocity, directionality, and dynamics across the axonal terminal?

6. What is the underlining molecular mechanism of AV trafficking in relation with *LC-NE* activity?

Previous observations in the lab suggest that SIPA1L2 is part of a protein complex with spinophilin, the scaffolding protein and regulatory subunit of protein phosphatase-1 (PP1). The mechanism underlying AV immobilization involves the phosphorylation of the dynein adaptor protein SNAPIN. In collaboration with Anna Karpova, we found that spinophilin, via SIPA1L2, recruits SNAPIN and may locally regulate its dephosphorylation, facilitating its subsequent reassociation with the dynein motor complex. This process may enable LC3B+ vesicle mobilization in response to cAMP/PKA signaling downstream of β2AR activation.

7. Does the *LC-NE* employ an alternative mechanism, such as degradative autophagy, for cargo disposal?

I observed a lower density of lysosomal vesicles in the *LC-NE* soma compared to the adjacent *Me5* neurons. This finding led to the intriguing hypothesis that *Me5* neurons may contribute to degradative processes, thereby supporting the highly vulnerable *LC-NE* neurons.

2. Materials and Methods

2.1. Experimental models and animals:

All *in vivo* animal experimental procedures were approved by the responsible authorities of Saxony-Anhalt (SA, Landesverwaltungsamt für Verbraucherschutz und Veterinärangelegenheiten, Referat 203; License number 42502-2-1638 LIN). B6.Cg-Dbhtm3.2(cre)Pjen/J (Strain #:033951 RRID:IMSR_JAX:033951) and C57BL/6J Strain #:000664 RRID:IMSR_JAX:000664) mouse lines were obtained from the Jackson Laboratory and maintained at animal facility at the LIN. The average age of the animals for surgical procedures was between 10-12 weeks old and all animals were treated according to the animal welfare guidelines of the Leibniz Institute for Neurobiology. Primary neuronal cell cultures were prepared from embryonic Sprague-Dawely rats (Janvier Labs, Le Genest-Saint-Isle, France). Rat cortices and hippocampi cell culture animal license (Töten zu wissenschaftlichen Zwecken -TWZ license- according to section 4 paragraph 3, German animal welfare act).

2.2. Materials

2.2.1. Surgical materials

The surgical materials used in the present study, along with their brief descriptions, are summarized in the Table 1.

Table 1. (Surgical materials and tools):

Name	**Purpose**	**Supplier / Cat.#Number**
Microscope Coverslip 5mm (Glass, #1.5) Fisherbrand™ Cover Glasses: Circles	Used to create the transcranial window by covering the exposed brain tissue.	Fisher Scientific, Cat.:#12-545-80
Dental Cement (e.g., Metabond) Paladur® Flüssigkeit Paladur® Pulver- rosa	Secures the coverslip to the skull and seals the window.	Pluradent supply Cat. :#46578 & #41101
Cranial Drill (High-Speed Rotary Tool) & Drill heads #007	Used to thin or remove part of the skull to expose the brain.	SERZG # DB1010 Dental bauer (#477128&# 474205)
Sterile (0.9%NaCl) Saline Solution	Keeps the exposed brain tissue hydrated during surgery.	Sigma-Aldrich, Cat.:# S8776
Gelfoam (Absorbable gelatin)	Controls bleeding during the surgical procedure.	Pfizer (09-0400-04)

Microsurgical Instruments (Scalpel, Forceps, Scissors, Needle Holder, etc.)	For precise dissection and manipulation of tissues during surgery.	fine science tool: Cat. # 12102-12 &# 12004-16 &# 11412-11 &# 14040-10 &# 14084-09
Isoflurane	Induces and maintains anesthesia during the surgical procedure.	Patterson Veterinary (07-893-4101)
Stereotaxic Frame	To immobilize the mouse's head during the surgery.	RWD (#68801 &# 68055&# 68057& # 68306 &# 68218
Suture Materials VICRYL™ 70 cm USP 2-0	Used for closing the wound after the procedure is complete.	Ethicon, Cat.:# Y312H
Heating Pad	Maintains the constant animal's body temperature during the surgery.	Kent Scientific (TP-700)
Headplate	For head fixation under microscopic objective	Custom made
Fiber Optic Cannula, Ø1.25 mm SS Ferrule, Ø400 µm Core, 0.50 NA, L=5 mm	Used to deliver light to mPFC for photo-stimulation of mEOS4-LC3B (405 nm).	Thorlabs (CFML15L05)
Ketamin 100mg/kg	For Animal Anesthesia	Ketabel "R1218-15"
Xylazine 20mg/kg	For Animal Anesthesia	Serumwerk "9435/02"
Carpofen 5mg/kg (Rimadyl, 50mg/ml)	Anti-inflamatory for post-surgery caring	Zoetic (400684.00)
Syring for viral injection (Nanofill syringe)	For virus injection in the brain tissue	WBI (NANOFIL-100)
Suturing kit (1.5mm)	For skin closure post-surgery	WDT "94030"
Nano-induction pump	For nano-induction of viral injection	WBI "MICRO21"
Plurafill "UV dental cement"	Adhesive for headplate	PLULINE (246126)
Superbond mixture	Adhesive for coverslip and headplate	C&B superbond "7120-200"
4X objective (NA=0.1) - PlanN	For two-photon microscopic imaging	Olympus "ULS-2"
40X objective (NA=0.8) - PlanW	For two-photon microscopic imaging	Nikon "3013438"

2.2.2. Antibodies

Primary and secondary antibodies used for immunohistochemical, immunocytochemical and western blot analysis are listed in tables 2.

Table 2. Antibodies:

REAGENT or RESOURCE	SOURCE	IDENTIFIER
Primary Antibodies		
Anti-TH (Guinea pig polyclonal)	Synaptic Systems	CAT.# 213104
Anti-TH (Rabbit)	Millipore	CAT.# AB152
Anti- LAMP2 (Rat)	ThermoFischer	CAT.# MA1-165

Anti- LAMP1 (Rabbit)	Proteintech	CAT.# 21997-1-AD
Anti- SIPA1L2 (Rabbit)	Gundelfinger´s lab	In house
Anti- GFP (mouse monoclonal)	ThermoFischer	CAT.# A11120
Anti- GFP (Rabbit monoclonal)	Abcam	CAT.# ab6556
Anti- Spinophilin (Rabbit)	Proteintech	CAT.# 55129-1-AP
Anti-LC3B (Mouse)	MBL International	Cat. #M152-3
Anti-MAP2 (Guinea pig monoclonal)	Sigma	CAT.# M-4403
Anti-p62 (Guinea pig)	Progen	CAT.# GP02-C
Anti-panATG16L	Thermo Fisher	CAT.# PA1-18296
Anti-Sec22B	Proteintech	Cat. #14776-1-AP
Anti-beta2AR	Alomone lab	Cat. #AAR-016-PE
DAPI	Thermo Fisher	CAT.# D3571
Secondary Antibodies		
Goat anti-mouse IgG, Alexa Fluor 405	Invitrogen	Cat.# A-31553;
Alexa Fluor 405 anti-rb (goat)	Abcam	Cat.# ab175652
Alexa Fluor 405 anti-gp (goat)	Abcam	Cat.# ab175678
Alexa Fluor 488 anti-ms (goat)	Invitrogen	Cat.# A32723
Alexa Fluor 488 anti-rb (goat)	Invitrogen	Cat.# A11034
Alexa Fluor 488 anti-gp (goat)	Invitrogen	Cat.# A11073
Alexa Fluor 488 anti-rat (goat)	Invitrogen	Cat.# A11006
Alexa Fluor 568 anti-ms (goat)	Invitrogen	Cat.# A11031
Alexa Fluor 568 anti-rb (goat)	Invitrogen	Cat.# A11036
Alexa Fluor 568 anti-gp (goat)	Invitrogen	Cat.# A11075
Alexa Fluor 568 anti-rat (goat)	Invitrogen	Cat.# A11077
Alexa Fluor 633 anti-rb (goat)	Invitrogen	Cat.# A21070
Alexa Fluor 633 anti-rat (goat)	Invitrogen	Cat.# A21094
Alexa Fluor 647 anti-gp (goat)	Invitrogen	Cat.# A21450
Alexa Fluor 647 anti-ms (goat)	Invitrogen	Cat.# A21236

2.2.3. Common buffers and reagents:

The used buffers and reagents in the present study, along with their brief descriptions, are summarized in the Table 3.

Table 3. Common buffers and reagents

REAGENT or RESOURCE			SOURCE	IDENTIFIER
Buffers				
Buffer/Medium	**Application**	**Composition**	**Supplier**	**Cat.#**
Phosphate Buffered Saline (PBS) PH 7.4	Washing of cells and tissue samples	NaCl: 140 mM	Sigma-Aldrich	S5886
		Na_2HPO_4: 8.3 mM	Sigma-Aldrich	S5136
		NaH_2PO_4: 1.7 mM	Sigma-Aldrich	S0751
Blocking Buffer	Immunocytochemical and immunohistochemical detection of epitopes	Horse serum: 10%	Sigma-Aldrich	H1138
		Triton X-100: 0.3%	Sigma-Aldrich	T8787
		PBS: 1x	See above	See above

Mowiol	Mounting tissues and cultured cells on microscopic slides	Mowiol 4-88: 10% (w/v)	Sigma-Aldrich	81381
		Glycerol: 25% (v/v)	Sigma-Aldrich	G5516
		Tris Buffer (pH 8.5, 0.2 M): 50%	Sigma-Aldrich	T6066
PFA Fixation Buffer	Animal perfusion and tissue fixation	Paraformaldehyde: 4% (w/v)	Sigma-Aldrich	158127
		PBS: 1x	See above	See above
Sucrose Buffer	Immunohistochemistry (IHC)	Sucrose: 30% (w/v)	Sigma-Aldrich	S0389
		PBS or Phosphate Buffer: 1x	See above	See above
PLL Coating Solution	Coating of coverslips for cell culture and microchambers	Poly-L-Lysine: 0.01% (w/v)	Sigma-Aldrich	P1524
		Sterile distilled water	N/A	N/A
Citric Acid Buffer	Antigen retrieval	Citric Acid Monohydrate: 0.1 M	Sigma-Aldrich	C1909
		Sodium Citrate Dihydrate: 0.1 M	Sigma-Aldrich	S4641
		Distilled Water	N/A	N/A
CTS™ Neurobasal™-A Medium	Maintenance of hippocampal neurons	Neurobasal Medium	Gibco™, Thermo Fisher Scientific	21103049
		B-27 Supplement (without vitamin A)	Gibco™, Thermo Fisher Scientific	17504044
DMEM	Maintenance of HEK293T cells	DMEM	Sigma-Aldrich	D5671
		Fetal Bovine Serum (FBS), 10%	Sigma-Aldrich	F2442
		Penicillin-Streptomycin, 1%	Sigma-Aldrich	P4333
MEM	Treatment of HEK293T cells	MEM	Sigma-Aldrich	M2279
		Fetal Bovine Serum (FBS), 10%	Sigma-Aldrich	F2442
		Penicillin-Streptomycin, 1%	Sigma-Aldrich	P4333
JHU37160 dihydrochloride (water soluble)	(DREADD ligand)	0.3 mg/kg	Hello Bio	HB6261
Neurobasal-A Medium		Neurobasal-A Medium	Thermo Fisher Scientific	A2473301

	Differentiation of hippocampal neurons	B-27 Supplement (with vitamin A)	Thermo Fisher Scientific	17504044
RPMI-1640	Alternative maintenance for HEK293 cells	RPMI-1640	Thermo Fisher Scientific	11875093
		Fetal Bovine Serum (FBS), 10%	Sigma-Aldrich	F2442
		Penicillin-Streptomycin, 1%	Sigma-Aldrich	P4333
Standard ACSF pH: 7.4 (adjusted with HCl or NaOH) & Osmolarity: ~310 mOsm/kg	General maintenance of brain acute slices	NaCl: 124 mM	Sigma-Aldrich	S5886
		KCl: 3.0 mM	Sigma-Aldrich	P5405
		$MgSO_4$: 1.3 mM	Sigma-Aldrich	M2643
		$CaCl_2$: 2.5 mM	Sigma-Aldrich	C3881
		NaH_2PO_4: 1.2 mM	Sigma-Aldrich	S8282
		$NaHCO_3$: 26.0 mM	Sigma-Aldrich	S5761
		Glucose: 10.0 mM	Sigma-Aldrich	G8270
Low Magnesium ACSF pH: 7.4 (adjusted with HCl or NaOH) & Osmolarity: ~310 mOsm/kg	Recovery of acute slices	NaCl: 124 mM	Sigma-Aldrich	S5886
		KCl: 3.0 mM	Sigma-Aldrich	P5405
		$MgSO_4$: 0.6 mM	Sigma-Aldrich	M2643
		$CaCl_2$: 2.5 mM	Sigma-Aldrich	C3881
		NaH_2PO_4: 1.2 mM	Sigma-Aldrich	S8282
		$NaHCO_3$: 26.0 mM	Sigma-Aldrich	S5761
		Glucose: 10.0 mM	Sigma-Aldrich	G8270
High Calcium ACSF pH: 7.4 (adjusted with HCl or NaOH)& Osmolarity: ~310 mOsm/kg	Recording/imaging buffer	NaCl: 124 mM	Sigma-Aldrich	S5886
		KCl: 3.0 mM	Sigma-Aldrich	P5405
		$MgSO_4$: 1.3 mM	Sigma-Aldrich	M2643
		$CaCl_2$: 4.0 mM	Sigma-Aldrich	C3881
		NaH_2PO_4: 1.2 mM	Sigma-Aldrich	S8282
		Glucose: 10.0 mM	Sigma-Aldrich	G8270

2.2.4. Oligonucleotides, recombinant DNA and adeno-associated viruses (AAVs)

The used Oligonucleotides, recombinant DNA and AAVs in the present study, along with their brief descriptions, are summarized in the Table 4.

Table 4. Oligonucleotides, recombinant DNA and adeno-associated viruses (AAVs)

REAGENT or RESOURCE	**SOURCE**	**IDENTIFIER**
Oligonucleotides		
Mouse Genopyping primers WT , F 5′ AGG CAT AAA TGG CAG AGT GG 3’	Rachel P Tillage, et al. 2020	ntegrated DNA Technologies (IDT)
Mouse Genopyping primers WT R 5′ TGG AGC TGG AAG TGG ATG AT 3′		
Mouse Genopyping primers Mutant R 5’ CAT GTC CAT CAG GTT CTT GC ‘3		
Recombinant DNA		
pAAV-EF1a-DIO-mNeonGreen-LC3B	AAV production	Addgene #50462 (backbone) This study
pAAV-EF1a-DIO-mRuby3-LC3B	AAV production	This study
pAAV-EF1a-DIO-mEOS4-LC3B	AAV production	This study
AAVs / Titer		
AAV-EF1a-DIO-mNeonGreen-LC3B , DJ (1.9x10^12vg/ml)	(this work); In vivo and in vitro CRE-dependent labeling of autophagic vesicles in green	This work; Addgene#50462 backbone
AAV-EF1a-DIO-mRuby3-LC3B , DJ 2,3x10^12 vg/ml	(this work); In vivo and in vitro CRE-dependent labeling of autophagic vesicles	this study
AAV-EF1a-DIO-mEOS4-LC3B , AAV2/9 3,24x10^13 vg/ml	(this work); In vivo and in vitro CRE-dependent labeling of autophagic vesicles	this study
AAV-CBh-DIO-EGFP, DJ 2,16x10^13 vg/ml	Addgene; Expression of eGFP in the presence of Cre	Addgene #87168
AAV-hSyn-GRAB-NE2h, AAV2/9 (1.7x10^13 vc/ml)	Addgene; Neuron-specific in vivo expression of NE sensor detecting NE release	Addgene #208687
AAV-hEF1a-dlox-hM4D(Gi)_mCherry_dlox_WPRE_bGH(pa) (8.2x10E12 vg/ml)	(this work); Pharmacogenetic inhibition for Cre recombinase-expressing cells	V104
AAV-hEF1a-iCre-WPRE-bGH(pA) (6.4x10^12 vg/ml)	Zurich Viral Vector; Cre recombinase expression for terminal-specific cells	V225

AAV-hSyn-eGFP-iCre-WPRE-bGH(pA) (6,1x10^12 vg/ml)	Zurich Viral Vector; Cre recombinase expression for terminal-specific cells with green label	V229

2.3. Methods

2.3.1. Cloning of viral constructs and viral particle production

The open reading frames (ORFs) for mNeonGreen-LC3B mRubi-LC3B and mEOS4-LC3B were sourced from IDT (Integrated DNA Technologies) as gBlocks and subsequently subcloned into the AAV-EF1α-DIO (Addgene#50462 for the backbone) using SgsI/AscI-Nhe1 restriction sites (Table 4 for details). AAV particles expressing LC3B targeted with fluorescent proteins were generated using DJ and AAV9 serotypes, either produced at the LIN (Magdeburg), at the UKE Vector Facility (Hamburg) or obtained from the Addgene and Zurich Viral Vector facility as a ready to use viral particles (Table 4).

2.2.2. Molecular cloning and purification of plasmid DNA (Miniprep)

For restriction, DNA constructs were treated with restriction enzymes (NEB) and incubated at 37°C for 2-3 h. The products were separated on an agarose gel (1%) with GelRed (Millipore, SCT123) and respective bands cut out and purified with the Nucleospin Gel and PCR clean-up kit (Macherey-Nagel, 740609.50). For ligation, 50 ng of backbone DNA was mixed with insert DNA at a molar ratio of 1:3 and incubated for 3 h at RT or o.n. at 4°C with T4 ligase (Promega, M1804). Subsequently, DNA was transformed into bacteria (E.coli XL10-Gold) via heat shock at 42°C for 45-50 sec. Bacteria were chilled on ice for 2-3 minutes and then incubated in SOC-medium at 37°C for 1 h, before they were transferred onto LB-plates with respective antibiotics and incubated o.n. at 37°C. Single colonies were picked and incubated in 2.5 mL LB medium with respective antibiotics o.n. at 37°C on a shaker. Bacterial DNA was isolated as described below, eluted in water and sent for sequencing (Microsynth, Balgach, Switzerland).

For isolation of plasmids from 2.5 mL bacterial solution (Miniprep), bacterial were pelleted by centrifugation at 3500 xg for 3 minutes at 4°C in 2 mL Eppendorf tubes. The supernatant was discarded and pellets resuspended in 300 µL resuspension buffer (500 mM Tris-HCl, 10 mM EDTA, 100 µg/mL RNaseA (EN0531, ThermoFisher);

pH 8.0). Then 300 µL lysis buffer (200 mM NaOH, 1% SDS) was added, tubes were inverted, followed by addition of 300 µL neutralization buffer (3 M potassium acetate; pH 5.5, adjusted with acetic acid) was added. Tubes were inverted again and centrifuged for 3 minutes at max speed and 4°C. The supernatant was transferred into new tubes, which were again centrifuged to remove remaining debris. The supernatant was again transferred into new tubes (1.5 mL Eppendorf). To precipitate DNA, 700 µL isopropanol were added and tubes were mixed vigorously before centrifugation for 5 minutes at max speed and 4°C. Isopropanol was discarded and 200 µL ethanol (70%) was added to solubilize precipitated salts. Tubes were again centrifuged for 5 minutes at max speed and 4°C. Ethanol was discarded and pellets were either dried o.n. at RT under a hood or via lyophilization (FreeZone 2.5, Labconco) at for 10 minutes at -20°C and 20 Pa while rotating (Univapo 150 ECH, UniEquip). Pellets were eluted in 25 µL H2O.

2.3.3. Adeno Associated Virus (AAV) Generation

For production of crude AAV, HEK293T cells were transfected with PEI with plasmids from the scAAV/DJ Helper Free expression system (Cell Biolabs, VPK-430-DJ-8). The expression vector, pAAV-DJ and pHelper were mixed at a molar ratio of 1:1:1. After 3 days of expression, cells were harvested. First, cells were washed with 10 mL warm PBS solution and then resuspended in 10 mL of warm PBS with a cell scraper. The suspension was collected in 50 mL falcons and centrifuged at 1000xg at 4°C for 30 minutes. The supernatant was discarded and pellets frozen at -80°C. Pellets were thawed and resuspended and up to 4 petri dished pooled in 5 mL Tris-HCl-buffer (20 mM Tris base, 150 mM NaCl; pH 8.0 with HCl). The solution was frozen and thawed (10 minutes in ethanol-dry ice mix, 10 min at 37°C) three times for lysis. After the last thaw step, benzonase (Sigma, E1014-25KU) (final conc. 50 U/mL) was added and suspension incubated for 1 h at 37°C and inverted from time to time. Then the mix was centrifuged at 4000-8000xg for 15-30 minutes and the supernatant was passed through a 0.2 µm microfilter for sterilization. Crude virus fractions were stored at 4°C. For animal use, the viral particles were purified using ultracentrifugation. Cesium chloride (CsCl) gradient ultracentrifugation was employed to separate the viral particles based on their buoyant density. Two clorid buffers were prepared CsCl at densities of approximately 1.4 g/mL and 1.25 g/mL. These were carefully loaded into ultracentrifuge tubes to create a visaly separated gradient. The clarified virus-containing supernatant, obtained by centrifuging the crude lysate at 10,000g for 20 minutes to remove debris, was then loaded on top of the CsCl gradient. The tubes were centrifuged in a swinging bucket rotor at 100,000g for 16-24 hours at 4°C. Following centrifugation, a distinct viral band, located at a density of approximately 1.37 g/mL, was collected using a syringe with a fine needle. The collected viral fractions were then dialyzed against PBS to remove the CsCl over a 24-hour period with multiple washing steps. Alternatively, size-exclusion chromatography was used for further purification. If necessary, the viral particles were concentrated using a centrifugal filter (Amicon Ultra with a 100 kDa cutoff). The viral titer was then determined using quantitative PCR (qPCR), and the purified virus was aliquoted and stored at -80°C in a PBS buffer containing 5% glycerol for long-term use.

2.3.4. Virus injection surgery

Prior to AAV injections, animals were anesthetized using a ketamine/xylazine mixture in concentrations 100 mg/kg for ketamine and 5 mg/kg for xylazine respectively injected intraperitoneal (IP). This combination effectively sedated the animal, ensuring it remained immobile and pain-free during the surgical procedure. Following anesthesia, the skull was fixated in a sterotactial setup (Table 1) and exposed above the region of interest by making an incision in the skin. After securing the surgical field by fixating the cutted skin and scrating the connective tissues from top of main sutures, a clear access for pregma and lamda was achieved. For targeting *Locus coeruleus* and ensuring precise localization of the AAV delivery, the following coordinates were defined using the mouse Allen Brain Atlas: anterior-posterior (AP) = -5.4 mm, medial-lateral (ML) = ±0.93 mm, and dorsal-ventral (DV) = -3.6 mm. Subsequently, a small hole, 0.1-0.2 mm in diameter, was drilled into the exposed skull at the designated location, taking care to avoid excessive damage. After confirming that the drilled hole was clean and free of debris, a micro-injection syringe (Table 1) was filled with the virus intended for injection and was carefully placed into a nano-induction pump (Table1) for slow injection in the brain.To minimize brain tissue distortion, a needle was then slowly introduced into the brain at a controlled speed (indicate the speed) until it reached the desired depth of -3.6 mm, which corresponds to the *LC-NE* region. Once the needle was in place, it was kept immobilized for additional 5 minutes to allow brain tissue to decompress from the **mechanical deformation** before commencing the injection. The virus was injected at a total volume of 500 nl, with an average injection rate of 75 nl/min (Cassia N. Cearley and John H. Wolfe, 2007). This slow, controlled injection process helped to minimize tissue damage or deformation and ensure even distribution of the virus within the targeted area. After the injection was complete, an additional 10 minutes was allowed for the viral load to distribute within the local region before the needle was carefully withdrawn at a steady, slow speed (0.1–0.2 mm/sec). This step was critical to minimizing tissue damage during needle removal. Following the AAV injection procedure, the exposed skull was closed by suturing the skin using a suturing kit (Table 1) The sutures were carefully placed to ensure proper wound closure and healing, 1 stitch for each mm cut in the skin been performed with 3-4 noddes each stitch. Post-surgical procedures were then followed to ensure the animal's recovery and well-being after securing the full closure of skin incision using a silk suture and dental cement according to surgery, animals were observed during the period of waking up from anesthesia to monitor all vital indicators for well-being (motor-function, social interaction, and pain indications). Three days post-surgery, animals been taken care off by the experimenter by checking the healing process and administrate analgesia medication (Carprofen 5mg/kg) subcutaneously injected during the close caring period. All animals been checked daily during the experiment timeline from the start of surgery till brain tissue collection.

2.3.5. Optical fiber implantation

For fiber implantation, animal preparation and skull exposure were performed as described for AAV injections methods 2.2.2. Additionally, a 300 μm diameter hole was drilled above the right brain hemisphere on top of the *PFC*. The coordinates for the hole were precisely located at anterior-posterior (AP) +1.8 mm and medial-lateral (ML) +0.3 mm in relation to Bregma. Subsequently, an optical fiber (with 300μm diameter and 0.5NA) targeting the medial *PFC* (mPFC) ensuring minimized tissue deformation was introduced into the brain to a depth of dorsal-ventral (DV) -2.2 mm the fiber inserion occurred on average rate of 1-2mm/sec. After securing the stability of the fiber in desired place using a dental cement applied around the insertion site, the surgical site was closed by suturing the skin, following the standard post-surgical procedures. Animals were observed during the period of waking up from anesthesia to monitor all vital indicators for well-being (motor-function, social interaction, and pain indications). Three days post-surgery, animals been taken care off by the experimenter by checking the healing process and administrate analgesia medication (Carprofen 5mg/kg) subcutaneously injected during the close caring period. All animals been checked daily during the experiment timeline from the start of surgery till brain tissue collection.

2.2.6. Transcranial window implantation

The animal was anesthetized and prepared following the procedures described in section 2.2.2. **Virus injection surgery** with the differences that bigger area of the skull was exposed. Next, the connective tissue on the bone surface was carefully roughened by scratching to prepare it for cranial window implantation. A 5 mm circular craniotomy was marked over the skull, covering the prefrontal and motor cortex regions, which were identified as the areas of interest using the Allen Mouse Brain Atlas (Zuluaga-Ramirez et al., 2015). A high-speed micro drill (specifications in Table 1) was then used to carefully cut around the marked area. To mitigate heat-induced tissue damage, sterile saline was continuously irrigated over the site to cool the area and reduce frictional heat during the drilling process (Goldey et al., 2014). This consistent application of saline also facilitated the gradual detachment of the skull from the dura mater by softening the cut edges, allowing for the gentle removal of the bone with minimal trauma to the underlying brain tissue. Once the edges were fully loosened, an additional application of saline was used to carefully lift the bone fragment without disrupting the dura mater (Xu et al., 2007). Throughout the procedure, careful attention was given to minimizing bleeding, ensuring optimal exposure of the brain while keeping the dura intact (Mostany & Portera-Cailliau, 2008). After thoroughly cleaning the area to remove excess saline and bone debris, a 5 mm glass coverslip (specifications in Table 1) was carefully placed over the exposed brain region. Special care was taken to avoid trapping air bubbles beneath the coverslip, as these could interfere with imaging or cause pressure on the underlying tissue (Goldey et al., 2014). The coverslip was securely affixed to the skull using cyanoacrylate adhesive (see Table 1 for specifications), applied along the edges to ensure a stable attachment and create a sealed interface between the skull and coverslip (Mostany & Portera-Cailliau, 2008). To further reinforce the stability of the cranial window and to prevent any movement or potential gaps, dental cement was applied around the perimeter of the coverslip (Xu et al., 2007). This additional layer of dental cement not only stabilized the coverslip but also created a hermetic seal, effectively protecting the exposed brain tissue and ensuring the cranial window remained intact for long-term imaging. This procedure provided a stable and secure platform for long-term imaging through the cranial window, ensuring the integrity of the cortical region beneath the window throughout the experiment. To facilitate two-photon in vivo imaging of head-fixed animals, a custom-made headplate (see Table 1 for specifications) was positioned over the cranial window using an adjustable arm. The headplate was fixed securely to the skull to ensure minimal movement during imaging, which is critical for obtaining high-resolution images over time (Mostany & Portera-Cailliau, 2008; Holtmaat et al., 2009). This setup allowed precise alignment with the microscope and provided a robust environment for chronic imaging while preserving the health of the underlying brain tissue (Yang et al., 2010). To ensure proper adhesion, a layer of superbond (Table 1) was applied to the skull to enhance surface roughness. The headplate was then stabilized on top of the cranial window and secured in place using a dental cement mixture (powder mixing with solvent) (Table 1). After verifying the stability of the headplate, each animal was monitored until it fully recovered, following standard post-surgical care procedures as listed in 2.2.2.

2.3.7. Multiphoton imaging *in-vivo*

Two to four weeks after AAV transduction and transcranial window installation, multiphoton in vivo imaging was performed using a commercial microscope (Bergamo) built by Thorlabs (Newton, New Jersey, USA) equipped with Coherent Chameleon Ultra II (Coherent, Inc., Santa Clara, California, USA) laser systems. For the green-emitting fluorophore (920nm–960nm), the laser source was a Coherent Chameleon Ultra II pumped by a 10W Verdi (Coherent, Inc.) with an average output power of 1.3W–1.4W. For the red-emitting fluorophore, a monochromatic Coherent OBIS 561nm laser was used, providing an output power of 1.44W. mNeonGreen-LC3B and GRAB-NE were detected using photomultiplier tubes (PMTs) with a detection range of 500–550nm, while mRuby3-LC3B was detected with a PMT range of 570–

620nm. Prior to imaging, animals were handled and habituated to the setup for five days to reduce stress and ensure their comfort during the procedure. On the first day of imaging, the animals were anesthetized using isoflurane administered via inhalation by placing them in an isoflurane chamber for 30 seconds, after which they were transferred to a head-fixation apparatus positioned under the microscope objective. This procedure was implemented to minimize head movement and ensure the animals remained in a stable and comfortable physiological state throughout the imaging session. Imaging started with a 4X objective (Table 1) to verify the imaging area on the brain tissue. This was performed using one-photon (1P) excitation from an LED (X-CITE 200, 488nm) for illumination, and a fluorescent camera (1500M-GE, a 1.4 MP) to capture an overview image. Additionally, 1P excitation was used to adjust the focal plane for the region of interest. Subsequently, the 4X objective was replaced with a 40X water-immersion objective (Table 1) for *LC-NE* axonal two-photon imaging. The microscope settings were switched to two-photon (2P) mode using the Coherent Chameleon Ultra II laser for excitation at 920-960 nm. For imaging distal axons in the M1-PFC, a digital zoom of 10-13X was applied after identifying the axon of interest to include the maximum possible axon length within the field of view. Optical sectioning with a step size of 1 µm, defined as a Z-stack, was performed to acquire detailed images across the tissue depth. Imaging was conducted at an acquisition rate of 30 Hz, with 100-150 repeated Z-stacks collected at constant time intervals, depending on the size of the stack for each axon. To minimize movement artifacts, 15 frames per Z-plane were recorded making the acquisition time around 20-30 mins with spatial resolution of 2–3 µm for axonal thickness and an average length of 10–20 µm. All data, along with the corresponding metadata for each stack, were automatically saved in a designated folder for further analysis.

2.3.8. Combined two-photon imaging and Chemogenetic neuronal silencing of *LC*

For combined two-photon imaging and Chemogenetic neuronal silencing of *LC*, two types of AAVs – AAV-EF1a-DIO-mNeonGreen-tagged LC3B and Designer Receptor Exclusively Activated by Designer Drugs (DREADDs) AAV-EF1a-DIO-hM4D(Gi)-mCherry (Armbruster et al., 2007) – were injected into the *LC-NE* of B6.CgDbhtm3.2(cre)Pjen/J Dbh *cre* knock-in mice, followed by the installation of a transcranial window and a head-plate, as described above. Subsequently, an axonal stretch was imaged twice, before and after the injection of the DREADD receptor agonist JHU37160 (Bonaventura et al., 2019) to assess the effect of inhibition of the *LC*. The JHU37160 compound (Table 3) was injected subcutaneously at a dose of (0.5mg/kg) immediately after the first imaging session as indicated in the timeline of the experiment represented in *Fig. 17*. After a 20–30-minute post-injection period, during which the agonist had sufficient time to cross the BBB (Lawson et al. 2024), the exact same axonal stretch was imaged again. This allowed for a direct comparison of the LC3B -positive vesicle trafficking in conditions of basal neuronal activity with conditions involved *LC-NE* inhibition. Images were aquired as described above employing the Coherent laser for two-photon excitation and a 40X water-immersion objective. The Z-stack imaging was performed with a 1 μm step size, 10-13X digital zoom, and 30Hz acquisition rate, capturing 100-150 repeated Z-stacks with 15 frames per Z-plane to minimize movement artifacts.

Data from both imaging sessions, along with metadata, were automatically saved in a designated folder, following the constant procedures for data storage and organization. This ensured consistency and facilitated later comparison and analysis of the effects of hM4D(Gi)-induced inhibition on the neuronal activity in the locus coeruleus.

2.3.9. Optical fiber mediated photoconversion of mEos4-LC3B at the *LC-NE* axons projecting to the *PFC*

Distal *LC-NE* axons may lack the ability to degrade their cargo locally, requiring autophagic cargos to be transported to the neuronal soma of the *LC-NE* for cargo disposal. Addressing the question whether LC3B-positive organelles from distal axons projecting to the PFC retrogradely transported into the *LC-NE* somata, we specifically labelled autophagic vesicles in *LC-NE* axons with LC3B fused to photoconvertible fluorescent protein mEOS4 by the AAV injection into the *LC-NE* (AAV-EF1a-DIO-mEOS4-LC3B). Following the virus injection, an optical fiber implantation surgery was performed to enable photoconversion in the *mPFC*. Briefly, an optical fiber, manufactured from ceramic ferrule Table 1), was unilaterally and vertically introduced into the *PFC* (AP-1.8 mm, ML-0.3 mm and DV-2.5 mm) at a rate of 1μm/min. The fiber cannula was securely fixed in the skull using multiple layers of dental cement. Four to six weeks post-surgery, the fiber optic was connected to a 405 nm laser (5mw output power) via an optical fiber cord (300um diameter and 85% effectiency), which was configured to allow the animal to move freely within its familiar environment (homecage). The photoconversion procedure of the mEOS4 fluorescent protein was achieved using the 405 nm laser wavelength, set to an intensity of 5 mW. The photoconversion was administered in 600-second sessions in awake animals, with each session consisting of 1-second pulses separated by 10-second intervals. The timeline of the experiment is indicated in *Fig. 24*. Six hours following the photoconversion, the animals were anesthetized for brain collection as an aend point for the experiment and perfused with a fixative solution (4% PFA in PBS) to preserve the brain tissue. Brains, both those subjected to photoconversion at the *PFC* and those without photoconversion, were dissected and postfixed, and subsequently sliced. Special attention was given to conducting all dissections without exposure to daylight to minimize stochastic photoconversion. Sections of the *LC*, with a thickness of 40-45 micrometers, were collected in a 48-well plate containing 1x PBS and then processed for immunohistochemistry (ICH). Confocal microscopy was employed to image the photoconverted LC3B puncta at the *LC-NE* somata.

The photoconversion experiment aimed to assess the effect of environmental context, resulting in different *LC-NE* activity states (J. McCall et al., 2017), on LC3B -labeled autophagic vesicles delivery time to the *LC-NE* somata, dealt with photoconversion at the Familiar enviroment, where animals were housed in their home cages throughout the photoconversion period, and the Novel Arena, where animals were placed in a novel 40x40x40 cm box with white walls designed to be unfamiliar and potentially stress-inducing enviroment. For the photoconversion process, animals in both groups were exposed to a 405 nm laser with a power output of 5 mW, delivering illumination in 600-second sessions consisting of 1-second pulses with 10-second intervals between pulses. Six hours after the photoconversion, animals were euthanized and perfused with a fixative solution to preserve the brain tissue for subsequent histological analysis. Throughout the photoconversion procedure, all animals were filmed to document their behavior and assess how the environmental context influenced their activity and exploration. This filming was crucial for correlating observed behavioral changes with the photoconversion results, allowing for a comprehensive analysis of how environmental factors affect the efficacy of autophagic vesicle trafficking and related behavioral responses.

2.3.10. HEK 293T cells and transfection

HEK293T cells were maintained in DMEM supplemented with L-Glutamine and serum (DMEM+) in a Heraeus incubator (37°C, 5% CO2, 95% humidity). Cells were cultured in T-75 flasks until reaching 50-60% confluence, then transfected using the calcium phosphate method. For transfection, DNA was combined with Solution A followed by Solution B (detailed in paragraph 2.1.3, Table 2). After a brief 1-minute incubation at room temperature, this mixture was immediately applied to the cells. The culture medium was replaced with fresh DMEM+ after 3.5-4 hours of incubation.

2.3.11. Immunocytochemistry & Immunohistochemistry

For Immunocytochemistry (ICC), Cells were fixed with 4% paraformaldehyde (PFA) containing 4% sucrose for 10 minutes. After fixation, cells were washed with PBS to remove PFA and permeabilized with 0.2% Triton X-100 in PBS for 10 minutes. Following permeabilization, the cells were washed three times for 5 minutes each in PBS, then incubated for 1 hour in blocking buffer (2% BSA, 2% glycine, 0.5% gelatin, and 50 mM NH_4Cl in PBS) to reduce non-specific binding. Primary antibodies were applied in blocking buffer and incubated overnight at 4°C in a humidity chamber. The next day, coverslips were washed three times for 10 minutes each with PBS before incubating with secondary antibodies in blocking solution for 1 hour at room temperature. After three additional washes in PBS, cells were optionally stained with DAPI (1:1000 in PBS) for 10 minutes to visualize nuclei. Coverslips were mounted using Mowiol 4-88 (Merck Chemicals GmbH) and stored for imaging.

For Immunohistochemistry (IHC), Animals were perfused transcardially with PBS followed by 4% PFA. Extracted brains were post-fixed in 4% PFA for at least 8 hours and then cryoprotected by immersion in 30% sucrose for 48-72 hours. Brain sections (40 µm) were prepared using a freezing microtome (Microm HM440E, Microm). Slices were washed in PBS and permeabilized with 0.2% Triton X-100 in PBS for 1 hour. After washing, slices were blocked in 10% normal horse serum in PBS for 1 hour to reduce non-specific binding. Primary antibodies were incubated overnight at 4°C in blocking buffer. Following this, sections were washed three times for 10 minutes each in PBS, then incubated with fluorophore-conjugated secondary antibodies for 1 hour at room temperature. For nuclear counterstaining, sections were incubated with DAPI (1:500) for 10 minutes. After a final series of PBS washes and a brief rinse with distilled water, slices were mounted using Mowiol 4-88 (Merck Chemicals GmbH). The mounted sections were imaged with a fluorescence or confocal microscope.

2.3.12. Microscopy imaging of fixed and living cells/tissue

Confocal images of fixed cell cultures and tissue samples were taken using an SP8 or SP5 Confocal Laser Scanning Microscope (CLSM) (Leica Microsystems, Mannheim, Germany). For imaging of *LC-NE* neurons and their terminals in the PFC, a 63x/1.4 NA oil-immersion objective (HCX PL APO, Leica) was used. Images were acquired at 400-600 Hz, with a lateral resolution of 1024x1024 pixels and a Z-stack step size of 160 nm.

2.4. Analysis

2.4.1. Analysis of vesicles quantification

Image processing and analysis utilizes ImageJ-FIJI software, implementing a sophisticated multi-step workflow optimized for vesicle quantification. Initial pre-processing employs sequential digital filters: a rolling ball algorithm for background subtraction (radius optimized based on feature size), followed by median filtering (typically 2-3 pixel radius) and Gaussian smoothing (σ = 1-2 pixels) to reduce noise while preserving biological structures and improving signal-to-noise ratio (SNR) (Schindelin et al., 2012; Berg et al., 2019). Contrast enhancement utilizes histogram-based methods with precise documentation of parameters to maintain data integrity, as validated through extensive control experiments (Aaron & Chew, 2021).

Region of Interest (ROI) selection follows standardized anatomical criteria, incorporating both morphological features and fluorescence intensity profiles to ensure consistent cell soma delineation. Advanced automated ROI detection algorithms, supplemented by manual verification, ensure reproducible selection across experimental conditions. Multi-channel analysis isolates specific vesicle populations through channel splitting and colocalization analysis, with Max-Entropy thresholding applied using machine learning-optimized parameters to accurately segment vesicles throughout the complete Z-stack volume (Arganda-Carreras et al., 2017; Wiesmann et al., 2020).

The StarDist deep learning-based object detection algorithm, trained on manually annotated vesicle datasets, enables precise quantification of vesicle numbers and morphological parameters. This approach significantly improves detection accuracy compared to conventional threshold-based methods, particularly in cases of overlapping objects (Schmidt et al., 2018; Weigert et al., 2020). The algorithm employs a U-Net architecture with star-convex polygon representation, achieving superior performance in separating closely packed vesicles while maintaining morphological integrity (Völker et al., 2020; Fazeli et al., 2021).

Quality control includes comprehensive validation steps: thresholded images are merged with pre-processed data for visual verification, and automated circularity measurements ($4\pi \times \text{area}/\text{perimeter}^2$) assess vesicle morphology. The analysis pipeline generates multidimensional datasets including vesicle counts per ROI, size distributions (in μm^2), and shape parameters, with statistical measures of variance and confidence intervals. This standardized workflow ensures reproducible quantification while maintaining high sensitivity and specificity in vesicle detection and characterization.

2.4.2. *In-vivo* two-photon imaging analysis of mNeonGreen-LC3B vesicular trafficking

Analysis of autophagosomal dynamics in axons through time-series imaging requires sophisticated processing and analytical approaches to maintain both spatial and temporal accuracy. The analysis pipeline begins with advanced motion correction implemented through ImageJ-FIJI, utilizing the FAST4DREG plugin which incorporates the NanoJ-Core algorithm for sub-pixel accuracy registration across all dimensions (x, y, z, t) (Laine et al., 2019; Culley et al., 2018). This correction is essential for reliable tracking of small, rapidly moving vesicles in living tissue, with motion correction parameters optimized for each dataset using an iterative approach to maximize registration accuracy while minimizing potential artifacts.

A multi-step noise reduction protocol follows to optimize signal-to-noise ratio while preserving biological dynamics. This protocol implements rolling ball background subtraction with a 50-pixel diameter to remove large-scale intensity variations, followed by Gaussian filtering ($\sigma = 2$ pixels) for high-frequency noise reduction (Schindelin et al., 2019; Berg et al., 2020). These parameters are carefully optimized through empirical testing to maintain vesicle edge definition while reducing background fluctuations. Maximum intensity projection of z-planes generates high-contrast 2D representations of vesicular movement, enabling reliable tracking across time.

Vesicular tracking employs the TrackMate algorithm, enhanced with machine learning-based detection coupled with Linear Assignment Problem (LAP) trackers (Tinevez et al., 2017; Simon Youssef, et al. 2011). The approach incorporates multiple parameters for optimal vesicle detection and linking, including spot detection using Laplacian of Gaussian filtering, feature extraction covering intensity, size, and contrast, and track linking with gap closing and split/merge handling. Validation studies comparing automated tracking results with manual analysis demonstrate high correlation ($r > 0.90$) for key movement parameters, confirming the reliability of the automated approach (Nicolas Chenouard et al., 2014; Yichen Wu et al., 2019).

Quantitative analysis of vesicular dynamics utilizes custom Python scripts in the Spyder integrated development environment. The analysis pipeline extracts multiple movement parameters, including instantaneous and mean velocities (μm/s), maximum speed and acceleration profiles, total displacement and path length, directional persistence ratios, and pause frequency and duration. These comprehensive measurements enable detailed characterization of vesicular trafficking patterns under various experimental conditions. For chemogenetic manipulation experiments involving hM4D(Gi) receptor activation, the analysis pipeline is applied to matched pre- and post-J60 compound administration datasets, enabling direct comparison of trafficking parameters within the same axons before and after *LC-NE* neuron inhibition. Statistical analysis employs paired t-tests implemented in GraphPad Prism software, with careful attention to assumptions of normality and equal variance. Power analysis ensures adequate sample sizes for detecting biologically relevant changes in vesicular dynamic.

Quality control measures are implemented throughout the analysis pipeline, including semi-automated detection and removal of out-of-focus frames, drift correction validation through stationary landmark tracking, signal-to-noise ratio monitoring across time series, and cross-validation of tracking accuracy through manual spot checking. This comprehensive methodology enables detailed characterization of autophagosomal trafficking dynamics in living axons while maintaining rigorous standards for data quality and reproducibility. The integration of multiple analytical approaches provides robust quantification of trafficking parameters, allowing for detailed investigation of how *LC-NE* neuron activity influences autophagosomal transport.

2.4.3. *In-vivo* two-photon GRABNE2h signal analysis with mRuby3-LC3B trafficking

The analysis of vesicular trafficking and norepinephrine dynamics requires sophisticated image processing and analytical approaches to ensure accurate quantification while maintaining biological relevance. Initial preprocessing employs a multi-step protocol implemented through ImageJ-FIJI and Jupyter Lab, incorporating the NoRMCorre algorithm for motion correction with sub-pixel accuracy (Zhou et al., 2020). This correction step is crucial for maintaining spatial precision in subsequent analyses, particularly for tracking small, rapidly moving vesicles. Noise reduction utilizes a combination of wavelet-based denoising and adaptive thresholding techniques, optimized specifically for neural imaging applications to preserve biological signal dynamics while reducing background fluctuations (Giovannucci et al., 2019).

Vesicular tracking implements the TrackMate algorithm, enhanced with machine learning-based detection coupled with Linear Assignment Problem (LAP) trackers (Tinevez et al., 2017). This semi-automated approach allows for precise quantification of multiple movement parameters, including instantaneous and mean velocities, displacement vectors, directional persistence, and pause characteristics. The tracking accuracy is validated through comparison with manual tracking in subset analyses, ensuring reliability of the automated measurements (Chenouard et al., 2014). This comprehensive tracking approach enables detailed analysis of vesicular behavior across different experimental conditions while maintaining consistent measurement criteria.

The analysis of norepinephrine signaling through GRABNE2h fluorescence employs specialized ROI selection algorithms that incorporate morphological filters and automated bouton detection (Feng et al., 2019). Signal processing includes multiple steps to ensure accuracy: adaptive baseline correction using 8th percentile F0 calculation, photobleaching compensation through exponential fitting, and movement artifact correction using cross-correlation analysis. These processing steps are essential for maintaining signal fidelity and enabling precise temporal analysis of neurotransmitter dynamics (Patriarchi et al., 2020).

Feature extraction and trigger analysis utilize custom-developed Python algorithms that implement hierarchical clustering for stop point identification and wavelet transform analysis for directional changes. This approach enables detailed characterization of movement patterns and their correlation with norepinephrine release events. The analysis pipeline incorporates machine learning classification of movement patterns and statistical validation through bootstrapping methods, ensuring robust identification of biological events (Pachitariu et al., 2018). Data visualization and statistical analysis employ multiple approaches to ensure comprehensive understanding of the results. These include Z-score normalization across experimental conditions, hierarchical clustering of temporal patterns, and generation of event-triggered averages. Statistical inference utilizes mixed-effects models to account for both fixed and random effects in the experimental design (Saxena et al., 2019). This multi-faceted analytical approach enables detection of both broad patterns and subtle variations in vesicular trafficking and neurotransmitter release.

2.4.4. Statistical analysis

For statistical analysis I used GraphPad Prism 8 (GraphPad Software). Error bars indicate SEM and sample numbers are either indicated in the graph or below the figure. Data distributions were checked for normality and adequate statistical tests were used.

3. Results

3.1. Establishing *Locus coeruleus* – specific labelling of autophagic vesicles *in vivo*

Regulation of autophagy in distal axons of the *Locus coeruleus in vivo* has not been previously addressed. Therefore, I first aimed to establish an *LC*-specific labeling approach for autophagic vesicles *in vivo*. To label *LC-NE* neurons and identify their distal projections in the PFC, I employed a mouse model with a Cre recombinase knock-in specific to DbH-expressing neurons (B6.Cg-Dbhm3.2(Cre)Pjen/J, *Fig. 11A* (Liu et al., 2008). This mouse model is suitable for the selective targeting of neurons expresssing dopamine-β-hydroxylase (DbH), the enzyme responsible for catalyzing the conversion of dopamine to norepinephrine. *LC*-specific labeling, therefore, was achived through the injection of *LC*-targeted viral particles, utilizing CRE-driven viral recombination. Specifically, the AAV vector system employed in this study incorporated a double-floxed inverse orientation (DIO) element, ensuring that only neurons transduced with AAV-DIO and expressing Cre recombinase could express the desired marker fused to fluorescent tag (*Fig. 11B*). This combination of Cre-mediated recombination and the DIO viral system provides high specificity for *LC-NE* neurons, minimizing off-target viral expression in other brain regions (Schwarz & Luo, 2015).

3.1.1. Generation of the viral tools for labelling of autophagic vesicles *in vivo*

Microtubule-associated protein 1A/1B-light chain 3 (LC3) is a well-characterized protein involved in the autophagy pathway (Tanida et al., 2008; Mizushima et al., 2008). Briefly, upon the induction of autophagy, the cytosolic form of LC3 (LC3-I) undergoes conjugation with phosphatidylethanolamine to form the LC3-phosphatidylethanolamine conjugate (LC3-II), which is subsequently recruited to autophagosomal membranes (*Fig. 3*). This ability of associating with autophagic membranes has made LC3 a widely used marker for tracking autophagic vesicles in live-cell imaging studies (Fu et al. 2022).

Therefore, with the guidance of my supervisor, Anna Karpova, I generated several constructs for labelling autophagic vesicles *in vivo* in *LC-NE* neurons employing: 1) the AAV-DIO viral vector system, 2) the LC3B autophagic vesicle marker, and 3) various fluorescent proteins (FPs) including mNeonGreen (i), mEOS4 (ii) and mRuby3 (iii) as N-terminal fusion tags for distinct applications.

Specifically, mNeonGreen, characterized by its enhanced quantum yield and extinction coefficient, making it up to three times brighter than the most commonly used GFP derivatives (Shaner NC, Nat Methods. 2013), is ideally suited for *in vivo* imaging in brain tissue (Zhang et al., 2012; Chen et al., 2013). Therefore, I considered it well-suited for visualizing LC3B puncta within distal *LC-NE* projections during two-photon imaging through a transcranial window in the PFC (*Fig. 11 Bi*).

mEOS, a bright and photostable photoconvertible fluorescent protein (McKinney et al., 2009), allows for photoconversion from green to red emmision upon exposure to UV light (405 nm), making it a valuble tool for tracking the origin and final destination of a protein of interest in the context of its long-distance traffiking in living cells (Karpova et al., 2013; Dinamarca et al., 2016; Kravchick et al., 2016). Therefore, I designed mEOS4-LC3B as an N-terminal fusion construct to track redistribution of photoconverted autophagic vesicles from the distal axons projecting to the PFC back to the *LC-NE* somata in awake animals (*Fig. 11 Bii*).

Finally, mRuby3, a red fluorescent protein with enhanced brightness and photostability designed for live-cell imaging (Bajar et al., 2016), was utilized as a fusion with LC3B to detect autophagic vesicles trafficking through transcranial window in conjunction with fluorescent geneticly encoded neurotransmetor sensors, specifically GRABNE2h, for sensing norepinephrine release at distal axons of *LC-NE* neurons projecting to the PFC (Feng et al., 2021; Feng et al., 2024).

Collectively, for the subcloniong of an autophagy marker labeled with a defined flouresent protein (FP), I designed an insert containing FP-LC3B flanked by NheI and SgsI restriction sites, which was synthesized as a gBlock by IDT (Israel). This insert was then ligated into the AAV-EF1a-DIO vector (Addgene #50462), followed by in-house production of purified AAV particles.

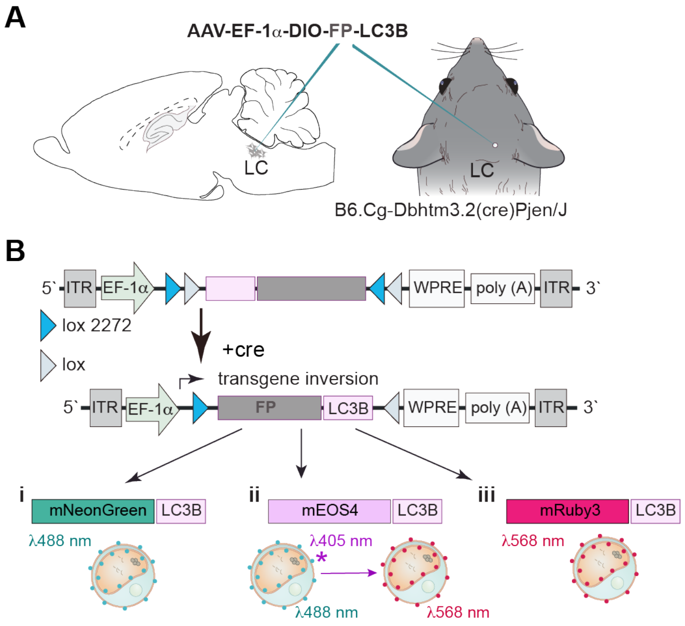

Figure 11| Cell type-specific in vivo labelling of autophagic vesicles for diverse applications

(A). Schematic representation of AAV9-DIO-EF1a-FP-LC3B injections into the LC-NE of DbH-Cre transgenic mice, which express Cre-recombinase under DbH intrinsic promoter. This initiate serial recombination steps and ultimately resulting in the active orientation of the transgene (Leslie O Goodwin, et al., 2019). (B) Scheme representing the double-floxed inverse orientation construct (AAV9-EF1a-DIO-FP-LC3B) for Cre-driven viral recombination and expression in LC-NE neurons of DbH-Cre transgenic mice. Key elements of the construct are indicated: inverted terminal repeats (ITR), the EF1α promoter, a FP-LC3B fusion protein flanked by pairs of LoxP and Lox2722 sites, a woodchuck hepatitis virus post-transcriptional regulatory element (WPRE), and a human growth hormone polyadenylation signal (hGH polyA). Illustration uses graphic elements courtesy of A. Karpova, used with permission.

3.1.2. Characterization of viral tools for their expression and suitability in labelling vesicles in the autophagy pathway *in vivo*

To characterize the cell type-specific expression and labeling of autophagic vesicles in *LC-NE* neurons, I first injected animal with the newly designed AAV constructs (*Fig. 11, B*), following the protocol described in the Meterials and Methods.

I confirmed the successful expression of mNeonGreen-LC3B by examining the specificity of labeling through fluorescence localized exclusively in the *LC-NE* (*Fig. 12, A*). mNeonGreen-LC3B was expressed in both *LC-NE* somata (Fig. 12 A-C) and its axonal projections located in the PFC, making it sutable for imaging via the transcranial window two-photon imaging (*Fig. 12, D, E*). Given that the LC3B protein exists in two distinct forms - the cytosolic form (LC3-I) and the conjugated form with phosphatidylethanolamine, known as the LC3-phosphatidylethanolamine conjugate

(LC3-II), which is subsequently recruited to autophagosomal membranes - the expression of the mNeonGreen fluorescent protein effectively mirrored these distinct forms. mNeonGreen fluorescence was observed both as a diffused cytosolic form filling the entire cell and as distinct puncta, representing LC3-I and the LC3-phosphatidylethanolamine conjugate respectively (*Fig. 12, C*). The later structures were detectable in both the *LC-NE* somata and distal axonal projections extending through the *PFC* (*Fig. 12, D, E*).

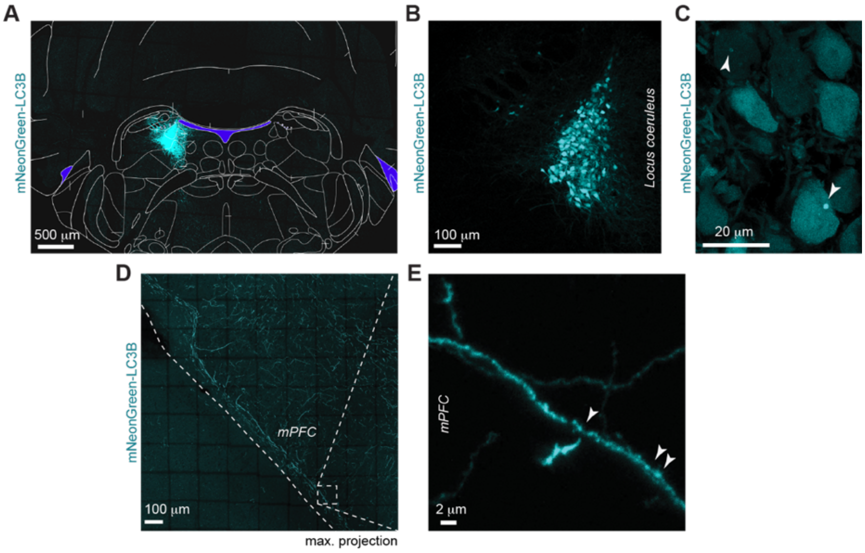

Figure 12| Expression of AAV-EF1a-DIO-mNeonGreen-LC3B in LC-NE somata and LC-NE distal LC-NE projections in the PFC

(A-C) The majority of LC-NE neurons exhibited robust expression of mNeonGreen. (D-E) Confocal tile-scanned image showing fluorescently labeled LC-NE axonal terminals in the mPFC, with dense axonal labeling observed, particularly in layers 1 and 2. E Magnified image from D showing LC3B fluorescent puncta in distal LC-NE axons (arrows), indicating the association of the marker protein with the membranous compartment.

Similar results were obtained from sections expressing mEOS4-LC3B in *LC-NE* neurons, which were subsequently stained with anti-TH antibodies. In the absence of photoconversion, negligible “red” fluorescence was observed within the *LC-NE* (*Fig. 13A*). High-magnification images from a single optical plane revealed somatic and axonal puncta of LC3B, indicative of autophagic vesicle labeling (*Fig. 13 B, C*).

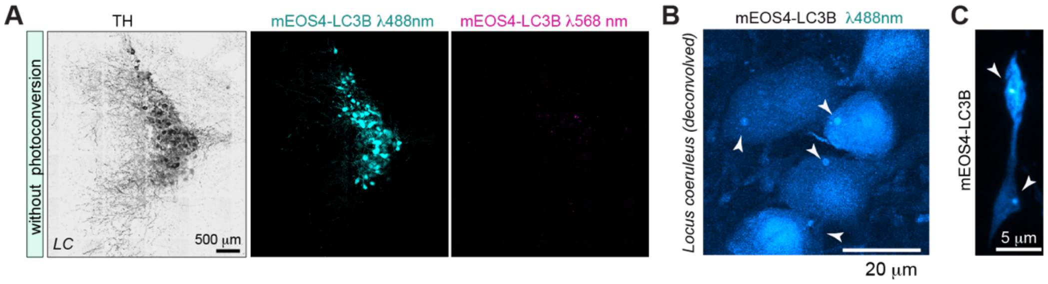

***Figure 13**| Expression of AAV-EF1a-DIO-mEOS4-LC3B in LC-NE somata and LC-NE axons*

(A) Confocal tile-scanned image showing anti-TH labeling within LC-NE neurons, with substantial AAV transduction observed in multiple neurons. Magnified images from a population of neighboring neurons in the LC-NE displaying mEOS4-LC3B expression in the neuronal somata (B) and in LC-NE axons (C). Arrowheads indicate the LC3-phosphatidylethanolamine conjugates, which detect AVs.

Finally, following the injection of the AAV expressing mRuby3-LC3B, numerous neurons within the *LC-NE* were labelled, confirming the efficiency of viral transduction and the effectiveness of the newly generated probe for detecting LC3B -positive vesicles in *LC-NE* projections (arrowheads in *Fig. 14 C*).

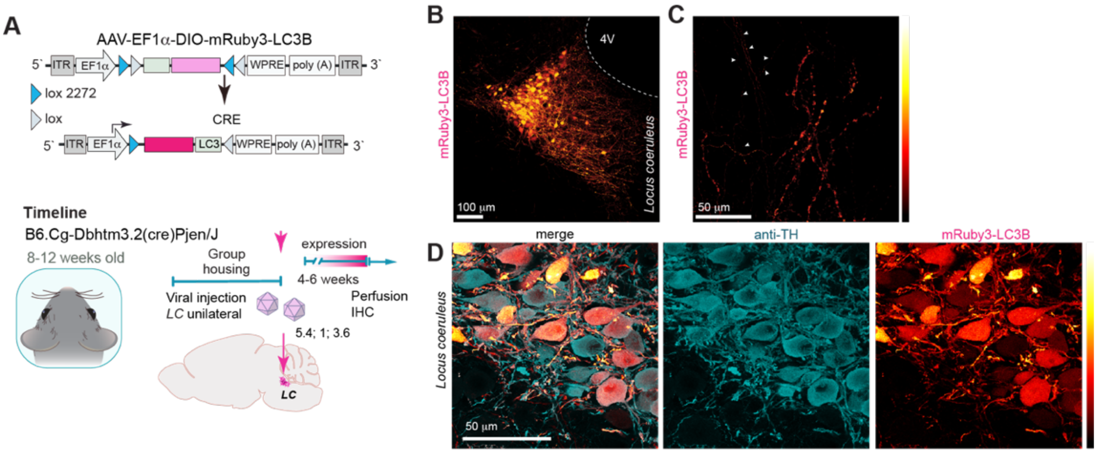

***Figure 14**| Expression of AAV-EF1a-DIO-mRuby3-LC3B in the LC*

(A) Schematic representation of the DIO viral construct encoding LC3B fused to the mRuby3 FP, along with the experimental timeline, including the injection procedure in 8- to 12-week-old DbH-Cre mice for targeting LC-NE neurons. Viral injections were performed accordingly stereotactic coordinates (AP: -5.4 mm, ML: ±1 mm, DV: -3.6 mm). Four to six weeks post-injection, animals were perfused to assess viral transduction of LC-NE neurons. (B) Confocal overview image of AAV-transduced LC-NE neurons. (C) mRuby3-LC3B expression in LC-NE axons (arrowheads). (D) Magnified confocal image of LC-NE neurons labelled with anti-TH antibodies and expressing mRuby3-LC3B . Please note that the image in panel D was obtained using enhanced HyD settings to ensure the detection of mRuby3 in the majority of LC-NE somata, thereby confirming efficient expression levels for detection in distal axons. Graphic courtesy of some elements of A. Karpova, used with permission.

Thus, the conjunction of Cre-mediated recombination and the DIO viral system ensures high specificity for *LC-NE* neurons, minimizing off-target effects in other brain regions (Schwarz & Luo, 2015) and LC3B fused N-terminally to the fluorescent tag has proven to be suitable for labeling autophagic vesicles *in vivo*. Therefore, my results convincingly demonstrate that DbH-Cre animals virally transduced with AAV-EF1a-DIO-FP-LC3B specifically express the AV marker in *LC-NE* neurons, and that *LC-NE* axons projecting into the PFC can be efficiently detected. This provides a robust model for investigating the trafficking velocities and motility patterns of autophagic vesicles *in vivo* across distal *LC-NE* trajectories.

3. 2. LC3B-positive vesicles in *Locus coeruleus* projections to the PFC are dynamic *in vivo* and are characterized by distinct trafficking velocities and motility patterns

Maintenance of proteostasis depends on efficient endo-lysosomal and autophagy systems and is particularly important for survival of long-range projecting norepinephrinergic neurons of the *Locus coeruleus* (*LC-NE*). Understanding the regulation of neuronal autophagy in these most burden cells in the brain, including autophagosome navigation through distal axons, somatic cargo delivery and disposal could inform the development of intervention strategies to prevent *LC-NE* neurodegeneration. Surprisingly, the trafficking velocities and motility patterns of AVs in *LC-NE* axons *in vivo* have not been previously studied.

To monitor the navigation of autophagosomes *in vivo* in distal *LC-NE* axons projecting to the *PFC*, I injected AAV expressing mNeonGreen fused to autophagy marker and employed two-photon microscopy via the transcranial window implanted at the PFC (*Fig. 15 A*).

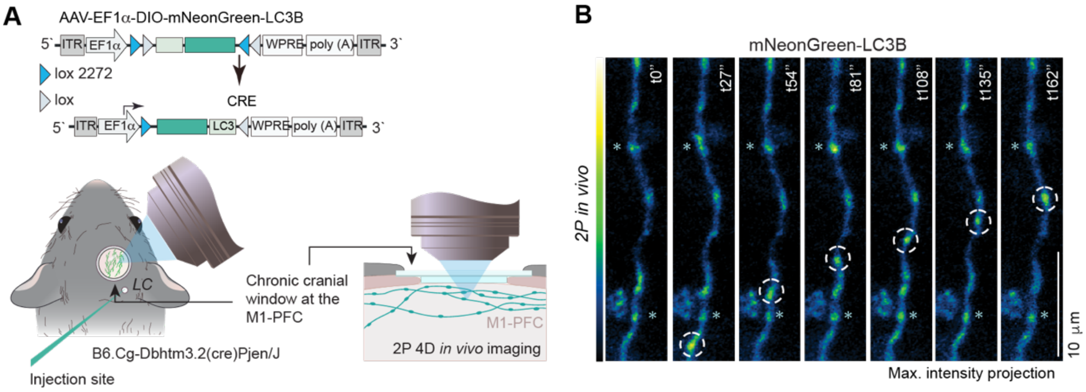

Figure 15| In vivo two-photon imaging of mNeonGreen-LC3B -labeled vesicles in LC-NE axons projecting to the PFC

(A) Schematic representation of the experimental setup, including AAV-EF1a-DIO-mNeonGreen-LC3B injection into DbH-Cre mice and transcranial window implantation to access LC-NE axons in the PFC/M1 region for two-photon imaging. (B) Example of in vivo two-photon imaging through the transcranial window in the PFC, showing labeled vesicles trafficking along the axons (dashed circles). Asterisks indicate mNeonGreen-LC3B puncta that remain immobile during time-lapse acquisition. Graphic courtesy of some elements in panel A of A. Karpova, used with permission.

Analysis of distal *LC-NE* axonal streatches recorded during the spontaneous activity of *LC-NE* neurons revealed a surprising heterogeneity in the trafficking velocities and motility patterns of LC3B -labeled vesicles *in vivo*. Semi-automated image processing facilitated the visualization of LC3B -positive vesicle trajectories within a defined time window and enabled the quantification of multiple key features of their trafficking characteristics (*Fig. 15 A*). These features included track length over time, which determines velocity, and the mean displacement ratio, which identifies vesicles that returned to their initial location within the imaging time window. Specifically, some LC3B -positive vesicles exhibited unidirectional movement with an average velocity of approximately 0.1 µm/s, while others displayed bidirectional movement, characterized by fluctuating average and maximum velocities (*Fig. 16 A, B*). Correlation plots between average velocities, maximum velocities, tracking duration, and displacement ratios (*Fig. 16 B-D*) highlight the overall heterogeneity of LC3B -positive vesicle dynamics across distal *LC-NE* axons during spontaneous *LC-NE* neuronal activity. Specifically, the strong positive correlation between average and maximum velocity during spontaneous *LC-NE* neuronal activity indicates that autophagic vesicles traverse the axon in a sustained manner, without instantaneous velocity fluctuations, within the imaged axonal segment. In other words, this indicate that fast moving vesicles along the imaged axonal segment *in vivo* have a lower likelihood of becoming immobile.

Its known that movement along microtubules occurs in a bidirectional, stop-and-go manner and is regulated by the alternating activities of a plus-end-directed kinesin motor and a minus-end-directed dynein-dynactin motor (Maday and Holzbaur, 2014; Maday et al., 2012; Maday and Holzbaur, 2016). The negative correlation between the displacement ratio, which characterizes the bidirectional trafficking pattern of LC3B + vesicles, and tracking time suggests a preferential vesicle directionality within the imaged axonal segment *in vivo*, as evidenced by shorter tracking durations. This preferential directionality likely reflects retrograde trafficking, given that LC3B$^+$ vesicles must reach the somatic region for cargo disposal. Concomitantly, longer tracking durations associate with changes in directionality, occurring in scenarios where trafficking velocity remains constant, but LC3B +vesicles reverse direction once or multiple times within the imaged axonal segment in vivo. At the molecular level, this suggests the regulation of alternating activity between the minus-end-directed dynein-dynactin motor and the plus-end-directed kinesin motor. The weak correlation between average velocity and displacement ratio suggests that vesicles moving at high speeds do not necessarily follow a linear, unidirectional path. This implies that, despite their fast velocities, LC3B$^+$ vesicles may still alter their directionality.

Given the observed discrepancies in trafficking behavior, I aimed to determine whether the variability in trafficking velocities and motility patterns delineates distinct subpopulations of autophagic vesicles in *LC-NE* axons *in vivo*. To achieve this, I performed principal component analysis (PCA) to assess the clustering of vesicle populations based on three key parameters: average velocity, maximum velocity, and displacement ratio. A feature extraction algorithm was then applied to classify the recorded events according to the dominant trafficking characteristics of LC3B$^+$ vesicles. This analysis identified three primary clusters of LC3B+ vesicles, each distinguished by unique trafficking characteristics: slow unidirectional, slow bidirectional, and fast bidirectional (*Fig. 16 E, F*).

Thus, these findings suggest that distal *LC-NE* axons projecting to the *PFC* accomodate mobile LC3B -positive vesicles, characterized by distinct trafficking velocities and motility patterns under conditions of spontaneous *LC-NE* neuronal activity. Considering the absence of conventional synaptic contacts at most norepinephrine-releasing boutons and their reliance on volume transmission (Atzori et al. 2016), this observation points to a presynaptic, autocrine mechanism regulating LC3B $^+$ vesicles trafficking in *LC-NE* axons.

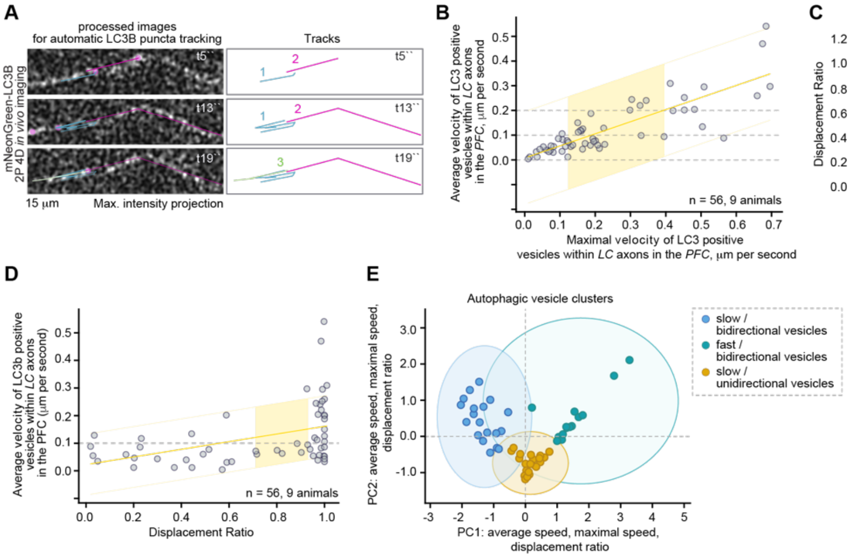

Figure 16| Analysis of trafficking velocities and motility patterns of LC3-positive vesicles in distal LC-NE axons during spontaneous LC-NE neuronal activity in vivo

(A) Semi-automated image processing of recorded distal LC-NE axons, showing three distinct tracks (1, 2, and 3) obtained over time, representing the different trafficking behaviors of LC3B -positive vesicles in vivo. (B). Linear correlation between the average and maximum velocities of LC3B -positive vesicle movement. It represents the distance traveled by each vesicle over time. (C) Correlation between the total track duration and the displacement ratio of LC3B -positive vesicles. (D) Correlation between the displacement ratio and average velocity, illustrating the heterogeneity of vesicle behavior. (E) Principal component analysis (PCA) based on three extracted features reveals three primary clusters of LC3B -positive vesicles, each characterized by distinct trafficking characteristics*: slow unidirectional, slow bidirectional, and fast bidirectional. (F) Cluster analysis further differentiates between uni- and bidirectional motility patterns, with an overall average vesicle velocity of approximately 0.1 µm/s. n=56 represents the number of distinct LC3-positive puncta obtained from multiple axons of 9 animals.*

3. 3. Chemogenetic silencing of *LC-NE* activity accelerates trafficking velocity and alters the directionality of AV trafficking in distal axons projecting to the *PFC in vivo*

Given the absence of conventional synaptic contacts at most norepinephrine terminals and their reliance on volume transmission (Atzori et al. 2016), variations in presynaptic adrenergic receptor activation suggest a presynaptic, autocrine mechanism for the regulation of autophagy in *LC-NE* axons. Propagation of neuronal activity across presynaptic boutons enhances norepinephrine release, preferentially activating high-affinity β2-AR signaling (Seungkirl Ahn et al., 2018). This activation engages Gs-protein coupling to stimulate PKA, initiating a cascade of subcellular events that culminate in prolonged dwelling time of LC3-containing vesicles, reflecting their immobilization (Cheng et al., 2015; Andres-Alonso et al., 2019). In contrast, activation of high-affinity α2-ARs, which are sensitive to low NE concentrations, signals through Gi-protein coupling to inhibit PKA activity, thereby potentially exerting an opposing effect. Furthermore, it remains an open question whether slow, bidirectional autophagic vesicles can transition to fast, unidirectional trafficking in response to changes in neuronal activity.

Previous studies in cultured hippocampal neurons have demonstrated that local cAMP/PKA activation significantly increases the dwell time of LC3B -positive amphisomes, a hybrid organelles on autophagy pathway, at synaptic boutons, while inhibition of PKA activity reduces dwell time and enhances the velocity of LC3B -positive vesicles during retrograde transport (Andres-Alonso et al., 2019; Andres-Alonso et al., 2021). These findings support the hypothesis that in distal *LC-NE* axons ptojecting into the *PFC*, the trafficking of LC3B + organelles may be regulated by autocrine mechanisms, involving the functional interplay between both β2-adrenergic and α2-adrenergic receptors.

Based on these assumptions, I hypothesize that activation of low-affinity α2-AR through *LC-NE* inactivation may facilitate vesicle trafficking along distal axonal projections without inducing immobilization, thereby accelerating the efficient delivery of autophagic vesicles to the *LC-NE* somata (*Fig. 10*).

Notably, variations in spontaneous activity among recorded *LC-NE* axons projecting to the *PFC* (*Fig. 16*) may account for the observed heterogeneity in the trafficking characteristics of AVs across different axons.

Therefore, I next asked whether blocking of *LC-NE* neuronal activity influences the trafficking velocities and motility patterns of autophagic vesicles in *LC-NE* axons *in vivo* or not.

To test this hypothesis, I employed a chemogenetic approach to modulate neuronal activity within the *LC-NE.* This approach involved the co-expression of mNeonGreen-LC3B, a marker for autophagosomes, and inhibitory Designer Receptor Exclusively Activated by Designer Drugs (DREADD), the engineered variant of the muscarinic acetylcholine receptor hM4D(Gi) (AAV-hSyn-DIO-hM4D(Gi)-mCherry) (McCall et al., 2015; Wagatsuma et al., 2018) and subsequent *in vivo* monitoring of LC3B+ dynamics was performed using two-photon imaging through a chronically implanted transcranial window (*Fig. 17*). Activation of hM4D(Gi) was achieved using the selective DREADD ligand JHU37160 (J60), which exhibits superior affinity and enhanced potency compared to earlier agonists (Bonaventura et al., 2019) and enabled precise, within-subject comparisons of LC3B+-vesicle trafficking velocities and motility patterns along the same distal axon, both prior to and following ligand administration.

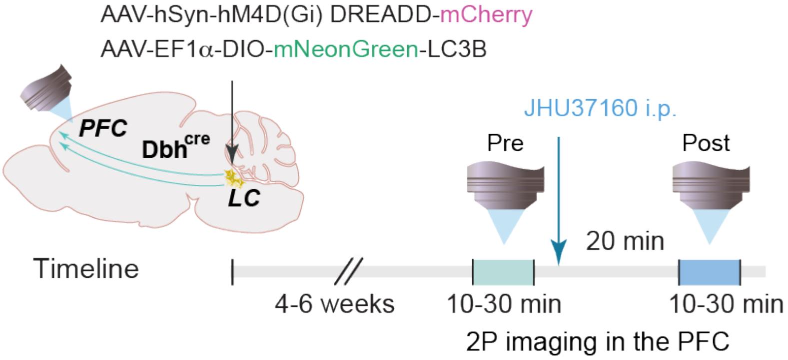

Figure 17| Graphical illustration depicting the experimental timeline for assessing LC3B -labeled vesicle trafficking velocities and motility patterns under systematic LC-NE silencing using hM4D(Gi)

The experimental workflow begins with the co-injection of AAV-hSyn-DIO-hM4D(Gi)-mCherry and AAV-EF1a-mNeonGreen-LC3B into the LC-NE region using stereotactic coordinates (AP: -5.4 mm, ML: ±1 mm, DV: -3.6 mm) and followed by transcranial window surgery over the PFC/M1 region to enable two-photon imaging. Four to six weeks post-surgery, 4D two-photon in vivo time-lapse imaging was conducted during spontaneous LC-NE activity to identify and designate LC-NE projections as regions of interest (ROIs). Subsequently, the animals were returned to their cages, and JHU37160 was administered subcutaneously to achieve effective LC-NE activity silencing via Gi-protein coupling mechanism. JHU37160 was selected for its higher affinity, greater potency, and reduced side-effect profile compared to clozapine N-oxide (CNO)(Bonaventura et al., 2019). Twenty minutes post-administration, to ensure peak activation ofhM4D(Gi)(Gi) and effective reduction of LC-NE activity, a new imaging session was conducted at the same ROIs using identical imaging settings.

Intriguingly, comparative analysis demonstrated that acute systemic hM4D(Gi) DREADD-mediated inhibition of *LC-NE* neurons induced substantial changes in the trafficking characteristics of LC3B + vesicles. Specifically, this intervention resulted in a marked increase in the average trafficking velocity shifting from a 0.09 µm/s (*Fig. 18*) during spontaneously active *LC-NE* to 0.15 µm/s under silenced *LC-NE* conditions (*Fig. 18, A-C*).

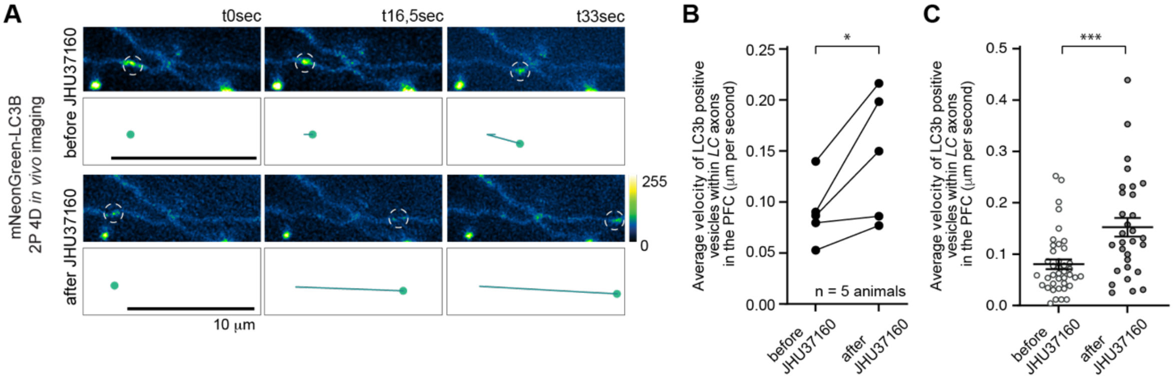

Figure 18|hM4D(Gi) DREADD-mediated inhibition of LC-NE neurons accelerates trafficking velocity of AV in distal axons projecting to the PFC in vivo
(A) Representative 2P 4D in vivo time frames acquired before and after the IP administration of JHU37160. Dashed circuits indicate automatically recognized changes in mNeonGreen intensities, defined as LC3B -positive clusters tracked over time. Traces were defined using an automatic plugin algorithm (TRACKMATE) with manual annotation in ImageJ. show the length of each vesicle track over time. (B, C) Averaged velocity of LC3B -positive vesicles recorded within LC-NE axons before and after LC-NE inhibition.

Previous findings indicate the presence of distinct subpopulations or clusters of LC3B + vesicles, distinguished by their multidimensional trafficking characteristics, including unique trafficking velocities and motility patterns observed under conditions of spontaneous *LC-NE* neuronal activity. Therefore, I next investigated whether hM4D(Gi) DREADD-mediated inhibition of *LC-NE* neurons could modulate these representative trafficking characteristics. Specifically, I analyzed whether *LC-NE* silencing alters LC3B+ vesicles trafficking parameters in a complex manner, encompassing changes in directionality pattern as well as modifications in trafficking velocity.

To address this, I conducted a cluster analysis comparing the same regions of interest (ROIs) before and after JHU37160 administration, focusing on displacement ratios and mean trafficking velocities of LC3B+ vesicles. Intriguingly, in spontaneously active *LC-NE* axons projecting to the *PFC*, AVs were similarly represented by unidirectional and bidirectional patterns (*Fig. 17 A; Fig. 19 A-D*). Remarkably, *LC-NE* silencing significantly reduced the proportion of bidirectional AVs at about 34%, resulting in a marked unification of directionality as evidenced by an increased number of unidirectional vesicles (*Fig. 19*). Subsequent principal component analysis revealed distinct shifts in the clustering patterns of LC3B+ vesicles, reflecting altered

multidimensional trafficking characteristics, including motility patterns and trafficking velocities, following JHU37160 administration.

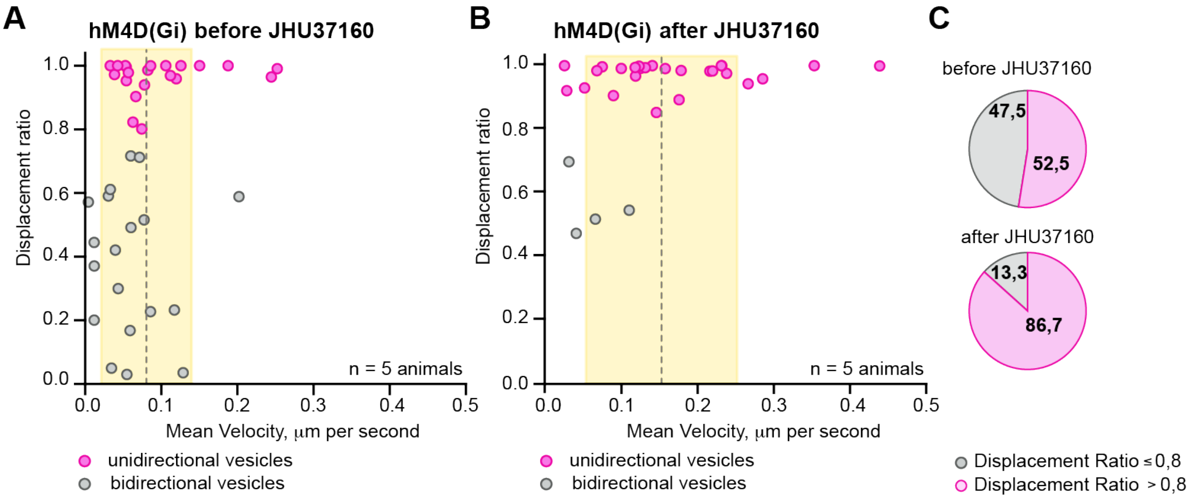

Figure 19|hM4D(Gi) DREADD-mediated inhibition of LC-NE neurons results in switch in directionality of AV trafficking in distal axons projecting to the PFC in vivo

The graphs illustrate the cluster analysis, where each point corresponds to a single track recorded before (A) and after (B) the acute administration of JHU37160 (J60). The grey dashed line represents the overall mean trafficking velocity, while the yellow-shaded area denotes the standard deviation of the average velocity. The shift in the grey dashed line from panel A to panel B reflects an increase in the average mean trafficking velocity of AVs. Furthermore, the distribution of mean trafficking velocities becomes broader following JHU37160 treatment (B). All events were clustered based on dominant directionality, with a displacement ratio threshold of 0.8. Magenta circles represent unidirectional AVs, whereas gray circles correspond to bidirectional vesicles. Panel C shows that following LC-NE silencing, the number of AVs exhibiting bidirectional trafficking motility decreased by approximately 34%. This reduction was accompanied by a notable increase in the number of AVs displaying unidirectional motility. (n number represent number of vesicles before and after treatment, collected from 5 animals per group).

The PCA showed a clear divergent distribution in directionaly parameter between systimaticly inhibited *LC-NE* neurons and control samples. Notably, three primary clusters - slow bidirectional, fast bidirectional, and slow unidirectional - observed during spontaneous *LC-NE* activity were no longer represented after *LC-NE* neuronal silencing. Instead, new clusters emerged, characterized as slow unidirectional, fast unidirectional, and extra-fast unidirectional autophagic vesicles (*Fig. 20, A, B, C*).

Altogether, these results suggest that *LC-NE* inacitation may **unify** LC3B + vesicles trafficking directionality by promoting a shift from bidirectional to unidirectional motility within *LC-NE* axons projecting to the *PFC in vivo*. This shift likely reflects an activity-regulated reconfiguration of cargo-molecular motor interactions, such as a switch between dynein- and kinesin-mediated transport.

Furthermore, *LC-NE* inactivation appears to enhance LC3B+ vesicles trafficking velocity *in vivo* and unification in directionality, likely by modulating both reduced immobilization and processivity of motor proteins.

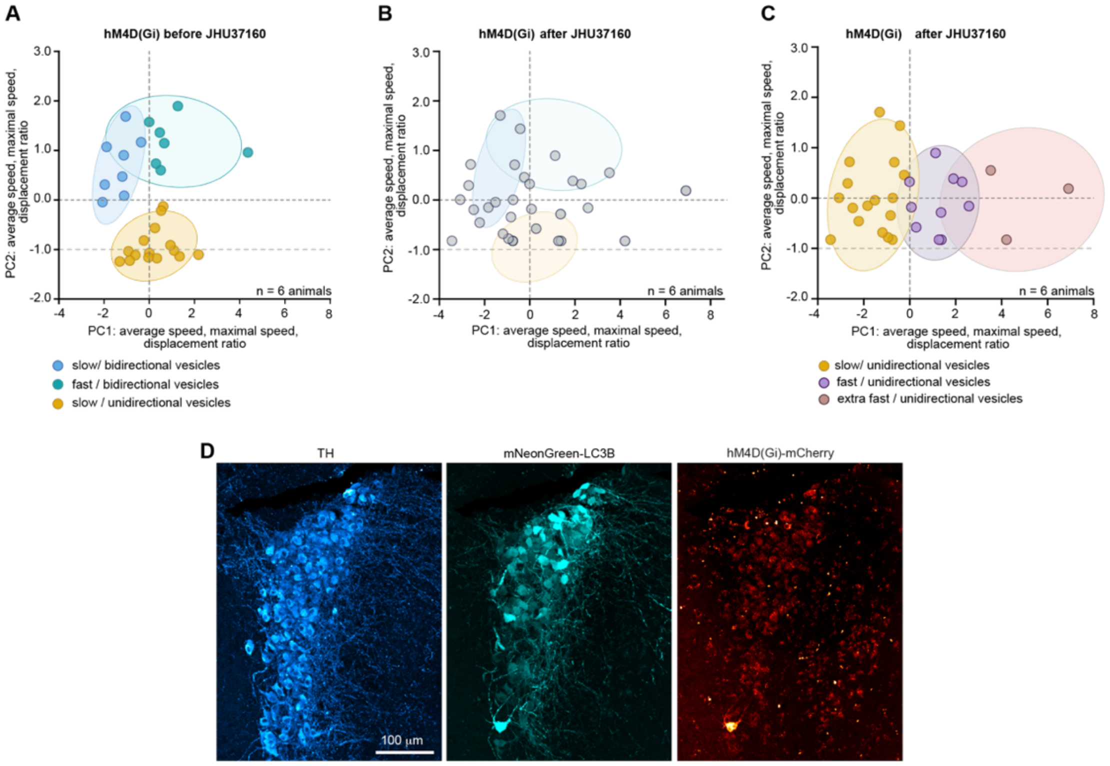

***Figure 20*|hM4D(Gi) DREADD-mediated inhibition of LC-NE neurons results in a switch in the cluster representations of LC3B -labeled AVs, reflecting changes in their complex multidimensional trafficking characteristics**

(A). PCA Scores Plot visualization of trafficking velocities and motility patterns prior to J60 administration. Three distinct clusters were observed: slow unidirectional (yellow), slow bidirectional (blue), and fast bidirectional (purple). Each cluster represents unique vesicle dynamics characterized by directionality and trafficking velocities. (B-C) Following LC-NE silencing with J60 administration, the three primary clusters—slow bidirectional, fast bidirectional, and slow unidirectional—observed during spontaneous LC-NE activity were no longer present. Instead, new clusters emerged, characterized as slow unidirectional, fast unidirectional, and extra-fast unidirectional AVs. Ellipses represent the spatial distribution of data points for each cluster, summarizing the variation within the cluster. Dashed lines indicate PCA axes for feature variance. In B, newly emerged patterns were overlaid with cluster areas before silencing for comparison. (D) Following data acquisition, immunostaining was performed on dissected brain slices to confirm infection rates in LC-NE neurons. Confocal tail.scan microscopy revealed that both mNeonGreen-LC3B and hM4D(Gi)-mCherry were co-expressed in TH-positive LC-NE neurons. Expression of hM4D(Gi) was not LC-, but neuron-specific (AAV-hSyn-hM4D(Gi)-mCherry.

3. 4. Distal *LC-NE* axons projecting to the *PFC* exhibit negligible lysosomal machinery for local autophagic cargo disposal, and AVs can travel retrogradely toward the *LC-NE* somata during spontaneous *LC-NE* activity

Whether the preferential unidirectional mobility of LC3B+ vesicles observed during *LC-NE* silencing specifically characterizes **retrograde**-directed trafficking remains unresolved.

To overcome this challenge, I thought first to investigate whether lysosomal machinery is present within the distal *LC-NE* axons projecting to the *PFC*. To explore whither lysosomes are sparse in distal *LC-NE* axons projecting to the PFC, I labeled *LC-NE* neurons with eGFP by injecting AAV-DIO-eGFP into *LC-NE* neurons of Cre recombinase expressing mice in DbH expressing neurons.

The number of LAMP2a-positive puncta, a lysosomal marker, was then assessed within the distal axons at the *PFC*. To enable a comparative analysis of LAMP2a puncta in axons versus lysosomes in the somatic regions of neurons and glia at the *PFC*, 3D reconstructions and volume rendering were performed, followed by isosurface masking based on GFP cell fill using Imaris (Bitplane). Further immunohistochemistry with anti-TH-specific antibodies confirmed the *LC-NE* origin of the virally transduced GFP projections.

Quantitative image analysis revealed that LAMP2a puncta were sporadically present in the distal *LC-NE* axons at the *PFC,* with their numbers being negligible compared to the surrounding cellular environment (*Fig. 21D*). This suggests that these axons may lack the capacity for local cargo degradation due to the limited presence of lysosomes. As a result, they rely on long-distance retrograde transport of AVs, mediated by the dynein molecular motor, to the neuronal soma for lysosomal fusion, autolysosome formation, and subsequent cargo degradation.

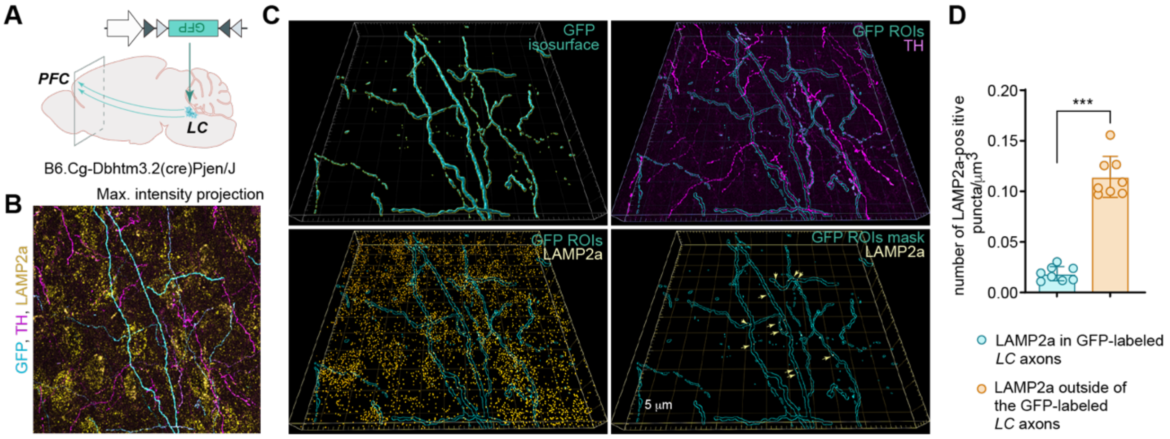

Figure 21| LAMP2a-positive lysosomes are sparsely distributed within the LC-NE axons projecting to the PFC

(A). Schematic representation of viral injection into the LC-NE using AAV-DIO-GFP for labeling LC-NE axonal projections. (B). Confocal maximum intensity projection of LC-NE axons in the PFC co-immunolabeled with anti-TH and anti-LAMP2a antibosies. (C). 3D reconstructed images generated using Imaris software (Bitplane). Top-left: 3D isosurface rendering of GFP-labeled LC-NE axonal projections, illustrating the dense LC-NE axonal network in the PFC.Top-right: Colocalization of GFP-labeled LC-NE axons (cyan) with TH immunoreactivity (magenta), confirming LC-NE specificity. Bottom-left: Colocalization of GFP-labeled LC-NE axons (cyan) with LAMP2a immunoreactivity (yellow). Bottom-right: LAMP2a immunoreactivity masked by GFP-defined ROIs (cyan) (D) Graph showing the quantification of LAMP2a-positive puncta within GFP-labeled LC-NE axons compared to LAMP2a-positive puncta outside GFP-labeled axons. Unpaired t-test. Box size: 5 µm.

Previous experiments suggest that unidirectional LC3B + vesicles exhibiting fast velocities are likely trafficking in the **retrograde** direction. Therefore, in the subsequent set of experiments, I investigated whether LC3B -labeled vesicles formed in the distal axons are capable of traversing the full distance from the *PFC* back to the *LC-NE* somata *in vivo*.

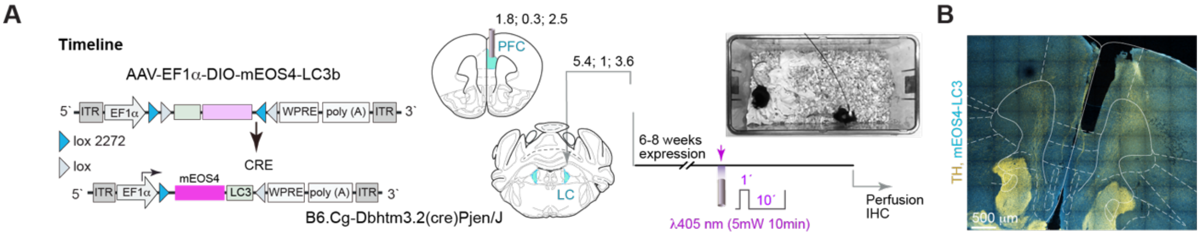

Figure 22| Experimental design for selective labeling of autophagic vesicles in distal LC-NE axons by mEOS4 photoconversion

(A) An experimental timeline illustrating the viral injection of the photoconvertible fluorophore mEOS4-LC3B into LC-NE neurons to label autophagic vesicles, alongside fiber implantation in the mPFC for subsequent photoconversion. The photoconversion protocol was executed 6–8 weeks post-surgery using a 405 nm laser with an output power at the fiber tip of approximately 5 mW. The optical fiber was connected to the 405 nm laser through a 1.5 m flexible fiber. To mitigate potential thermal damage to brain tissue, the stimulation protocol was designed to

avoid continuous radiation, adhering to recommendations by Schwarz and Luo (2015). (*B*) *Confocal tile-scanned image depicting the location of the fiber trace within the mPFC region.*

To label autophagic vesicles and assess their redistribution, I utilized the photoconvertible fluorophore mEOS4, N-terminally fused to LC3B (*Fig. 11 Bii).* Following the validation of AAV-DIO-mEOS4-LC3B , a 300 μm diameter optical fiber was implanted into the mPFC (*Fig. 22 A, B*), as previously described (Yizhar et al., 2011). This experimental configuration allowed for the photoconversion of mEOS4-LC3B -labeled vesicles in distal *LC-NE* axons within the *mPFC*, enabling the subsequent detection of photoconverted puncta at the *LC-NE* following brain sectioning.

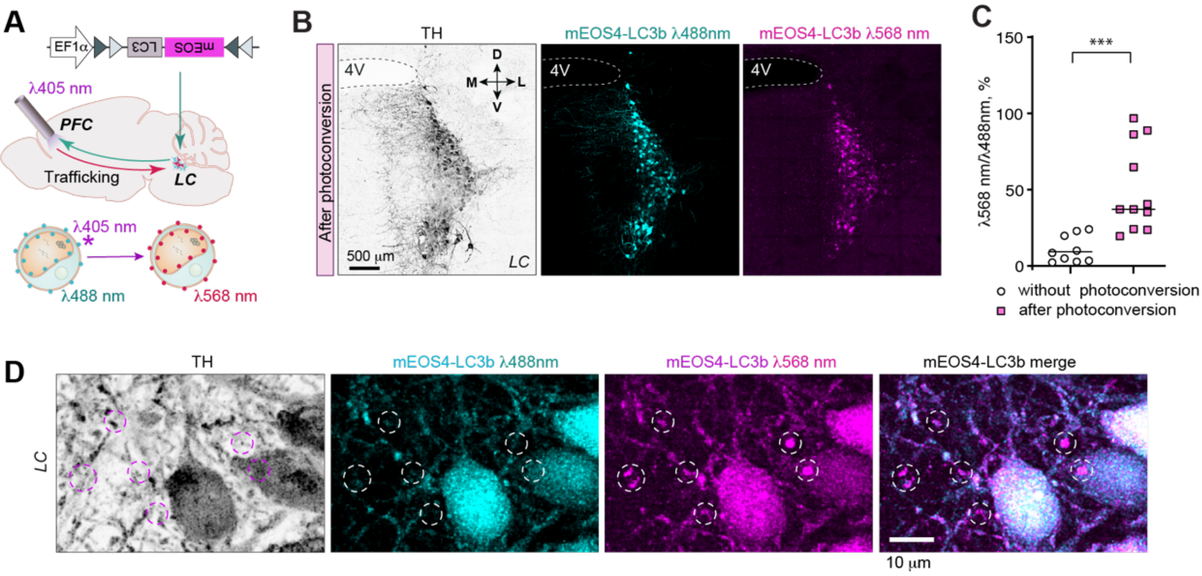

Figure 23| LC3B -positive AVs are capable of retrograde transport along axons projecting to the PFC, traveling toward the LC-NE somata during spontaneous LC-NE activity

(A) Schematic representation of the experimental procedure. (*B*) *Confocal tile-scan depicting photoconverted mEOS4 fluorescence in the LC-NE following photoconversion at the PFC. Anti-TH immunostaining labels LC-NE neurons. Six hours post-photostimulation, animals were perfused, and LC-NE sections were immunostained for tyrosine hydroxylase. Two experimental conditions were compared: the "photoconverted", the group of animals which underwent a UV light stimulation protocol consisting of 1-second pulses at 10-second intervals for a total duration of 10 minutes (Yizhar et al., 2011), and a control group that underwent the same procedures without photostimulation.* (*C*) *Graph illustrating a significant increase in photoconverted versus non-photoconverted mEOS4 fluorescence, confirming the efficiency of photoconversion and the ability of photoconverted LC3B to reach neuronal somata. n denotes the number of animals; unpaired t-test.* (*D*) *Magnified confocal maximum projection image of LC-NE neurons post-photoconversion at the PFC, stained with anti-TH antibodies. Dashed ROIs highlight "red"-positive and "green"-negative puncta, indicating the PFC origin of LC3B -labeled vesicles. Note that the somatic region was imaged with overexposure to enhance detection of puncta in the neurites.*

Qualitative and quantitative analyses revealed significantly elevated levels of photoconverted "red" mEOS4 fluorescence in *LC-NE* neurons of animals subjected to UV light stimulation in the PFC, in contrast to non-stimulated controls, which showed negligible "red" fluorescence (*Fig. 11; Fig. 23 B, C*). Moreover, multiple photoconverted "red" puncta were observed in TH-positive neurites in close proximity to *LC-NE* somata, providing compelling evidence that distally photoconverted LC3B+ vesicles can indeed reach neuronal somata within the six-hour time frame. Although varying in total duration, largely depending on the length of the axons assessed, my findings align with previous observations in cultured neurons, further supporting the concept of long-distance retrograde organelle trafficking for somatic cargo delivery in *LC-NE* neurons *in vivo* (Mizushima et al., 2008; Nakatogawa et al., 2009).

3. 5. Heightened *LC-NE* activity in animals exposed to an anxiety-like paradigm reduces the allocation of LC3B-positive vesicles transported from distal *LC-NE* axons back to the *LC-NE* somata

To investigate the trafficking dynamics of autophagic vesicles in *LC-NE* axons projecting to the *PFC in vivo* during noradrenergic systemic activity, I employed a photoconvertible fluorophore, mEOS, and designed an experimental approach involving two distinct behavioral paradigms to modulate neuronal activity in the *LC*. In the first paradigm, animals were placed in an open arena environment to induce anxiety-like behaviors and elicit heightened *LC-NE* activity. In contrast, the second paradigm involved placing the animals in a familiar arena, which maintained spontaneous *LC-NE* neuronal activity (*Fig. 24).*

Therefore, I employed a combinatorial approach, utilizing viral particles injections (AAV-EF1a-DIO-EOS4-LC3B) to label autophagic vesicles in *LC-NE* neurons, and implanted an optical fiber in the *mPFC* to enable photoconversion of EOS4-LC3B in distal *LC-NE* axons. This experimental setup facilitated precise tracking of photoconverted autophagic vesicles within the *LC-PFC* circuit under both baseline (familiar arena/'home cage') conditions and anxiety-provoking (open arena/ 'novel arena') (Yizhar et al., 2011). The optical fiber, connected to a 405 nm laser via a 1.5m flexible fiber, enabled the establishment of two distinct experimental groups: the 'home cage' group, which comprised animals exposed to UV light stimulation (1-second pulses, 10-second intervals, for a total duration of 10 minutes) within their familiar arena, and the 'novel arena' group, which included animals subjected to the same UV light stimulation protocol but placed in a novel arena designed to induce stress-related anxiety, thereby enhancing *LC-NE* neuronal activity and norepinephrine release (Yizhar et al., 2011).

I therefore hypothesized, that animals placed in the open arena, characterized by higher *NE* release, would exhibit increased activation of β2-AR compared to home cage animals. This, in turn, would result in slower delivery of autophagic vesicles to the *LC-NE* somata, as the trafficking velocity and pattern would favor reduced displacement of LC3B + vesicles along the distal axons of the *LC*.

Six hours after the photoconversion protocol, both animal groups were perfused for immunohistochemistry and anti-tyrosine hydroxylase (TH) staining to label *LC-NE* neurons, and the amounts of 'red' puncta, indicating photoconverted autophagic vesicles arriving from the distal *LC-NE* axons projecting to the *PFC*, were quantified.

As expected, quantitative analysis revealed a higher number of 'red' puncta in *LC-NE* somata in the home cage group compared to the novel arena group (*Fig. 24 B-D*), suggesting that systemic *LC-NE* activation during anxiety-like behavior and subsequent β2-AR activation exerts the opposite effect of *LC-NE* tonic inhibition, thereby slowing autophagic vesicle trafficking *in vivo* through *LC-NE* axons projecting to the *PFC*.

Previous research conducted both in our lab and by others (Cheng et al., 2015; Maria-Alonso et al., 2019; Maria-Alonso et al., 2021; Karpova et al., 2025) has established that PKA activity is critical for the immobilization of amphisomes, RapGAP-SIPA1L2-positive and LC3B -positive hybrid organelles formed through the fusion of autophagosomes with late endosomes/multivesicular bodies (LE/MVBs). To investigate whether LC3B -positive vesicles arriving at the somatic regions exhibit characteristics of amphisomes, I performed immunodetection of SIPA1L2 alongside with mEOS-LC3B puncta (*Fig. 24 E).* Line profile indicate co-localization of both proteins in *LC-NE* somata (*Fig. 24 F).*

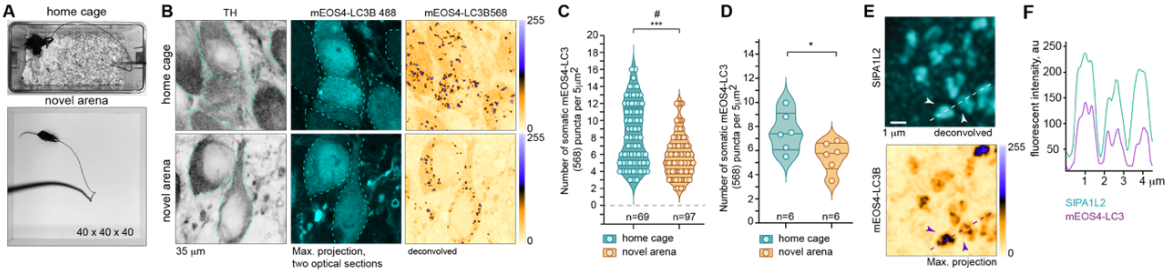

Figure 24| Autophagic vesicle trafficking dynamics in the Locus coeruleus during differential behavioral states

(A) Schematic representation of the experimental design illustrating two behavioral paradigms: Home cage condition (baseline): Animals placed in a familiar environment. Novel arena condition (anxiety-inducing): Animals exposed to a new, open arena environment. (B) Representative image showing photoconverted "red" puncta (mEos-LC3B 568) and "green" soluble mEos-LC3B in the LC-NE soma labeled with anti-TH antibodies across different behavioral conditions. (C) Quantitative analysis of "red" puncta numbers in LC-NE soma per LC-NE brain slice under both behavioral conditions. (D) Quantitative analysis of "red" puncta numbers in LC-NE soma per animal under both behavioral conditions. (E) SIPA1L2 immunoreactivity colocalizes with mEos-LC3B puncta. Scale bar = 1 μm. (F) Line profile of the colocalization between SIPA1L2 and the mEos-LC3B puncta.

Collectively, these findings suggest that the previously described molecular mechanism, linking enhanced PKA activity with prolonged amphisome dwell time, may also apply to the long-range axonal projections of *LC-NE* neurons targeting the *PFC*.

Moreover, the presence of SIPA1L2 in these vesicles may identify the LC3B - containing vesicles as hybrid organelles, commonly referred to as amphisomes (Andres-Alonso et al., 2019; Karpova et al., 2025).

It is well established that α_2-adrenergic receptors (α_2-ARs) are abundant in the distal *LC-NE* axons (Washburn & Moises, 1989). However, evidence for the presynaptic expression of β_2 adrenergic receptors (β_2AR) in distal *LC-NE* axons remains contradictory (Starke & Majewski, 1981).

Therefore next, I investigated whether β_2AR (β_2 adrenergic receptors) are present in the distal *LC-NE* axons projecting to the PFC. For this, I employed an AAV strategy as described above (*Fig. 21*) and expressed GFP exclusively in *LC-NE* neurons. Subsequent 3D reconstructions, masking, and analysis revealed the presence of β_2AR immunoreactivity within the distal *LC-NE* axons projecting to the PFC *in vivo* (*Fig. 25).*

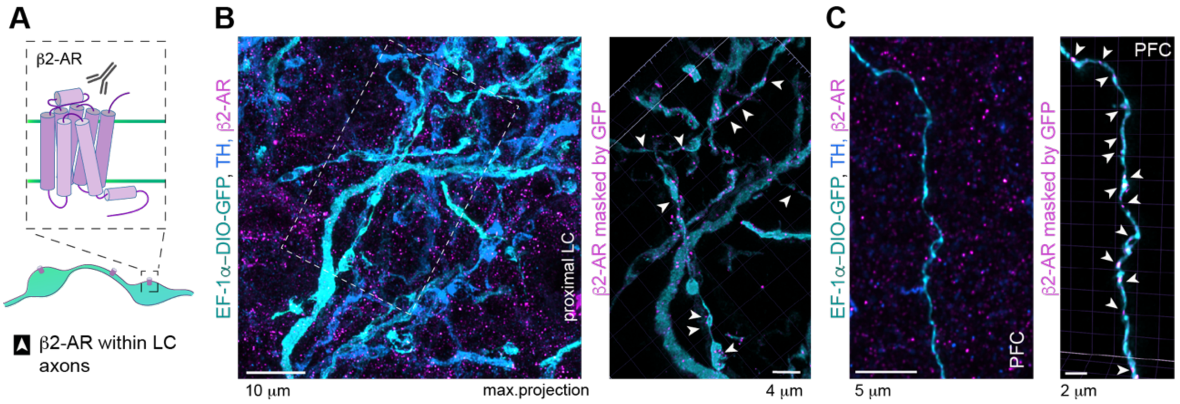

***Figure 25*| β_2AR are sparsly expressed in distal LC-NE axons projecting to the PFC**

(A) An illustration depicting β_2AR localization in the synaptic bouton. (B) A representative image of β_2AR staining in proximal LC-NE axonal terminals following overexpression with EF-1a-DIO-GFP, with immunostaining against TH to confirm expression localization. In the right panel, white arrows indicate β_2AR localization after masking out all non-GFP-expressing structures, ensuring that β_2AR is specifically within the presynaptic terminal. (C) A similar immunostaining approach was applied to distal LC-NE axons in the PFC region, with β_2AR and TH labeling. The right panel highlights β_2AR puncta localized within masked GFP-expressing LC-NE axonal terminals.

Given the autocrine mechanisms regulating subcellular processes in *LC-NE* axons, the functional interplay between β2-AR and α2-AR, along with their opposing effects on PKA signaling, may be key to modulating trafficking velocity and altering the directionality of autophagic vesicle trafficking within distal axons projecting to the PFC *in vivo.* However, whether *NE* release from *LC-NE* axons regulates the trafficking velocity and motility patterns of amphisomes in an autocrine-like fashion remains elusive.

3. 6. Changes in spontaneous norepinephrine release correlate with distinct autophagic vesicle trafficking patterns.

The *locus coeruleus* is the primary source of norepinephrine in the brain (Swanson & Hartman, 1975; Loughlin et al., 1986; Berridge & Waterhouse, 2003; Szabadi, 2013). To detect the autocrine release of NE from *LC-NE* axons, I employed a recently developed genetically encoded fluorescent sensor for rapid and specific *in vivo* detection of norepinephrine, the next-generation GRABNE2h (Feng et al., 2019; Feng et al., 2024). To assess the correlation between amphisome motility patterns and spontaneous NE release, I co-expressed the NE sensor, which emits within the EGFP-comparable spectral range, in *LC-NE* neurons alongside an autophagic vesicle marker fused to mRuby3 (*Fig. 14*).

Initially, I evaluated the expression of GRABNE2h in *LC-NE* axons projecting to the *PFC* using two-photon microscopy through a transcranial window. This approach enabled the real-time monitoring of NE dynamics within *LC-NE* axons, providing an ideal means to non-invasively track of NE release with high spatiotemporal resolution, as demonstrated by(Feng et al., 2024).

Thus, the expression of GRABNE2h in distal *LC-NE* axons and its spontaneous signal fluctuations demonstrated the suitability of this genetically encoded NE indicator for combinatory *in vivo* time-lapse imaging to investigate the correlation between norepinephrine release at synaptic boutons of distal *LC-NE* axons projecting to the *PFC* and autophagic vesicle trafficking (*Fig. 26 A–C*).

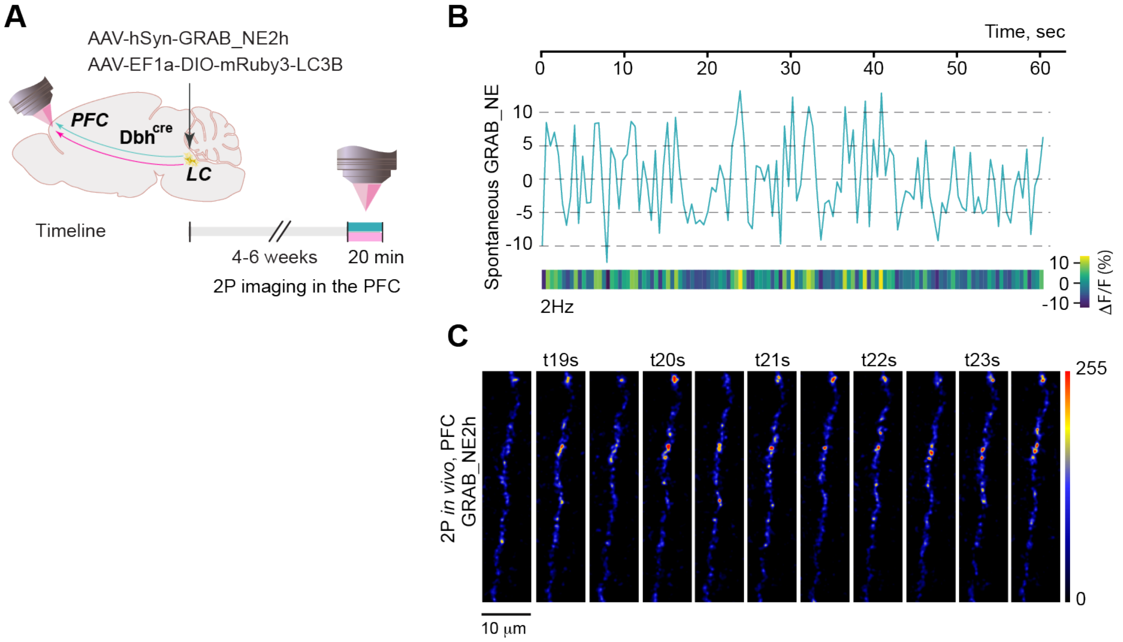

Figure 26** | 2P-imaging of spontaneous NE release from LC-NE axons projecting to the PFC by means of* **GRABNE2h** ***fluorescent signal fluctuations

(A) Schematic illustration of the experimental design. AAV-hSyn-GRABNE2h with AAV-EF1a-DIO-mRuby3-LC3B was injected into the locus coeruleus (LC), followed by transcranial window implantation over the PFC. Two-photon imaging was performed 4–6 weeks post-surgery to assess sensor expression and spontaneous fluctuations of GRABNE2h fluorescence. (B) Representative two-photon images showing GRABNE2h expression in LC-NE distal axons within the PFC. (C) The sensor exhibits clear signal fluctuations, indicating dynamic norepinephrine release sensed during spontinous activity of the LC. The heatmap in B represents the scoring of the signal flactuation of dF/Fo% across the recording period.

3.6.1. Lowering NE release in *LC-NE* axons projecting to the *PFC* correlates with amphisome mobilization

After confirming NE sensor expression and changes in GRABNE2h fluorescence intensities in *LC-NE* axons projecting to the *PFC*, I conducted combinatorial imaging to simultaneously track amphisome motility patterns and spontaneous *NE* dynamics (*Fig. 26 A*). As expected, I observed both unidirectional and bidirectional mobile amphisomes consistent with previous findings. The GRABNE2h probe, previously validated for detecting electrically evoked NE release, exhibited significant increases in fluorescence intensity under such conditions. However, a major challenge I encountered during correlative analysis was that $\Delta F/F_0\%$ of GRABNE2h, reflecting spontaneous NE release, displayed relatively small changes compared to evoked NE release. To address this, and to further investigate the correlation between spontaneous NE release and amphisome dynamics within axons, I developed a detailed spatiotemporal analysis pipeline employing the TRACKMATE algorithm (section 2.4.1. for details).

Specifically, I extracted the **amphisome unidirectional mobilization events** from the track edge (the imaged part of an axon), allowing for the analysis of vesicle spatial appearance across sequentially acquired image frames. This approach provided a unique set of features, including changes in directionality, variations in velocity, and pauses in trafficking compared to previous frames. I defined an “amphisome unidirectional mobilization event” as a time point when a vesicle’s motility shifted from low to no movement after previously exhibiting trafficking behavior along the axon, referring to this event as the "trigger" (*Fig. 27-A*). Next, I analyzed a 15-second temporal window of GRABNE2h fluorescent intensity fluctuations around the “trigger” point, averaging the signal across all detected triggers in multiple recorded axons from the obtained datasets (*Fig. 27-B*).

Interestingly, automated analysis revealed that the GRABNE2h sensor detects a decrease in NE release from *LC-NE* axons approximately 3 seconds prior to the trigger event, as indicated by significant changes in valley values (*Fig. 27 C*). This suggests that spontaneous inactivity of *LC-NE* axons, resulting in reduced NE levels, may enhance the probability of amphisome unidirectional mobilization. Further analysis of peak values before and after the trigger event revealed no significant changes (*Fig. 27 C, D*).

Collectively, this results indicate that lowering *NE* levels in distal *LC-NE* axons projecting to the *PFC* facilitates amphisome unidirectional mobilization. Moreover, these findings are consistent with observations from chemogenetic interference with the *LC-NE* neuronal activity, both converging on the same regulatory mechanism underlying amphisome unidirectional mobilization.

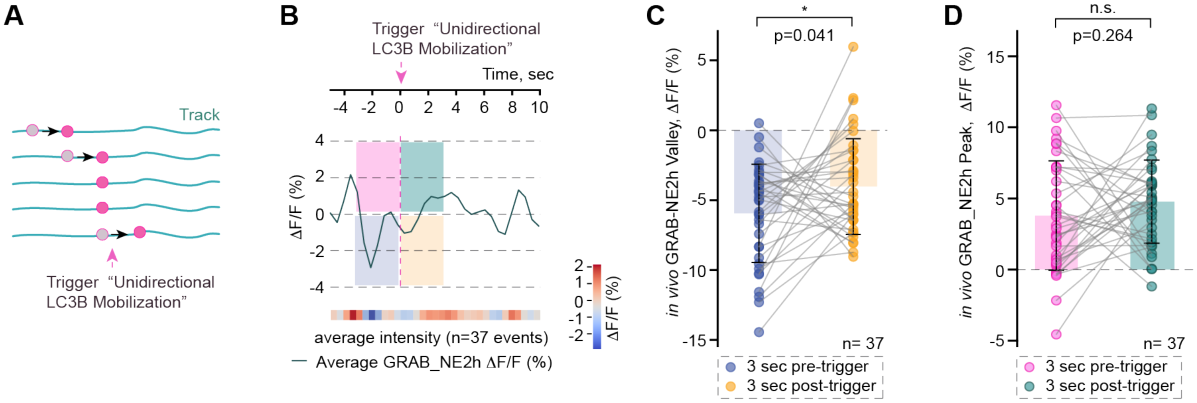

Figure 27| Lowering NE release in LC-NE axons projecting to the PFC correlates with amphisomes mobilization

(A) Schematic representation of the trigger selection of amphisome trafficking. (B) Averaged GRABNE2h signal ($\Delta F/F_0\%$) aligned to the trigger time point, showing a reduction in NE release approximately 3 seconds before mobilization. (C) Quantification reveals no significant change in peak values, while valley values were significantly lower before the trigger compared as compated to the value after, suggesting that reduced NE release facilitates amphisome mobilization. (D) Analysis of GRABNE2h peak values of $\Delta F/F_0\%$ before and after the trigger event showed no signifcant differences supporting the idea of overall reduction in NE release before the trigger initiation.

3.6.2. Amphisome bidirectionality during spontaneous *NE* release across distal *LC-NE* axons

LC3B$^+$ vesicles rely on molecular motors for transport to lysosomes (Maday and Holzbaur, 2016; Kulkarni and Maday, 2018). Both motor proteins with opposite polarity, dynein (Jahreiss et al., 2008; Batlevi et al., 2010; Kimura et al., 2008; Cai & Ganesan, 2022; Cason et al., 2023) and kinesins (Maday et al., 2012), participate in LC3B + vesicles transport along microtubules (reviewed in Kast & Dominguez, 2017; Manbiar & Manjithaya, 2024), and both co-fractionate with axonal autophagosomes (Maday et al., 2012). Furthermore, brain-derived autophagosome profiling has identified multiple motor proteins and their adaptors associated with the cytoplasmic leaflet of autophagosomes, along with SIPA1L2 (Goldsmith et al., 2022). The involvement of various dynein adaptors adds further complexity to the logistics of

LC3B + vesicles trafficking (Cheng et al., 2015; Andres-Alonso et al., 2019; Cai and Ganesan, 2022; reviewed in Nambiar & Manjithaya, 2024).
Consistent with previous findings, time-lapse two-photon *in vivo* imaging revealed frequent instances of sudden directional changes of LC3B -positive vesicles within distal *LC-NE* axons projecting to the *PFC* under conditions of spontaneous neuronal activity (*Fig. 16 A*). Furthermore, as described above, principal component analysis demonstrated shifts in the distribution of LC3B -positive vesicle motility from bidirectional to unidirectional patterns in response to chemogenetic tonic inhibition of *LC-NE* activity mediated by hM4D(Gi) and J60 (*Fig. 20 A-C*).

Therefore, I set out to investigate how sudden changes in the directionality of LC3B - positive vesicles correlate with NE release in distal axons of the *LC-NE* projecting to the *PFC.* Consequently, a second "trigger," reflecting changes in amphisome directionality, was identified in the current dataset and defined by the feature of "bidirectionality," which, in molecular terms, reflects shifts in the preferential association of amphisomes with either dynein or kinesins motor proteins. This trigger was selected based on edge characteristics of bidirectionality, identified at the time point when the directionality of vesicle movement changed relative to the preceding time point, as illustrated in *Fig. 28 A.*

Using the TRACKMATE algorithm, I extracted “amphisome bidirectionality switch” events from the track edge (the imaged part of an axon) and assessed changes in GRABNE2h intensities before and after the switch. Automated analysis of peak and valley values of the GRABNE2h sensor, reflecting increases and decreases in NE release, respectively, centered around the “track” (*amphisome bidirectionality switch*), revealed significant changes in peak values before and after the trigger, without significant diffrences in valley values. These changes suggest that shifts in bidirectionality occur in response to enhanced spontaneous NE release, with is further increase in spontaneous NE release observed in the post-trigger time window within distal *LC-NE* axons projecting to the *PFC*, as shown in the average ΔF/F plot (*Fig. 28 B*). In contrast, no significant differences in valley values were detected before and after the bidirectionality switch, suggesting that reductions in NE release do not influence this parameter. This finding further supports the observation that a reduction in NE release, as indicated by valley values, rather associates with unidirectional amphisome mobilization.

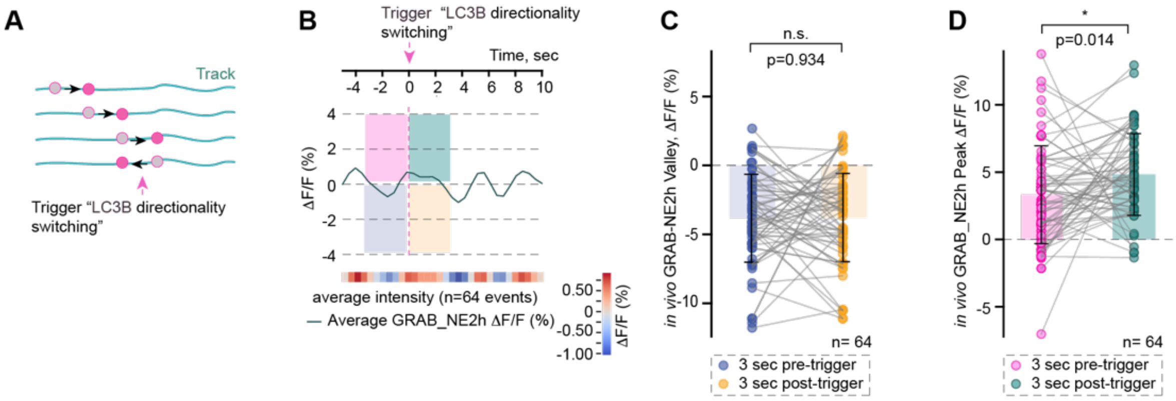

Figure 28| Vesicle movement bidirectionality during spontaneous NE release across LC-NE distal axons

(A) Schematic representation of extracted trigger point for identifying bidirectional Avs movement. The trigger was defined as the time point where Avs directionality changed relative to the previous frame. (B) Averaged GRABNE2h signal ($\Delta F/F_0\%$) aligned to the trigger, showing no significant fluctuations beyond normal spontaneous activity. (C-D) Statistical analysis of valley and peak values. Valley values remained unchanged, while peak values significantly increased post-trigger, suggesting a subtle elevation in NE release following Avs directionality changes.

3.6.3. Stationary pauses of LC3B-positive vesicles within distal *LC-NE* axons correlate with enhanced NE release

Stationary pauses of LC3B+ vesicles at synaptic boutons have attracted particular interest and were recently shown to depend on two molecular mechanisms operating downstream of cAMP and PKA activation (*Fig. 10*.; Andres-Alonso et al., 2019): (a) modulating the interaction of amphisomes with the dynein motor complex, a process facilitated by the motor adaptor protein Snapin (Cai et al., 2010; Xie et al., 2015; Andres-Alonso et al., 2019); and (b) regulating motor processivity by modulating the GTPase-activating protein (GAP) activity of RapGAP SIPA1L family members, which have been identified in association with the outer membrane leaflet of autophagosomes (Andres-Alonso et al., 2019; Goldsmith et al., 2022). Although the current experimental settings did not allow for the detection of distal synaptic boutons localized within *LC-NE* axons projecting to the *PFC*, I observed multiple events characterized by amphisome stationary pauses *in vivo*. Consequently, a third "trigger" reflecting amphisome stationary pauses was identified in the current dataset using the TRACKMATE algorithm. This trigger was defined by the feature of "stationary pauses," characterized as periods of immobilization lasting for at least 3 seconds, preceded by clear amphisome motility, as illustrated in *Fig. 29 A*. Analysis of spontaneous GRABNE2h fluorescence changes around the trigger revealed a significant increase in peak values within a two-second time window surrounding the trigger event (from -1 to +1 second relative to the trigger), compared to the preceding two seconds prior to immobilization (*Fig. 28 D*). These results suggest that NE spontaneous release levels were elevated in the two seconds preceding amphisome immobilization and remained elevated following the stationary pause (*Fig. 29*). In this observed scenario, the elevation of NE release appears to induce amphisome immobilization, while subsequent stationary pauses "help" maintain high levels of spontaneous NE release. Thus, these findings suggest that enhanced *LC-NE* activation and the concomitant increase in NE release from distal *LC-NE* axons projecting to the *PFC* slow down amphisome trafficking by promoting their immobilization. These data are consistent with observations showing that higher *LC-NE* activity during anxiety-like behavior reduces the number of LC3B - positive photoconverted in the PFC vesicles reaching the soma (*Fig. 24*). Additionally, in line with previous observations (Andres-Alonso et al., 2019), stationary pauses of LC3B -positive vesicles may contribute to the local activation of synaptic vesicle release machinery.

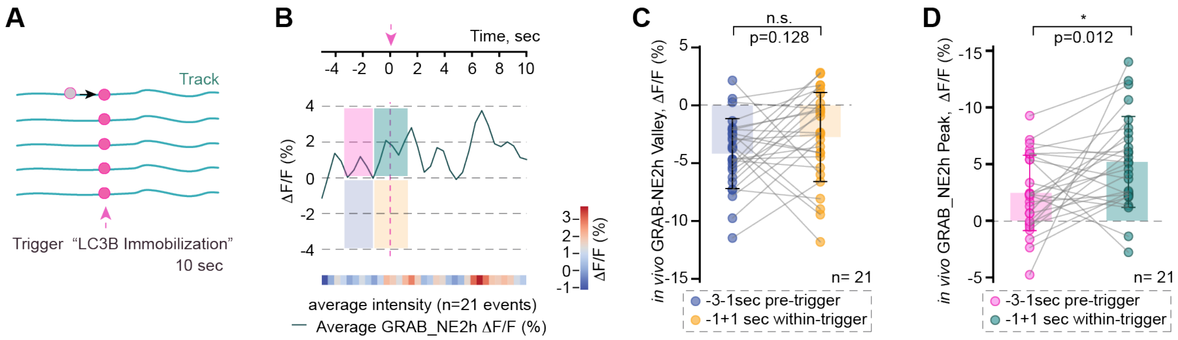

Figure 29| Enhanced NE release correlated with stationary pauses of LC3B-positive vesicles within distal LC-NE axons

(A) Schematic representation of the trigger selection for identifying stopover events in autophagosome (Avs) trafficking. Triggers were defined as vesicles exhibiting at least 3 seconds of immobility following active transport. (B) Averaged GRABNE2h signal ($\Delta F/F_0\%$) aligned to the trigger, showing elevated NE release within a 2-second window around the stopover. (C-D) Statistical analysis of peak and valley values of $\Delta F/F_0\%$. Peak values were significantly higher during the -1 to +1 second window compared to the -3 to -1 second period, while valley values

showed no significant differences. These results indicate that LC-NE activation transiently reduces Avs trafficking by inducing stopover behavior.

3.7. What molecular mechanisms kick in for the regulation of amphisome motility patterns?

LC3B^{+} vesicles navigate through the axons using **motor-adaptor-mediated strategies** (Cheng et al. 2015, Jordens et al. 2001, Wijdeven et al. 2016) and association with scaffolding proteins (Fu et al. 2014, Wong & Holzbaur 2014b), to enable fast and slow motility of autophagic vesicles, stationary pauses, prolonged stops with varying dwell times, and fusion with other organelles (Cason et al., 2021; Cason & Holzbaur, 2023). Several **motor-adaptor-mediated** strategies for navigating autophagic vesicles and amphisomes, hybrid organelles in the autophagy pathway, was described (Chheda et al., 2001; Pankiv et al., 2010; Tumbarello et al., 2012; Di Giovanni & Sheng, 2015; Andres-Alonso et al., 2019; Cason et al., 2021; Cason & Holzbaur, 2023).

Snapin functions as an adaptor that recruits dynein motors to late endosomes and amphisomes by binding to the DIC (Cai et al., 2010, *Fig. 5, Fig. 6*). Upon phosphorylation by PKA, Snapin dissociates from the motor, promoting organelle immobilization at synaptic botons (Chheda et al., 2001; Di Giovanni & Sheng, 2015; Andres-Alonso et al., 2019). Knowing that amphisome trafficking in *LC-NE* axons might be controlled by SIPA1L2 (*Fig. 24 F*), I hypothesized that the dynein motor adaptor Snapin and a PKA-dependent mechanism might contribute to navigating amphisomes within the distal *LC-NE* axons projecting to the PFC. Additionally, Snapin dephosphorylation may lead to the recruitment of Snapin to the motor and initiate movement, as observed during tonic *LC-NE* inhibition (*Fig. 27*).

Previous observations in the lab suggest that SIPA1L2 is part of a protein complex with spinophilin (Fig. 30 A), the scaffolding protein and regulatory subunit of protein phosphatase-1 (PP1). Being associated with both spinophilin and Snapin, SIPA1L2 may provide local regulation for Snapin dephosphorylation and association with the motor for the LC3B +-vesicle mobilization .

To address this hypothesis, in collaboration with Anna Karpova, we investigated the association between SIPA1L2 and Spinophilin using the HEK293T cell model and live imaging (*Fig. 30 B*). We found that overexpressed RapGAP-PDZ, a short version of SIPA1L2 tagged with tRFP, and Spinophilin tagged with HA (detected using 15F11-

HascFv-mEGFP nanobodies) were co-recruited into the vesicular compartments (*Fig. 30 B-C*). To determine whether Snapin was also recruited into the same vesicular compartments, we employed the SNAPIN-SNAP-cell647-SiR labeling approach for three-color confocal live imaging, confirming that all proteins were indeed present in the same vesicular compartment (*Fig. 30 D*).

Finally, to assess whether Spinophilin might contribute to the regulation of amphisome motility in *LC-NE* neurons, I evaluated the abundance of Spinophilin in *LC-NE* neurons. For this, I performed immunohistochemical analysis using anti-Spinophilin alongside anti-TH (tyrosine hydroxylase, a marker for *LC-NE* neurons). The results confirmed the localization of Spinophilin in *LC-NE* neurons (*Fig. 30 E*), further supporting its possible involvement in the regulation of trafficking complexes within *LC-NE* neurons. Further experiments, such as verifying the substrate specificity of PP1 for Snapin and Spinophilin gene manipulation in the regulation of amphisome mobilization and trafficking, are needed and may be addressed after my defense.

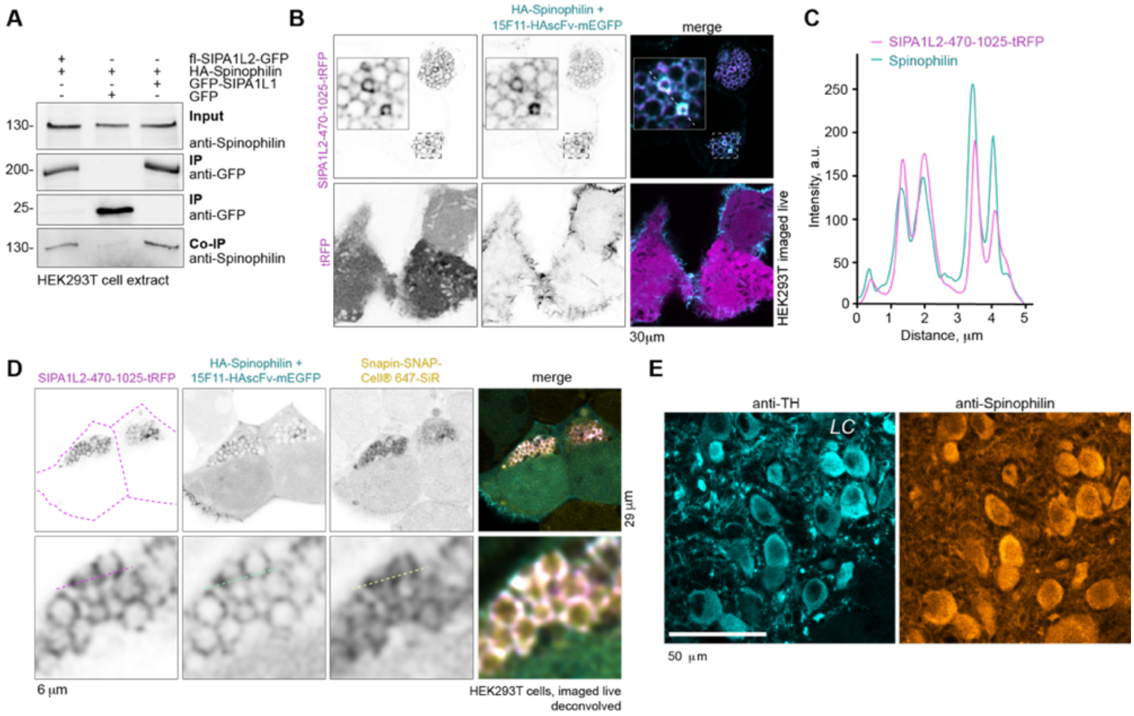

Figure 30| SIPA1L2 associates with Snapin and the regulatory subunit of PP1, Spinophilin, which may control Snapin dephosphorylation and the immobilization of amphisome trafficking

(A) Co-immunoprecipitation (Co-IP) and Western blot analysis demonstrating the interaction between SIPA1L2 and Spinophilin in HEK293T cells. SIPA1L2-GFP and HA-Spinophilin were co-expressed, and Co-IP confirmed their association, suggesting their role in the motor protein regulatory complex. (B) Confocal immunocytochemistry (ICC) imaging of SIPA1L2-470-1025-tRFP (RapGAP-PDZ) and HA-Spinophilin, with anti-HA labeled with mEGFP. High colocalization

was observed, indicating a strong interaction between SIPA1L2 and Spinophilin, compared to the control condition (tRFP alone). (C) A histogram of collocalized spinophilin with SIPA1L2 (RapGAP-PDZ domain). (D) Live-cell imaging of HEK293T cells co-expressing SIPA1L2-470-1025-tRFP (RapGAP-PDZ), HA-Spinophilin+15F11-HascFv-mEGFP, and SNAPIN-SNAP-cell647-SiR. The colocalization of SIPA1L2 (RapGAP-PDZ), Spinophilin, and SNAPIN suggests their functional interaction in the motor protein docking complex for Avs trafficking. (E) Immunohistochemical staining of LC-NE neurons, using anti-Spinophilin alongside anti-TH (tyrosine hydroxylase, an LC-NE neuronal marker). The presence of Spinophilin in LC-NE neurons supports its role in the motor protein regulatory complex within the LC-NE system.

3.8. Communication between *LC-NE* and *Me5* neurons for cargo disposal

As stated in the introductory section, recent snRNA-seq profiling of the neurotypical adult human *LC*, aimed at comparing NE-positive neurons identified and characterized by their gene expression signatures in the *LC-NE* versus surrounding regions, found the autophagy marker mRNA *MAP1LC3B* among the top 70 significantly elevated genes (Weber et al., 2023). This finding suggests a high demand for autophagy regulation in these neurons. Immunohistochemical analysis confirmed a high abundance of endogenous LC3B in the somatic region of *LC-NE* neurons (*Fig. 31 A*). Next, I assessed the relative abundance of the selective autophagy receptor p62 (Kabeya et al., 2000) (*Fig. 31 B-C*). To my surprise, I observed that p62 levels were markedly higher in *LC-NE* neurons compared to adjacent mesencephalic trigeminal nucleus (*Me5*) neurons (*Fig. 31 D-C*).

Given that the *locus coeruleus* is a highly active neuronal population with a substantial demand for lysosomal degradation to maintain neuronal proteostasis, I further examined lysosomal abundance in *LC-NE* neuronal somata compared to adjacent *Me5* neurons. For this, I performed immunohistochemistry for the lysosomal resident proteins LAMP2a and LAMP1, two well-characterized lysosomal markers. Intriguingly, LAMP2b-positive puncta were significantly less abundant in *LC-NE* neurons compared to neighboring *Me5* neurons, as shown in (*Fig. 31 D-F*). Similarly, LAMP1 staining further confirmed the limited presence of lysosomal vesicles in *LC-NE* neurons compared to *Me5* neurons (*Fig. 32*).

Intrigued by these unexpected observations and aiming to further explore the disposal of autophagic cargo through the interplay between *LC-NE* neurons and adjacent *Me5* neurons, I assessed the possibility that *LC-NE* neurons might employ a secretory autophagy mechanism for cargo disposal, while adjacent *Me5* neurons, given their heightened digestive capacity, could contribute to cargo clearance.

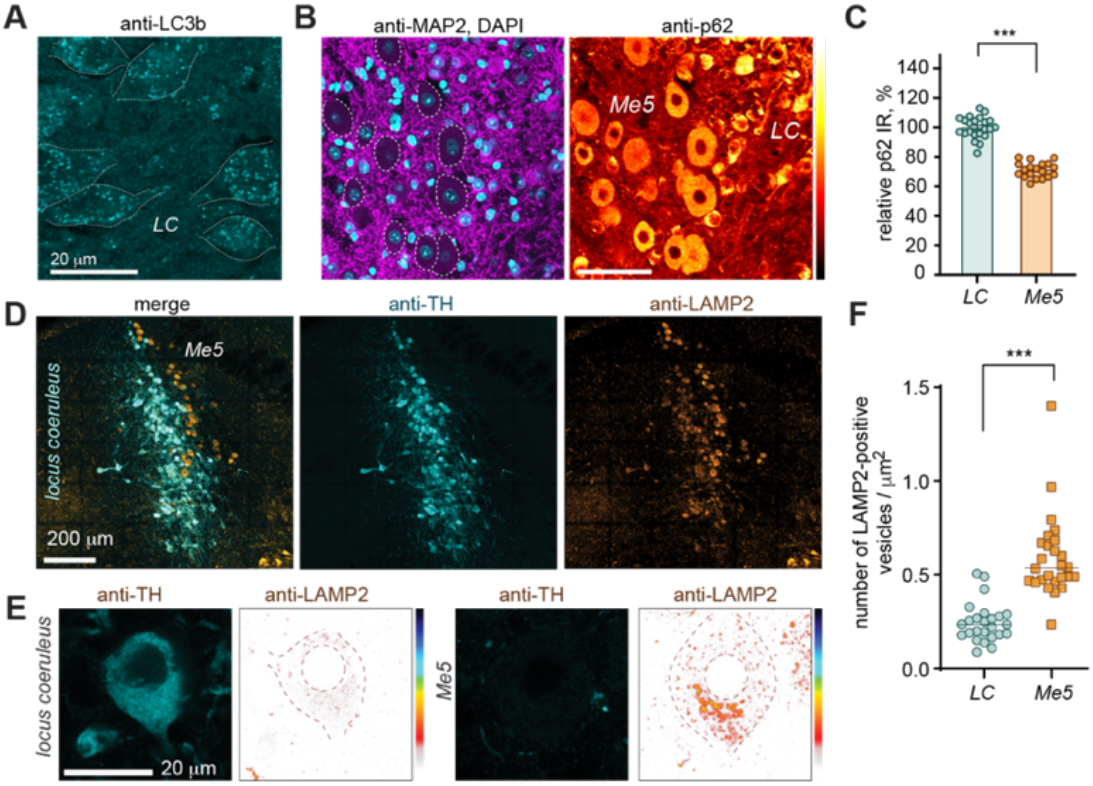

Figure 31| p62 and LAMP2a expression in LC-NE and Me5 neurons

(A) Representative immunohistochemistry (IHC) images showing the localization of LC3B postivie vesicels in LC-NE neurons. (B) immunostaining for MAP2 and Dapi to distigution morphologicaly between Me5 and LC-NE neurons, on the right panel its immunostaining of P62, an autophagy marker and cargo receptor, in LC-NE and Me5 neurons. (C) quantification of P62 intensity in Me5 relative to LC-NE neurons. LC-NE neurons exhibit significantly higher P62 levels compared to Me5 neurons, indicating an elevated autophagic flux despite limited lysosomal content. (D) Representative immunohistochemistry (IHC) images showing LAMP2 in yellow and TH in cyne in LC-NE neuons and its lateral proximity neurons Me5. (E) representitve high mangification imaging of LAMP2 in glow lookup table and TH staining in cyne across LC-NE and Me5 neurons. (F) Quantification of LAMP2-positive puncta reveals significantly lower lysosomal presence in LC-NE neurons relative to Me5 neurons.

To directly test whether autophagic cargo from *LC-NE* neurons can be transferred to *Me5* neurons, I selectively expressed mRuby3-LC3B in *LC-NE* neurons using the AAV approach and Cre-recombinase system and examined whether mRuby3 fluorescence could be detected in the somatic regions of *Me5* neurons (*Fig. 33 A*).

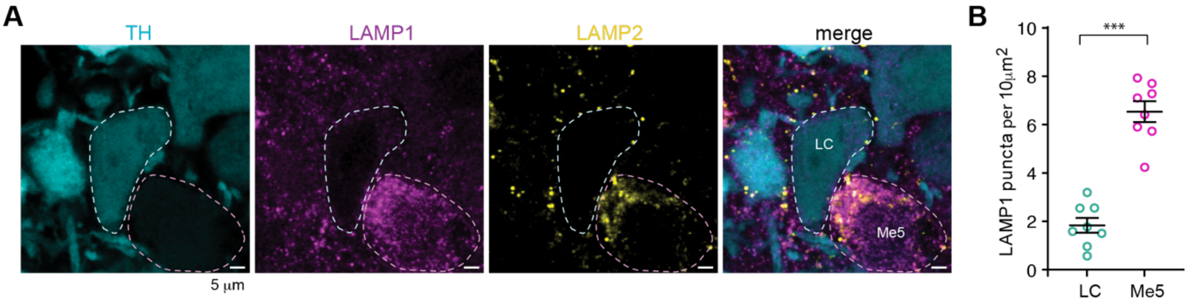

Figure 32| LAMP1 expression in LC-NE and Me5 neurons

(A). Representative confocal images showing the expression of LAMP1 in TH-positive neurons of the LC, compared to adjacent Me5 neurons. (B). Quantitative analysis of LAMP1-positive puncta in LC-NE neurons versus Me5 neurons (t-test).

As expected, mRuby3-positive puncta within *Me5* neurons were positive for ATG16L1, a marker of autophagosome membranes (highlighted by the white dashed circles in *Fig. 33B*), and the colocalization of mRuby3-LC3B with ATG16L1 in *Me5* neurons provided strong evidence that *LC-NE* neurons may transfer autophagy-related membranous compartments to neighboring neurons with higher digestive capacities (*Fig. 33 C*).

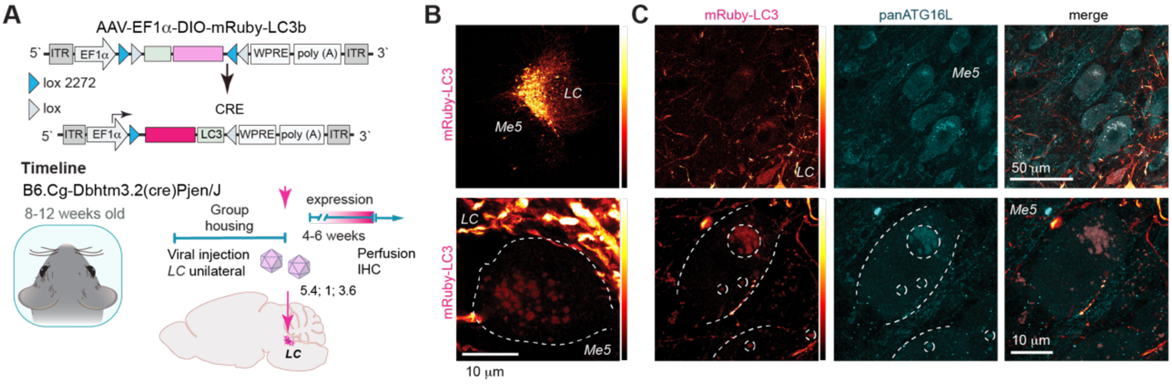

Figure 33| Transfer of LC-derived autophagic vesicles to Me5 neurons

(A) Schematic of the experimental approach using AAV-EF1a-DIO-mRuby-LC3B expression in LC-NE neurons of DbH-Cre expressing animal to track autophagic vesicle (Avs) location. (B) Representative IHC images showing mRuby-LC3B -positive puncta in both LC-NE and Me5 neurons, suggesting intercellular transfer of Avs. (C) Colocalization of mRuby-LC3B with PanATG16L1, a key autophagosome membrane marker, within Me5 neurons (white circles) confirms that the transferred vesicles retain autophagic characteristics. Scale bar: 10um

These finding strongly indicate that along the classical digestive autophagy *LC-NE* neurons may employ an alternative secretory autophagy pathway for cargo disposal and *LC-NE* neurons may outsource part of their autophagic degradation process to adjecent *Me5* neurons, revealing a potential neuron-to-neuron cargo transfer mechanism to support cellular homeostasis.

Secretory autophagy is mediated by SNARE proteins, including Sec22b (see the Introduction for a detailed description), and multiple studies have identified Sec22b in secretory vesicles (Kimura et al., 2017a; Kimura et al., 2017b; Martinelli et al., 2021). To investigate whether the activity or inactivity states of *LC-NE* neurons influence secretory autophagy, I employed hM4D(Gi) (*Fig. 34 A*) and assessed Sec22b puncta using Sec22b knockdown-verified antibodies under conditions of spontaneous neuronal activity and tonic neuronal inhibition. Intriguingly, under tonic *LC-NE* inhibition, Sec22b puncta were scarcely detectable, supporting the notion that the activity state of *LC-NE* neurons may regulate secretory autophagy and membrane exchange between *LC-NE* and *Me5* neurons.

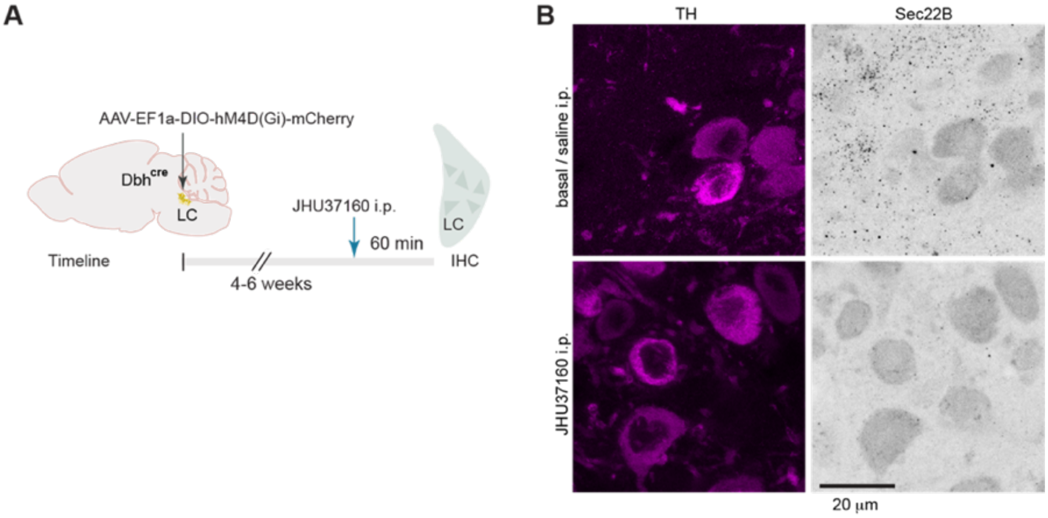

Figure 34| Inhibition of LC-NE activity reduces the amount of Sec22B puncta

(A). Timeline of the experiment showing AAV injection of EF1a-DIO-hM4D(Gi)-mCherry into the locus coeruleus of DBH-CRE mice and subsequent IP injection of JHU37160. (B). Confocal laser scans depicting decreased amounts of Sec22B puncta in the LC-NE upon LC-NE inactivation.hM4D(Gi)-mCherry was largely quenched after antigen retrieval with 10 mM sodium citrate buffer. TH- tyrosine hydroxylase

4. Discussion

In my thesis, I investigated network-related cellular mechanisms that regulate neuronal proteostasis in the *locus coeruleus* - a population of highly vulnerable neurons essential for modulating various brain functions - through autophagy during different states of *LC-NE* activity and wakefulness-associated behaviors. My research specifically explores the trafficking mechanisms of autophagy-related organelles, particularly LC3B -positive hybrid organelles, known as amphisomes, *in vivo*. In particular, I examined how these organelles navigate through the distal axons of *LC-NE* neurons projecting to the *PFC* and how their trafficking velocities and motility patterns are regulated by neuronal activity and autocrine sensing of norepinephrine release. Additionally, I identified previously overlooked, significant differences in lysosomal machinery between tyrosine hydroxylase-positive neurons of the *LC-NE* and neighboring mesencephalic trigeminal neurons. My findings suggest a functional interplay between these neuronal populations, indicating that *LC-NE* neurons may utilize secretory autophagy as an alternative pathway for membrane trafficking when their intrinsic degradative capacity is limited. Furthermore, *Me5* neurons may support *LC-NE* neurons in clearing unwanted damaged proteins and metabolites, highlighting a potential **cooperative mechanism** in maintaining neuronal proteostasis.

I employed an array of state-of-the-art technologies to study the *in vivo* navigation of LC3B -positive amphisomes trought the *LC-NE* axons projecting to the *PFC*. These included the development and characterization of molecular tools, specifically, the establishment of efficient *LC*-specific labeling of autophagy-related membranal compartments *in vivo*, and the implementation of various surgical procedures, such as transcranial window surgery, optical fiber implantation, and virus injection combined with photoconversion or two-photon imaging in conjunction with behavioral assays. Additionally, I employed chemogenetic approach to modulate *LC-NE* activity, followed by brain tissue processing for histological analysis, immunohistochemistry, and confocal microscopy.

To investigate the relationship between norepinephrine release and amphisome trafficking, I utilized the recently developed GRAB-NE2h NE sensor (Feng et al., 2023) to assess the correlation between *NE* release and the trafficking velocities and motility patterns of autophagic vesicles in distal *LC-NE* axons projecting to the *PFC*. Furthermore, I developed a detailed, spatiotemporal automated analysis pipeline based on the TRACKMATE algorithm to analyze LC3B -positive vesicle trafficking.

These methodologies collectively enabled me to confirm the overarching hypothesis that a reduction in neuronal activity and norepinephrine release in the distal axons of the locus coeruleus projecting to the *PFC* accelerates amphisome trafficking, a hybrid organelle in the autophagy pathway, by altering their directionality, reducing stopovers, and ensuring their faster delivery to the *LC-NE* soma for disposal.

4.1. Locus coeruleus specific labelling of autophagic vesicles *in vivo*

To the best of my knowledge, this study is the first to investigate the trafficking of autophagy-related organelles in axons of deep brain regions, such as the *locus coeruleus*, *in vivo.* Microtubule-associated protein 1A/1B-light chain 3 (LC3B) is a well-characterized protein involved in the autophagy pathway (Tanida et al., 2008; Mizushima et al., 2008) and is widely used as a marker for tracking autophagic vesicles in live-cell imaging studies, both *in vitro*, *ex vivo*, and *in vivo* (Fu et al., 2022; Chen et al., 2010). Despite its widespread use in various applications, LC3B overexpression has limitations, as it has the potential to alter the threshold for autophagy induction. With recent advancements in CRISPR/Cas9-based strategies, such as Targeted Knock-In with Two (TKIT) guides targeting non-coding regions (Fang et al., 2021), it is now possible to tag endogenous proteins with fluorescent markers. However, further optimization of fluorophore brightness and stability is needed, especially for *in vivo* two-photon imaging through the transcranial window, to compensate for the lower expression levels of endogenous proteins.

To ensure the precision and reliability of my findings, I implemented several controls to assess the expression levels of the autophagy marker. Specifically, I: i) titrated adeno-associated virus prior to animal experimentation to achieve optimal expression, and ii) conducted multiple two-photon imaging sessions to monitor and validate the appropriate overexpression levels of the autophagy marker fused to a fluorescent protein, particularly in experimental settings involving cranial window imaging. A key challenge I encountered in this process involved the use of two-color 2P imaging, particularly in combination with the recently developed norepinephrine sensor. The expression of both AAVs required transduction along the same trajectories and comparable expression levels of LC3 and GRAB-NE, ensuring the simultaneous visualization of both markers. Additionally, axons that met these criteria and were oriented parallel to the cranial window were selected for further investigation.

As I stated in the results section, LC3B protein expresses in two distinct forms: the cytosolic form (LC3-I) and the conjugated form with phosphatidylethanolamine, known as the LC3-phosphatidylethanolamine conjugate (LC3-II), which is subsequently recruited to autophagosomal membranes. The expression of the mNeonGreen fluorescent protein and mRuby3 fised to LC3B effectively mirrored these distinct forms, with the soluble LC3B form also serving as a marker for intact axons. During 2P imaging, I observed instances of immobile clusters or clumps of fluorescently tagged LC3B , which likely reflect an enhanced threshold for autophagy induction in certain axons due to very high expression levels. These axons were excluded from investigation. The presence of soluble LC3B under these conditions served as a criterion for identifying healthy axons, and this formed the basis for my preselection of axons for analysis (*Fig. 12).*

4.2. Dynamic characteristics of LC3B-positive vesicles in distal *LC-NE* axons projecting to the PFC *in vivo*

The maintenance of proteostasis relies on the efficient functioning of endo-lysosomal and autophagy systems and is particularly crucial for the survival of long-range projecting norepinephrinergic neurons of the locus coeruleus. Precise regulatory mechanisms must be in place to coordinate the delivery of autophagic cargo for degradation, ensuring the maintenance and survival of the most burdened cells in the brain. Therfore, understanding how autophagic vesicles navigate through axons in living animals will provide critical insights for targeted therapeutic interventions.

Studying axonal autophagosome trafficking *in vivo* presents significant challenges.

We recently highlighted technological advancements, particularly the ultra-thin laser-scanning endomicroscope, which enables subcellular resolution of membranous compartments for in vivo imaging in relation to neuronal activity and animal behavior (Stibůrek et al., 2023; Karpova, Aly et al., 2024).

In my thesis, I visualized and analyzed the trafficking dynamics of vesicles associated with the autophagy pathway. Although imaging through the narrow field of view provided by the transcranial window in the current experimental setup does not yield information about the directionality of autophagic vesicle trafficking, it also limits the ability to detect axonal terminals. However, it enables the visualization of distal axonal segments containing *en passant* synaptic boutons, allowing for a detailed characterization of the trafficking velocities and motility patterns of LC3B+ amphisomes, hybrid organelles on the autophagy pathway, *in vivo*.

Another challenge in *in vivo* imaging of axons through a transcranial window arises from the anatomy of locus coeruleus projections in distal regions. These axons are embedded within the brain tissue in a three-dimensional branching pattern and frequently traverse different depths. As a result, acquiring a Z-stack to cover the full depth of labeled axons is necessary, but this compromises the temporal resolution required to capture fast trafficking events. To address these constraints, only axons positioned within the focal plane, achievable with 5–7 optical sections, were selected for imaging. Consequently, only axons oriented parallel to the field of view were included, allowing for shortened acquisition times per Z-stack. This approach facilitated the imaging of labeled vesicles with the temporal resolution necessary to capture their redistribution and analyze trafficking events.

Classical kymograph analysis, commonly employed to characterize axonal organelle trafficking patterns in cultured neurons was found to be not informative for capturing the complexities of 4D *in vivo* imaging. To overcome these limitation, I implemented a customized image-processing approach that incorporats measures of vesicles size and dynamic features such as velocity, displacement, and change in directionality over the imaging period. For detailed information, please refer to the “Materials and Methods” section.

I analyzed the trafficking characteristics and motility patterns of autophagic vesicles during spontaneous *LC-NE* activity and categorized them accordingly. This analysis identified three distinct populations of autophagic vesicles based on their trafficking velocities and motility patterns: slow bidirectional, fast bidirectional, and slow unidirectional.

What can we learn from the descriptive characteristics of LC3B +amphisome trafficking velocities and motility patterns in the context of their physiological significance?

In the context of their degradative function, $LC3^+$ vesicles exhibiting fast velocities and/or retrograde unidirectional motility are more likely to reach neuronal somata more efficiently, facilitating cargo delivery for the degradation. In contrast, vesicles with slower dynamics and low displacement ratios may function in local cargo collection or signaling, analogous to the roles of amphisomes described previously (Andres-Alonso et al., 2019; Andres-Alonso et al., 2021; Karpova et al., 2025).

4.3. Chemogenetic silencing of *LC-NE* activity accelerates trafficking velocity and alters the directionality of autophagic vesicles trafficking in distal *LC-NE* axons projecting to the *PFC in vivo*

In my thesis, I investigated the role of selective inhibition of *LC-NE* neurons *in vivo*, specifically mediated by the activation of high-affinity α2-adrenergic receptors for norepinephrine (*Fig. 10*). This receptor activity is commonly associated with distinct physiological states of the *LC*, such as specific phases of sleep (Hansen & Manahan-Vaughan, 2015; Nguyen & Connor, 2019; Lim et al., 2010; Lemon et al., 2009; Maity et al., 2015).

Intriguingly, inhibiting *LC-NE* activity using chemogenetic manipulation, via hM4D(Gi) expression and J60 administration, shifted the representative clusters from slow bidirectional, fast bidirectional, and slow unidirectional to slow unidirectional, fast unidirectional, and extra-fast unidirectional. This inhibition also increased the proportion of unidirectional autophagic vesicles from 52.5% to 86.7% and elevated the overall average velocity of autophagic vesicles by more than 50%.

My findings closely aligned with previously published observations in acute optic nerve preparations, where autophagic vesicle trafficking was visualized using two-photon microscopy (Luo et al., 2024). In this study, imaging was conducted with the objective tip immersed in a physiological solution above the optic nerve, and data were acquired under deep anesthesia. The authors reported that under these conditions, the majority (85%) of autophagic vesicles were transported in the retrograde direction.

What could be the physiological significance of changes in trafficking directionality and trafficking velocity during LC-NE inactivation? Could these changes reflect a switch in AV trafficking characteristics corresponding to the physiological state of the LC-NE during sleep stages, when LC-NE neurons become predominantly silent?

As pointed out above, in the context of degradative functions, autophagic vesicles exhibiting higher velocities and/or preferential **retrograde** unidirectional motility are more likely to reach neuronal somata efficiently, thereby facilitating the delivery of cargo for lysosomal degradation. This findings suggest that *LC-NE* inactivation, such as occurs during REM sleep state and in sub-NREM microstructure (A. Osorio-Forero et al. 2024), may optimize AV trafficking by unifying their directionality and enhancing retrograde transport. This unification could support more effective degradative processes, potentially contributing to the maintenance of neuronal proteostasis and synaptic plasticity.

Understanding which specific motility patterns are preferentially employed during *LC-NE* scilencing versus spontaneous neuronal activity *in vivo*, and how these states, physiologically relevant to sleep and wakfulness, modulate the trafficking velocity of autophagic vesicles, provide insights into the activity-dependent regulation of cargo delivery for degradation, a process critical for neuronal proteostasis and survaval. This understanding also underscores the role of sleep and wakefulness in *LC-NE* clearance regulated by the autocrine presynaptic mechanism.

4.4. Distal *LC-NE* axons projecting to the *PFC* exhibit negligible lysosomal machinery for local autophagic cargo disposal and autophagic vesicles can travel retrogradely toward the *LC-NE* somata

Maintenance of proteostasis depends on efficient endo-lysosomal and autophagy systems and is particularly important for survival of long-range projecting norepinephrinergic neurons of the *locus coeruleus* (Llorca-Torralba et al., 2019).

Whether the preferential unidirectional mobility of LC3B$^+$ vesicles observed via transcranial window during *LC-NE* silencing specifically characterizes **retrograde**-directed trafficking remains unresolved. Addressing this question necessitates simultaneous imaging of autophagic vesicle transport and analysis of microtubule orientation, utilizing molecular tools such as the plus-end microtubule tip detection probe EB3-tdTomato, a technique commonly employed in Total Internal Reflection Fluorescence (TIRF) microscopy (Ramirez-Rios et al., 2017; Kok et al., 2024;) and rarely used in vivo (Knabbe et al., 2018; Knabbe et al., 2022). However, under the constraints of the current experimental setup, which involves the simultaneous use of two fluorophores for two-photon *in vivo* microscopy and necessitates rapid image acquisition, this approach is not practically feasible.

To overcome this challenge, I thought first to investigate whether lysosomal machinery is present within the distal *LC-NE* axons projecting to the *PFC*. Lysosomes are generally sparse in distal axons, resulting the retrograde transport of autophagic vesicles to the soma for lysosomal fusion and subsequent degradation (Maday et al., 2012; reviewed in Karpova et al., 2025; Nixon, 2013). *LC-NE* axons rely on retrograde trafficking to meet their synaptic and metabolic demands (Surmeier et al., 2010), and disruptions in autophagic vesicle trafficking in *LC-NE* neurons have been implicated in neurodegenerative diseases such as Parkinson's disease (Fornai et al., 2008).
Furthermore, by utilizing mEOS-LC3B as an autophagosomal marker and optical fiber-mediated photoconversion at the *PFC*, I demonstrated that LC3B-containing amphisomes originating from distal axons in the PFC travels the entire distance to the *locus coeruleus* soma, presumably delivering degradative cargo for disposal by autolysosomes, the final destination of autophagic cargo.

4.5. Heightened *LC-NE* activity in animals exposed to anxiety-like behavior reduces the allocation of LC3B -positive vesicles transported from distal *LC-NE* axons back to the *LC-NE* somata

In the next set of experiments, I established a correlation between the trafficking velocities of autophagic vesicles and animal behavior. Specifically, I investigated how heightened activity of the *locus coeruleus* under conditions associated with anxiety-like behavior, primarily regulated by autocrine mechanisms involving β2-adrenergic receptors, modulates the trafficking parameters of autophagy-related organelles.
I found that the changes in Avs trafficking influenced by activity induction using a novel environment behavioral paradigm that can induce stress and increase the *LC-NE* neuronal excitability (Llorca-Torralba et al., 2019). I performed the same photoconversion experiment in two separate animal groups; first group the photoconversion been performed while the animal located in its home cage (Familiar arena)– normal *LC-NE* neuronal activity– and the second group the photoconversion been performed while the animal introduced into an open arena for the first time (Novel arena) – novelty induce stress induction– led to increase the *LC-NE* neurons excitability. Interestingly, I found that when *LC-NE* neurons is highly activated due to a stress-induced-paradigm the Avs located in *LC-NE* soma that traffics from *PFC*

region back to cell soma become significantly less than number of Avs traffics back to *LC-NE* soma during baseline spontaneous activity.

4.6. Changes in spontaneous norepinephrine release correlate with distinct autophagic vesicle trafficking patterns.

Furthermore, understanding the effect of AVs trafficking velocities and pattern under conditions of systematic *LC-NE* activation or silencing led me to assess the correlation between the NE release and AVs trafficking.

I established a novel methodology to observe AVs trafficking *in vivo* under two-photon microscopy alongside a genetically encoded NE sensor (GRABNE2h) to detect local NE release at distal *LC* axons. Additionally, I established a computational analysis framework to process high-dimensional datasets, enabling the precise segregation of distinct correlations between AVs dynamics and NE release with high temporal resolution.

During the data analysis I encounted some limitations of the GRABNE2h probe. The GRABNE2h was previously validated for detecting electrically evoked NE release, exhibited significant increases in fluorescence intensity under such conditions. However, a major challenge I encountered during correlative analysis was that $\Delta F/F_0\%$ of GRABNE2h, reflecting spontaneous NE release, displayed relatively small changes compared to evoked NE release (Feng et al., 2024).

From this experimental dataset, I have derived three key findings. First, the that lowering *NE* levels in distal *LC* axons projecting to the *PFC* facilitates amphisome unidirectional mobilization. These findings are cohearent with observations from chemogenetic interference with the *LC-NE* neuronal activity, both converging on the same regulatory mechanism underlying amphisome unidirectional mobilization. Second, frequent instances of directional changes of LC3B-positive vesicles within distal *LC* axons projecting to the *PFC* under conditions of spontaneous neuronal activity occur in response to changes in spontaneous NE release, which was significantly higer after the directionality switch. Third, stationary pauses of LC3B-positive vesicles within distal *LC-NE* axons correlate with prolonged enhanced NE release. In line with previous observations (Andres-Alonso et al., 2019), stationary pauses of LC3B-positive vesicles may contribute to the local activation of synaptic vesicle release machinery.

4.7. What molecular mechanisms kick in for the regulation of amphisome trafficking velocities and motility patterns?

In this thesis I characterized the trafficking velocities and motility patterns of amphisomes within *LC-NE* axonal projection targeting the *PFC* under spontaneous *in vivo* activity, as well as across different states of *LC-NE* activation, including chemogenetic inactivation and heightened activity during behavior. This study represents the first to investigate vesicular trafficking along the autophagy pathway in long-range projections from neurons situated deep within the brain. Autophagosomes rely on molecular motors for transport to lysosomes (Lee et al., 2011; Maday and Holzbaur, 2014; Maday et al., 2012; Maday and Holzbaur, 2016; Kulkarni and Maday, 2018) and follows a bidirectional, stop-and-go pattern, regulated by the coordinated activity of plus-end-directed kinesin motors and minus-end-directed dynein-dynactin motors (Jahreiss et al., 2008; Batlevi et al., 2010; Kimura et al., 2008; Cai & Ganesan, 2022; Maday et al., 2012). Additionally, fast and slow motility of autophagic vesicles, stationary pauses, prolonged stops with varying dwell times, and fusion with other organelles are controlled by various **motor-adaptor-mediated strategies** (Cheng et al. 2015, Jordens et al. 2001, Wijdeven et al. 2016) and association with scaffolding proteins (Fu et al. 2014, Wong & Holzbaur 2014b).

Observed bidirectional motility or "back-and-forth motion followed by processive retrograde transport" of LC3B$^+$ vesicles in *LC-NE* distal axons may require the scaffolding protein MAPK8IP1/JIP1**,** that is recruited to autophagosomes through direct binding to LC3 and this association coincides with the initiation of unidirectional retrograde transport (Fu & Holzbaur, 2014). MAPK8IP1/JIP1 interacts directly with the kinesin-1 heavy chain (KIF5/KHC) and the DCTN1/p150Glued subunit of dynactin, a dynein activator. This interaction is regulated by MAPK8/JNK-mediated phosphorylation at S421 within the KIF5-binding domain, such that non-phosphorylated MAPK8IP1/JIP1 sustains retrograde autophagosome transport (Fu & Holzbaur, 2013). In other words, phosphorylation at S421 acts as a molecular switch, governing the directional movement of autophagosomes along the axon (Fu et al., 2014).

However, the potential role of neuronal activity in regulating this motor switch requires further investigation. Whether this mechanism contributes to directionality shifts during *LC* inactivation remains to be determined. Specifically, additional experiments are necessary to (1) evaluate the expression of MAPK8IP1/JIP1 and (2) assess MAPK8/JNK activity states in distal *LC-NE* axons projecting to the *PFC* using specific antibodies. Furthermore, a projection-specific knockout of MAPK8/JNK via the sgRNA-CRISPR/Cas9 system, followed by two-photon imaging analysis of mNeonGreen-LC3B, may provide deeper insights into the key regulatory mechanisms governing directionality shifts under conditions of neuronal silencing.

A different motor-adaptor-mediated mechanism for guiding autophagic vesicles and amphisomes, hybrid organelles within the autophagy pathway, along axons involves Snapin (SNAP25-interacting protein). Snapin acts as an adaptor that recruits dynein motors to late endosomes and amphisomes by binding to the dynein intermediate chain (DIC) (Cai et al., 2010, *Fig. 5, Fig. 6*). Phosphorylation of Snapin by PKA leads to its dissociation from the motor, thereby promoting the immobilization of organelles at synaptic boutons (*Fig. 35, 1;* Chheda et al., 2001; Di Giovanni & Sheng, 2015; Andres-Alonso et al., 2019). Since LC3$^+$ vesicles in the *LC* are positive for SIPA1L2, we hypothesize that stopovers in the distal *LC* axons may be controlled by a Snapin and PKA-dependent mechanism. To explore this, I investigated the role of SIPA1L2's interactor, Spinophilin, a PP1 regulatory subunit, in regulating the reassembly of the Snapin-dynein complex by promoting Snapin dephosphorylation (see *Fig. 35, 2*). I examined the co-recruitment of Snapin, SIPA1L2, and Spinophilin into the same vesicular compartments in a heterologous system.

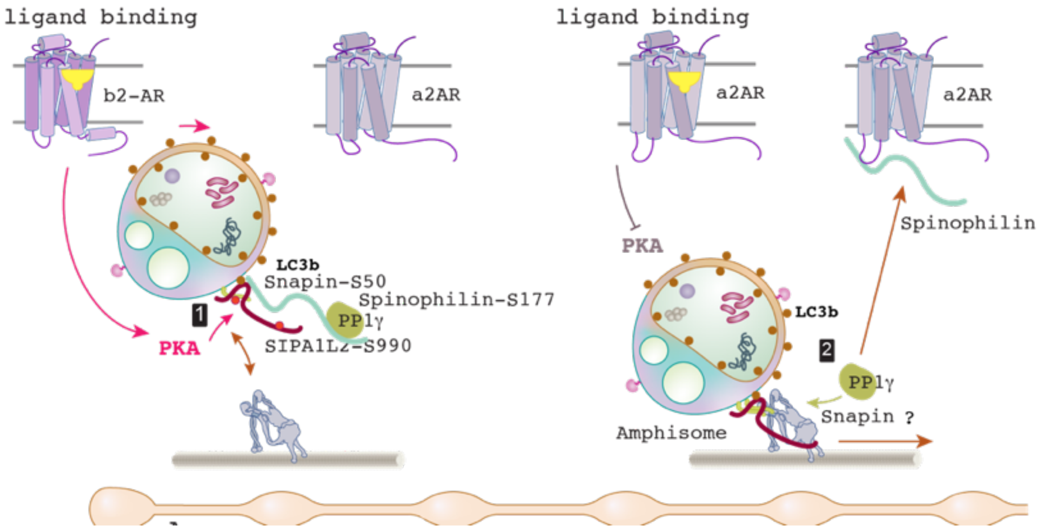

Figure 35| *Illustration of the molecular model of autophagic vesicles immobilization in response to LC-NE neuronal silencing (Graphic courtesy of A. Karpova, used with permission).*

Intriguingly, both processes may require the action of a specific phosphatase, DUSP1/MKP1 (dual specificity phosphatase 1), which likely acts to maintain MAPK8IP1/JIP1 in its dephosphorylated state as autophagosomes are transported toward the cell body (Fu et al., 2014). Additionally, Spinophilin, by recruiting PP1 into the SIPA1L2-Snapin complex, may facilitate the mobilization of LC3^{+} vesicles and support trafficking in the retrograde direction. Further experiments are needed to confirm the involvement of Spinophilin in amphisome mobilization within LC axons, like sgRNA-CRISPR/Cas9-mediated *LC*-specific knock out.

4.8. A compensatory secretory mechanism to regulate cargo degradation via membrane transfer to adjacent neurons with more achive lysosomal machinery

All *in vivo* imaging studies were conducted by labeling vesicles on autophgy pathway using overexpressed, tagged LC3B. Therefore, in the next set of immunohistochemical analysis, I assessed the abundance of endogenous LC3B in the somatic region of *LC-NE* neuron. As expected, I defined multiple LC3B^{+} puncta, , indicating a high demand for autophagy regulation in these neurons.

These findings align with recent snRNA-seq profiling of the neurotypical adult human LC, which aimed to compare NE-positive neurons, characterized by their gene expression signatures in the LC versus surrounding regions. Notably, this study identified the autophagy marker mRNA MAP1LC3B among the top 70 significantly upregulated genes (Weber et al., 2023).

As further evidence of the heightened autophagy demand in LC-NE neurons, I examined the relative abundance of the selective autophagy receptor p62 (Kabeya et al., 2000). Unexpectedly, I observed that p62 levels were markedly higher in LC-NE neurons compared to adjacent *Me5* neurons.

Given that the *locus coeruleus* is a highly active neuronal population with a substantial demand for lysosomal degradation to maintain neuronal proteostasis, I further investigated lysosomal abundance within the relatively small somata of *LC* neurons (Ref). Immunohistochemical analysis for lysosomal resident proteins LAMP2a and LAMP1, two well-characterized lysosomal markers (Ref), revealed that their abundance is significantly lower in *LC* neurons compared to adjacent *Me5* neurons.

Impaired degradative autophagy due to altered lysosomal function has been shown to induce a shift from digestive to secretory autophagy in non-neuronal cells (Solvic et al., 2022). To investigate the possibility that *LC-NE* neurons employ a compensatory secretion mechanism for cargo disposal, while adjacent *Me5* neurons, with their enhanced degradative capacity, may facilitate cargo clearance, I selectively expressed mRuby3-LC3B in *LC* neurons using the AAV approach and Cre-recombinase system. The detection of mRuby3 fluorescence in the somatic regions of *Me5* neurons, along with its colocalization with ATG16L1, a marker of autophagosome membranes, supports the notion that autophagy-related membranous compartments may be transferred to neighboring neurons with higher degradative capacities. A similar phenomenon has been previously observed, though not explicitly linked to secretory autophagy mechanisms (Goto et al., 2020).

Furthermore, I found that the SNARE protein Sec22b, a key regulator of secretory autophagy (Kimura et al., 2017a; Kimura et al., 2017b; Martinelli et al., 2021; Wu SY et al., 2024; Chang et al., 2024) and a marker of secretory vesicles, was more abundant under conditions of spontaneous neuronal activity but nearly undetectable during chemogenetic neuronal inhibition. These findings suggest that the activity state of *LC-NE* neurons may regulate secretory autophagy and membrane exchange between *LC* and *Me5* neurons.

This mechanism aligns with recent literature on secretory autophagy, which serves dual functions in cellular maintenance. Beyond its role in cargo degradation, secretory autophagy facilitates synaptic remodeling during hyperexcitation states in neuromuscular junctions by modulating GluR abundance and synaptic size, contributing to synaptic plasticity and stress response in the brain (Chang et al., 2024; Martinelli et al., 2021).

The compensatory machinery of cargo degradative processes appears particularly advantageous for *LC-NE* neurons, given their noradrenergic nature and high metabolic demands. This intercellular quality control system likely maintains cellular homeostasis when local degradation capacity is exceeded. During stress responses or periods of elevated protein synthesis, *LC-NE* neurons may generate cellular waste exceeding their limited lysosomal capacity. The vesicular transfer mechanism we identified could serve as a crucial safeguard against the accumulation of potentially toxic protein aggregates, such as Aβ42 or neuromelanin. This protective mechanism may be particularly relevant given *LC-NE* neurons' known vulnerability to degeneration in Parkinson's and Alzheimer's disease. The anatomical positioning of *Me5* neurons in lateral proximity to *LC-NE* neurons appears optimally suited for this supportive degradative function.

However, several critical questions emerge from this work: *What molecular mechanisms govern autophagosome transfer? How does this compensatory machinery progress in various neurodegenerative diseases? Could this pathway be therapeutically targeted to treat neurodegeneration?*

These questions represent promising directions for future investigation in this field.

4.9. Conclusions

To conclude, my findings demonstrate that amphisomes exhibit bidirectional trafficking influenced by the spontaneous activity of LC-NE neurons, mirroring normal daily conditions without any induced stimulation or inhibition. During periods when LC-NE neurons are fully silenced—such as during REM sleep and certain NREM substates—AVs travel retrogradely with increased speed and frequency. This enhanced retrograde movement likely aids in maintaining synaptic integrity by efficiently clearing waste and sustaining a healthy synaptic pool for wakefulness and attention.

Conversely, during states of *LC-NE* activation, as seen in wakefulness or anxiety-like behavior, the mobility of AVs is impaired. This suggests that high neuronal activation disrupts the binding of the dynein motor complex, compromising its role in initiating retrograde trafficking.

These bidirectional phenomena support the hypothesis of dual motor binding to AVs, wherein dynein and kinesin motor complexes compete for dominance. Specifically, during activation, elevated norepinephrine release likely triggers the cAMP/PKA pathway, phosphorylating motor complex regulators and halting motility. In contrast, during sleep, dephosphorylation of the dynein regulatory complex enhances its binding, thereby promoting retrograde trafficking.

Overall, these results underscore the critical balance between neuronal activity states: active periods promote waste accumulation and AV formation, while inhibition during sleep facilitates clearance and optimizes synaptic capacity in alignment with the circadian cycle.

This work also offers new insights into the interplay between neuronal activity, neuromodulation, and autophagy in long-range projecting neurons. Given the essential role of *LC-NE* neurons in cognitive and physiological processes, these findings have broader implications for understanding how autophagic dysfunction might contribute to neurodegenerative diseases such as Alzheimer’s and Parkinson’s disease. Future research should investigate how these mechanisms are altered under pathological conditions and explore whether modulating adrenergic signaling can restore autophagic balance as a potential therapeutic strategy.

5. References

Aman, Y. et al. Autophagy in healthy aging and disease. Nat Aging 1, 634–650 (2021).

Andres-Alonso, M. et al. SIPA1L2 controls trafficking and local signaling of TrkB-containing amphisomes at presynaptic terminals. Nat Commun 10, 5448 (2019).

Andres-Alonso, M., Kreutz, M. R. & Karpova, A. Autophagy and the endolysosomal system in presynaptic function. Cell. Mol. Life Sci. 78, 2621–2639 (2021).

Aránguiz-Urroz, P. et al. Beta(2)-adrenergic receptor regulates cardiac fibroblast autophagy and collagen degradation. Biochim Biophys Acta 1812, 23–31 (2011).

Arimoto, M. et al. The Caenorhabditis elegans JIP3 Protein UNC-16 Functions As an Adaptor to Link Kinesin-1 with Cytoplasmic Dynein. J. Neurosci. 31, 2216–2224 (2011).

Armbruster, B. N., Li, X., Pausch, M. H., Herlitze, S. & Roth, B. L. Evolving the lock to fit the key to create a family of G protein-coupled receptors potently activated by an inert ligand. Proc Natl Acad Sci U S A 104, 5163–5168 (2007).

Arnsten, A. F. T. & Goldman-Rakic, P. S. Selective prefrontal cortical projections to the region of the locus coeruleus and raphe nuclei in the rhesus monkey. Brain Res 306, 9–18 (1984).

Aston-Jones, G. & Bloom, F. E. Activity of norepinephrine-containing locus coeruleus neurons in behaving rats anticipates fluctuations in the sleep-waking cycle. J Neurosci 1, 876–886 (1981).

Aston-Jones, G. & Cohen, J. D. Adaptive gain and the role of the locus coeruleus-norepinephrine system in optimal performance. J Comp Neurol 493, 99–110 (2005).

Aston-Jones, G. & Cohen, J. D. An integrative theory of locus coeruleus-norepinephrine function: adaptive gain and optimal performance. Annu Rev Neurosci 28, 403–450 (2005).

Aston-Jones, G., Chiang, C. & Alexinsky, T. Discharge of noradrenergic locus coeruleus neurons in behaving rats and monkeys suggests a role in vigilance. Prog Brain Res 88, 501–520 (1991)

Aston-Jones, G., Rajkowski, J. & Kubiak, P. Conditioned responses of monkey locus coeruleus neurons anticipate acquisition of discriminative behavior in a vigilance task. Neuroscience 80, 697–715 (1997).

Azarnia Tehran, D., Kuijpers, M. & Haucke, V. Presynaptic endocytic factors in autophagy and neurodegeneration. Curr Opin Neurobiol 48, 153–159 (2018).

Bajar, B. T. et al. Improving brightness and photostability of green and red fluorescent proteins for live cell imaging and FRET reporting. Sci Rep 6, 20889 (2016).

Ban, B.-K. et al. Autophagy Negatively Regulates Early Axon Growth in Cortical Neurons. Mol Cell Biol 33, 3907–3919 (2013).

Berchtold, M. W. & Villalobo, A. The many faces of calmodulin in cell proliferation, programmed cell death, autophagy, and cancer. Biochim Biophys Acta 1843, 398–435 (2014).

Bergles, D. E., Doze, V. A., Madison, D. V. & Smith, S. J. Excitatory actions of norepinephrine on multiple classes of hippocampal CA1 interneurons. J Neurosci 16, 572–585 (1996).

Berkane, R. et al. The function of ER-phagy receptors is regulated through phosphorylation-dependent ubiquitination pathways. Nat Commun 14, 8364 (2023).

Berridge, C. W. & Waterhouse, B. D. The locus coeruleus-noradrenergic system: modulation of behavioral state and state-dependent cognitive processes. Brain Res Brain Res Rev 42, 33–84 (2003).

Bjørkøy, G. et al. p62/SQSTM1 forms protein aggregates degraded by autophagy and has a protective effect on huntingtin-induced cell death. J Cell Biol 171, 603–614 (2005).

Bodnar, R. J., Steiner, S. S., Brutus, M., Ippolito, P. M. & Ellman, S. J. Hypothalamic self-stimulation differs as a function of anodal locus. Psychobiology 6, 48–52 (1978).

Boecker, C. A. & Holzbaur, E. L. F. Vesicular degradation pathways in neurons: at the crossroads of autophagy and endo-lysosomal degradation. Curr Opin Neurobiol 57, 94–101 (2019).

Breton-Provencher, V. & Sur, M. Active control of arousal by a locus coeruleus GABAergic circuit. Nat Neurosci 22, 218–228 (2019).

Burbidge, K. et al. LGALS3 (galectin 3) mediates an unconventional secretion of SNCA/α-synuclein in response to lysosomal membrane damage by the autophagic-lysosomal pathway in human midbrain dopamine neurons. Autophagy 18, 1020–1048 (2022).

Cadwell, K. & Debnath, J. Beyond self-eating: The control of nonautophagic functions and signaling pathways by autophagy-related proteins. The Journal of Cell Biology 217, 813–822 (2018).

Cai, Q. & Ganesan, D. Regulation of neuronal autophagy and the implications in neurodegenerative diseases. Neurobiol Dis 162, 105582 (2022).

Cai, Q. et al. Snapin-Regulated Late Endosomal Transport Is Critical for Efficient Autophagy-Lysosomal Function in Neurons. Neuron 68, 73–86 (2010).

Campos, G. V. et al. The Angiotensin Type 1 Receptor Antagonist Losartan Prevents Ovariectomy-Induced Cognitive Dysfunction and Anxiety-Like Behavior in Long Evans Rats. Cell Mol Neurobiol 40, 407–420 (2020).

Canteras, N. S., Resstel, L. B., Bertoglio, L. J., de Pádua Carobrez, A. & Guimarães, F. S. Neuroanatomy of Anxiety. In Behavioral Neurobiology of Anxiety and Its Treatment (eds. Stein, M. B. & Steckler, T.) 77–96. Springer, 2010.

Carter, M. E., de Lecea, L. & Adamantidis, A. Functional wiring of hypocretin and LC-NE neurons: implications for arousal. Front. Behav. Neurosci. 7, (2013).

Cashikar, A. G. & Hanson, P. I. A cell-based assay for CD63-containing extracellular vesicles. PLoS One 14, e0220007 (2019).

Cason, S. E. & Holzbaur, E. L. F. Axonal transport of autophagosomes is regulated by dynein activators JIP3/JIP4 and ARF/RAB GTPases. J Cell Biol 222, e202301084 (2023).

Cason, S. E. & Holzbaur, E. L. F. Selective motor activation in organelle transport along axons. Nat Rev Mol Cell Biol 23, 699–714 (2022).

Cason, S. E. et al. Sequential dynein effectors regulate axonal autophagosome motility in a maturation-dependent pathway. J Cell Biol 220, e202010179 (2021).

Catanese, A. et al. Retinoic acid worsens ATG10-dependent autophagy impairment in TBK1-mutant hiPSC-derived motoneurons through SQSTM1/p62 accumulation. Autophagy 15, 1719–1737 (2019).

Cavalli, V., Kujala, P., Klumperman, J. & Goldstein, L. S. B. Sunday Driver links axonal transport to damage signaling. J Cell Biol 168, 775–787 (2005).

Cearley, C. N. & Wolfe, J. H. A single injection of an adeno-associated virus vector into nuclei with divergent connections results in widespread vector distribution in the brain and global correction of a neurogenetic disease. J Neurosci 27, 9928–9940 (2007).

Cedarbaum, J. M. & Aghajanian, G. K. Activation of locus coeruleus neurons by peripheral stimuli: modulation by a collateral inhibitory mechanism. Life Sci 23, 1383–1392 (1978).

Chandler, D. J. et al. Redefining Noradrenergic Neuromodulation of Behavior: Impacts of a Modular Locus Coeruleus Architecture. J Neurosci 39, 8239–8249 (2019).

Chang, Y.-C. et al. Identification of secretory autophagy as a mechanism modulating activity-induced synaptic remodeling. Proceedings of the National Academy of Sciences 121, e2315958121 (2024).

Charney, D. S. Monoamine dysfunction and the pathophysiology and treatment of depression. J Clin Psychiatry 59 Suppl 14, 11–14 (1998).

Chen, Z.-H. et al. Autophagy protein microtubule-associated protein 1 light chain-3B (LC3B) activates extrinsic apoptosis during cigarette smoke-induced emphysema. Proc Natl Acad Sci U S A 107, 18880–18885 (2010).

Cheng, X.-T., Zhou, B., Lin, M.-Y., Cai, Q. & Sheng, Z.-H. Axonal autophagosomes recruit dynein for retrograde transport through fusion with late endosomes. J Cell Biol 209, 377–386 (2015).

Chino, H., Hatta, T., Natsume, T. & Mizushima, N. Intrinsically Disordered Protein TEX264 Mediates ER-phagy. Molecular Cell 74, 909–921.e6 (2019).

Choi, J., Jang, H., Xuan, Z. & Park, D. Emerging roles of ATG9/ATG9A in autophagy: implications for cell and neurobiology. Autophagy (2024).

Cizza, G. et al. Decreased stress responsivity of central and peripheral catecholaminergic systems in aged 344/N Fischer rats. J Clin Invest 95, 1217–1224 (1995).

Cockburn, J. J. B. et al. Insights into Kinesin-1 Activation from the Crystal Structure of KLC2 Bound to JIP3. Structure 26, 1486–1498.e6 (2018).

Cohen, L. D. & Ziv, N. E. Neuronal and synaptic protein lifetimes. Curr Opin Neurobiol 57, 9–16 (2019).

Conway, O., Akpinar, H. A., Rogov, V. V. & Kirkin, V. Selective Autophagy Receptors in Neuronal Health and Disease. J Mol Biol 432, 2483–2509 (2020)

Craig, A. D. Spinal and trigeminal lamina I input to the locus coeruleus anterogradely labeled with Phaseolus vulgaris leucoagglutinin (PHA-L) in the cat and the monkey. Brain Res 584, 325–328 (1992).

Cuddy, L. K. et al. Stress-Induced Cellular Clearance Is Mediated by the SNARE Protein ykt6 and Disrupted by α-Synuclein. Neuron 104, 869–884.e11 (2019).

de Lecea, L. et al. The hypocretins: hypothalamus-specific peptides with neuroexcitatory activity. Proc Natl Acad Sci U S A 95, 322–327 (1998).

Di Giovanni, J. & Sheng, Z.-H. Regulation of synaptic activity by snapin-mediated endolysosomal transport and sorting. EMBO J 34, 2059–2077 (2015).

Diao, J. et al. ATG14 promotes membrane tethering and fusion of autophagosomes to endolysosomes. Nature 520, 563–566 (2015).

Dikic, I. & Elazar, Z. Mechanism and medical implications of mammalian autophagy. Nat Rev Mol Cell Biol 19, 349–364 (2018).

Dinamarca, M. C. et al. Complex formation of APP with GABAB receptors links axonal trafficking to amyloidogenic processing. Nat Commun 10, 1331 (2019).

Dupont, N. et al. Autophagy-based unconventional secretory pathway for extracellular delivery of IL-1β. EMBO J 30, 4701–4711 (2011).

Durgan, J. et al. Non-canonical autophagy drives alternative ATG8 conjugation to phosphatidylserine. Mol Cell 81, 2031–2040.e8 (2020).

E, S. Functional neuroanatomy of the central noradrenergic system. Journal of psychopharmacology (Oxford, England) 27, (2013).

Ennis, M., Aston-Jones, G. & Shiekhattar, R. Activation of locus coeruleus neurons by nucleus paragigantocellularis or noxious sensory stimulation is mediated by intracoerulear excitatory amino acid neurotransmission. Brain Research 598, 185–195 (1992).

Evans, C. S. & Holzbaur, E. L. F. Degradation of engulfed mitochondria is rate-limiting in Optineurin-mediated mitophagy in neurons. Elife 9, e50260 (2020).

Farah, B. L. et al. β-Adrenergic Agonist and Antagonist Regulation of Autophagy in HepG2 Cells, Primary Mouse Hepatocytes, and Mouse Liver. PLoS One 9, e98155 (2014).

Feng, X. et al. Hypoxia-induced acetylation of PAK1 enhances autophagy and promotes brain tumorigenesis via phosphorylating ATG5. Autophagy 17, 723–742 (2021).

Feng, Y. et al. A toll-like receptor agonist mimicking microbial signal to generate tumor-suppressive macrophages. Nat Commun 10, 2272 (2019).

Feng, Y. et al. Interplay of energy metabolism and autophagy. Autophagy 20, 4–14 (2024).

Ferrucci, M., Giorgi, F. S., Bartalucci, A., Busceti, C. L. & Fornai, F. The Effects of Locus Coeruleus and Norepinephrine in Methamphetamine Toxicity. Curr Neuropharmacol 11, 80–94 (2013).

Filimonenko, M. et al. Functional multivesicular bodies are required for autophagic clearance of protein aggregates associated with neurodegenerative disease. J Cell Biol 179, 485–500 (2007).

Foley, N. M. et al. A genomic timescale for placental mammal evolution. Science 380, eabl8189 (2023).

Fornasiero, E. F. et al. Precisely measured protein lifetimes in the mouse brain reveal differences across tissues and subcellular fractions. Nat Commun 9, 4230 (2018).

Fu, D. et al. Iron blocks autophagic flux and induces autophagosomes accumulation in microglia. Food Chem Toxicol 181, 114054 (2023).

Fu, H., Pel, A. J. & Hoogendoorn, S. P. Optimization of Evacuation Traffic Management With Intersection Control Constraints. IEEE Trans Intell Transp Syst 16, 376–386 (2015).

Fu, M. & Holzbaur, E. L. F. JIP1 regulates the directionality of APP axonal transport by coordinating kinesin and dynein motors. J Cell Biol 202, 495–508 (2013).

Fu, Y. et al. Persistent Activation of Autophagy After Cisplatin Nephrotoxicity Promotes Renal Fibrosis and Chronic Kidney Disease. Front. Pharmacol. 13 (2022).

Fumagalli, F. et al. Translocon component Sec62 acts in endoplasmic reticulum turnover during stress recovery. Nat Cell Biol 18, 1173–1184 (2016).

Galluzzi, L. et al. Molecular definitions of autophagy and related processes. EMBO J 36, 1811–1836 (2017).

Gardner, J. O., Leidal, A. M., Nguyen, T. A. & Debnath, J. LC3-dependent EV loading and secretion (LDELS) promotes TFRC (transferrin receptor) secretion via extracellular vesicles. Autophagy 19, 1551–1561 (2022).

Gatica, D., Lahiri, V. & Klionsky, D. J. Cargo recognition and degradation by selective autophagy. Nat Cell Biol 20, 233–242 (2018).

Giorgi, A. et al. Brain-wide Mapping of Endogenous Serotonergic Transmission via Chemogenetic fMRI. Cell Reports 21, 910–918 (2017).

Giorgi, F. S. et al. A damage to locus coeruleus neurons converts sporadic seizures into self-sustaining limbic status epilepticus. European Journal of Neuroscience 17, 2593–2601 (2003).

Giorgi, F. S. et al. Activation of brain metabolism and fos during limbic seizures: The role of Locus Coeruleus. Neurobiology of Disease 30, 388–399 (2008).

Giorgi, F. S. et al. Locus Coeruleus and Neuronal Plasticity in a Model of Focal Limbic Epilepsy. Epilepsia 47, 21–25 (2006).

Giorgi, F. S., Galgani, A., Puglisi-Allegra, S., Busceti, C. L. & Fornai, F. The connections of Locus Coeruleus with hypothalamus: potential involvement in Alzheimer's disease. J Neural Transm 128, 589–613 (2021).

Giustino, T. F., Ramanathan, K. R., Totty, M. S., Miles, O. W. & Maren, S. Locus Coeruleus Norepinephrine Drives Stress-Induced Increases in Basolateral Amygdala Firing and Impairs Extinction Learning. J Neurosci 40, 907–916 (2020).

Glatigny, M. et al. Autophagy Is Required for Memory Formation and Reverses Age-Related Memory Decline. Curr Biol 29, 435–448.e8 (2019).

Goldey, G. J. et al. Removable cranial windows for long-term imaging in awake mice. Nat Protoc 9, 2515–2538 (2014).

Goldsmith, J., Ordureau, A., Harper, J. W. & Holzbaur, E. L. F. Brain-derived autophagosome profiling reveals the engulfment of nucleoid-enriched mitochondrial fragments by basal autophagy in neurons. Neuron 110, 967–976.e8 (2022).

Goodwin, L. O. et al. Large-scale discovery of mouse transgenic integration sites reveals frequent structural variation and insertional mutagenesis. Genome Res. 29, 494–505 (2019).

Goto, T. et al. Neurodegeneration of Trigeminal Mesencephalic Neurons by the Tooth Loss Triggers the Progression of Alzheimer's Disease in 3×Tg-AD Model Mice. J Alzheimers Dis 76(4), 1443–1459 (2020).

Grochowska, K. M. et al. Chaperone-mediated autophagy in neuronal dendrites utilizes activity-dependent lysosomal exocytosis for protein disposal. Cell Rep 42, 112998 (2023).

Grochowska, K. M., Andres-Alonso, M., Karpova, A. & Kreutz, M. R. The needs of a synapse—How local organelles serve synaptic proteostasis. EMBO J 41, e110057 (2022)

Gubas, A. & Dikic, I. A guide to the regulation of selective autophagy receptors. The FEBS Journal 289, 75–89 (2022).

Gubas, A. & Dikic, I. ER remodeling via ER-phagy. Molecular Cell 82, 1492–1500 (2022).

Gulati, G., D'Silva, J. P., Liu, Y., Wang, L. & Newman, A. M. Profiling cell identity and tissue architecture with single-cell and spatial transcriptomics. Nat Rev Mol Cell Biol (2024).

Gundelfinger, E. D., Karpova, A., Pielot, R., Garner, C. C. & Kreutz, M. R. Organization of Presynaptic Autophagy-Related Processes. Front. Synaptic Neurosci. 14 (2022).

Hakim, V., Cohen, L. D., Zuchman, R., Ziv, T. & Ziv, N. E. The effects of proteasomal inhibition on synaptic proteostasis. EMBO J 35, 2238–2262 (2016).

Hamasaki, M. et al. Autophagosomes form at ER–mitochondria contact sites. Nature 495, 389–393 (2013).

Hansen, N. & Manahan-Vaughan, D. Hippocampal long-term potentiation that is elicited by perforant path stimulation or that occurs in conjunction with spatial learning is tightly controlled by beta-adrenoreceptors and the locus coeruleus. Hippocampus 25, 1285–1298 (2015).

Hara, T. et al. Suppression of basal autophagy in neural cells causes neurodegenerative disease in mice. Nature 441, 885–889 (2006).

Harrison, R. E. et al. Salmonella Impairs RILP Recruitment to Rab7 during Maturation of Invasion Vacuoles. MBoC 15, 3146–3154 (2004).

Hayat, H. et al. Locus coeruleus norepinephrine activity mediates sensory-evoked awakenings from sleep. Sci Adv 6, eaaz4232 (2020).

Heckmann, B. L. et al. LC3-Associated Endocytosis Facilitates β-Amyloid Clearance and Mitigates Neurodegeneration in Murine Alzheimer's Disease. Cell 178, 536–551.e14 (2019).

Helm, M. S. et al. A large-scale nanoscopy and biochemistry analysis of postsynaptic dendritic spines. Nat Neurosci 24, 1151–1162 (2021).

Hernandez, D. et al. Regulation of Presynaptic Neurotransmission by Macroautophagy. Neuron 74, 277–284 (2012).

Hill, C. et al. Autophagy inhibition-mediated epithelial–mesenchymal transition augments local myofibroblast differentiation in pulmonary fibrosis. Cell Death Dis 10, 1–11 (2019).

Hirschberg, S., Li, Y., Randall, A., Kremer, E. J. & Pickering, A. E. Functional dichotomy in spinal- vs prefrontal-projecting locus coeruleus modules splits descending noradrenergic analgesia from ascending aversion and anxiety in rats. eLife 6, e29808 (2017).

Hoffmann, S. et al. Light-Activated ROS Production Induces Synaptic Autophagy. J. Neurosci. 39, 2163–2183 (2019).

Hollenstein, D. M. & Kraft, C. Autophagosomes are formed at a distinct cellular structure. Curr Opin Cell Biol 65, 50–57 (2020).

Holtmaat, A. et al. Long-term, high-resolution imaging in the mouse neocortex through a chronic cranial window. Nat Protoc 4, 1128–1144 (2009).

Hoyer, M. J. et al. Combinatorial selective ER-phagy remodels the ER during neurogenesis. Nat Cell Biol 26, 378–392 (2024).

Hutchings, A.-J. et al. Plekhg5 controls the unconventional secretion of Sod1 by presynaptic secretory autophagy. Nat Commun 15, 8622 (2024).

Huttlin, E. L. et al. Architecture of the human interactome defines protein communities and disease networks. Nature 545, 505–509 (2017).

Itakura, E., Kishi-Itakura, C. & Mizushima, N. The Hairpin-type Tail-Anchored SNARE Syntaxin 17 Targets to Autophagosomes for Fusion with Endosomes/Lysosomes. Cell 151, 1256–1269 (2012).

Jahn, R., Cafiso, D. C. & Tamm, L. K. Mechanisms of SNARE proteins in membrane fusion. Nat Rev Mol Cell Biol 25, 101–118 (2024).

Jahreiss, L., Menzies, F. M. & Rubinsztein, D. C. The Itinerary of Autophagosomes: From Peripheral Formation to Kiss-and-Run Fusion with Lysosomes. Traffic 9, 574–587 (2008).

Jasmin, L., Tien, D., Janni, G. & Ohara, P. T. Is noradrenaline a significant factor in the analgesic effect of antidepressants? PAIN 106, 3 (2003).

Jian, F. et al. The STX17-SNAP47-VAMP7/VAMP8 complex is the default SNARE complex mediating autophagosome–lysosome fusion. Cell Res 34, 151–168 (2024).

Jiang, P. & Mizushima, N. Autophagy and human diseases. Cell Res 24, 69–79 (2014).

Jin, X. et al. Identification of a Group of GABAergic Neurons in the Dorsomedial Area of the Locus Coeruleus. PLOS ONE 11, e0146470 (2016).

Jodo, E., Chiang, C. & Aston-Jones, G. Potent excitatory influence of prefrontal cortex activity on noradrenergic locus coeruleus neurons. Neuroscience 83, 63–79 (1998).

Johansen, T. & Lamark, T. Selective Autophagy: ATG8 Family Proteins, LIR Motifs and Cargo Receptors. J Mol Biol 432, 80–103 (2020).

Jordens, I. et al. The Rab7 effector protein RILP controls lysosomal transport by inducing the recruitment of dynein-dynactin motors. Curr Biol 11, 1680–1685 (2001).

Joshi, S., Li, Y., Kalwani, R. M. & Gold, J. I. Relationships between Pupil Diameter and Neuronal Activity in the Locus Coeruleus, Colliculi, and Cingulate Cortex. Neuron 89, 221–234 (2016).

Kabeya, Y. et al. LC3, a mammalian homologue of yeast Apg8p, is localized in autophagosome membranes after processing. EMBO J 19, 5720–5728 (2000).

Kallergi, E. et al. Dendritic autophagy degrades postsynaptic proteins and is required for long-term synaptic depression in mice. Nat Commun 13, 680 (2022).

Kane, M. J. et al. For Whom the Mind Wanders, and When, Varies Across Laboratory and Daily-Life Settings. Psychol Sci 28, 1271–1289 (2017).

Karpova, A. et al. Encoding and transducing the synaptic or extrasynaptic origin of NMDA receptor signals to the nucleus. Cell 152, 1119–1133 (2013).

Karpova, A. et al. Neuronal autophagy in the control of synapse function. Neuron 0 (2025).

Karpova, A., Aly, A. A. A., Marosi, E. L. & Mikulovic, S. Fiber-based in vivo imaging: unveiling avenues for exploring mechanisms of synaptic plasticity and neuronal adaptations underlying behavior. Neurophotonics 11, S11507 (2024).

Kast, D. J. & Dominguez, R. The Cytoskeleton-Autophagy Connection. Curr Biol 27, R318–R326 (2017).

Katsumata, K. et al. Dynein- and activity-dependent retrograde transport of autophagosomes in neuronal axons. Autophagy 6, 378–385 (2010)

Keary, K. M., Gu, Q.-H., Chen, J. & Li, Z. Dendritic distribution of autophagosomes underlies pathway-selective induction of LTD. Cell Reports 42, (2023).

Khaminets, A. et al. Regulation of endoplasmic reticulum turnover by selective autophagy. Nature 522, 354–358 (2015).

Kim, J. et al. Autophagic Organelles in DNA Damage Response. Front. Cell Dev. Biol. 9, (2021).

Kim, N. H. et al. A p53/miRNA-34 axis regulates Snail1-dependent cancer cell epithelial–mesenchymal transition. Journal of Cell Biology 195, 417–433 (2011).

Kimura, F. & Nakamura, S. Locus coeruleus neurons in the neonatal rat: Electrical activity and responses to sensory stimulation. Dev Brain Res 23, 301–305 (1985).

Kimura, K., Mizoguchi, A. & Ide, C. Regulation of Growth Cone Extension by SNARE Proteins. J Histochem Cytochem 51, 429–433 (2003).

Kimura, S., Noda, T. & Yoshimori, T. Dynein-dependent movement of autophagosomes mediates efficient encounters with lysosomes. Cell Struct Funct 33, 109–122 (2008).

Kimura, T. et al. Dedicated SNAREs and specialized TRIM cargo receptors mediate secretory autophagy. EMBO J 36, 42–60 (2017).

Kirkin, V. & Rogov, V. V. A Diversity of Selective Autophagy Receptors Determines the Specificity of the Autophagy Pathway. Mol Cell 76, 268–285 (2019).

Kirkin, V., McEwan, D. G., Novak, I. & Dikic, I. A role for ubiquitin in selective autophagy. Mol Cell 34, 259–269 (2009).

Kjaerby, C. et al. Memory-enhancing properties of sleep depend on the oscillatory amplitude of norepinephrine. Nat Neurosci 25, 1059–1070 (2022).

Knabbe, J., Nassal, J. P., Verhage, M. & Kuner, T. Secretory vesicle trafficking in awake and anaesthetized mice: differential speeds in axons versus synapses. J Physiol 596, 3759–3773 (2018).

Knabbe, J., Protzmann, J. & Kuner, T. In Vivo Imaging of Axonal Organelle Transport in the Mouse Brain. Methods Mol Biol 2431, 95–109 (2022).

Komatsu, M. et al. Loss of autophagy in the central nervous system causes neurodegeneration in mice. Nature 441, 880–884 (2006).

Kononenko, N. L. et al. Retrograde transport of TrkB-containing autophagosomes via the adaptor AP-2 mediates neuronal complexity and prevents neurodegeneration. Nat Commun 8, 14819 (2017).

Korolchuk, V. I. et al. Lysosomal positioning coordinates cellular nutrient responses. Nat Cell Biol 13, 453–460 (2011).

Korotkova, T. M., Sergeeva, O. A., Ponomarenko, A. A. & Haas, H. L. Histamine excites noradrenergic neurons in locus coeruleus in rats. Neuropharmacology 49, 129–134 (2005).

Kowal, J. et al. Proteomic comparison defines novel markers to characterize heterogeneous populations of extracellular vesicle subtypes. Proc Natl Acad Sci U S A 113, E968–977 (2016).

Kravchick, D. O. et al. Synaptonuclear messenger PRR7 inhibits c-Jun ubiquitination and regulates NMDA-mediated excitotoxicity. EMBO J 35, 1923–1934 (2016).

Kuan, Y.-D., Tsai, C.-Y., Sakakibara, S., Standley, D. & Kikutani, H. External stimulation induces the secretion of autophagosome-like vesicles by B cells. Autophagy Reports (2023).

Kuchitsu, Y. & Taguchi, T. Lysosomal microautophagy: an emerging dimension in mammalian autophagy. Trends Cell Biol 34, 606–616 (2024).

Kuijpers, M. et al. Neuronal Autophagy Regulates Presynaptic Neurotransmission by Controlling the Axonal Endoplasmic Reticulum. Neuron 109, 299–313.e9 (2021).

Kulkarni, V. V. & Maday, S. Neuronal endosomes to lysosomes: A journey to the soma. J Cell Biol 217, 2977–2979 (2018).

Kumar, A. V., Mills, J. & Lapierre, L. R. Selective Autophagy Receptor p62/SQSTM1, a Pivotal Player in Stress and Aging. Front Cell Dev Biol 10 (2022).

Lawson, K. A., Ruiz, C. M. & Mahler, S. V. A head-to-head comparison of two DREADD agonists for suppressing operant behavior in rats via VTA dopamine neuron inhibition. Psychopharmacology (Berl) 240, 2101–2110 (2023).

Lazarevic, V., Schöne, C., Heine, M., Gundelfinger, E. D. & Fejtova, A. Extensive Remodeling of the Presynaptic Cytomatrix upon Homeostatic Adaptation to Network Activity Silencing. J. Neurosci. 31, 10189–10200 (2011).

Lazarou, M. et al. The ubiquitin kinase PINK1 recruits autophagy receptors to induce mitophagy. Nature 524, 309–314 (2015).

Lee, J.-H. & Nixon, R. A. Autolysosomal acidification failure as a primary driver of Alzheimer disease pathogenesis. Autophagy 18, 2763–2764 (2022).

Lee, J.-H. et al. β2-adrenergic Agonists Rescue Lysosome Acidification and Function in PSEN1 Deficiency by Reversing Defective ER-to-lysosome Delivery of ClC-7. J Mol Biol 432, 2633–2650 (2020).

Lee, T.-H. et al. Arousal increases neural gain via the locus coeruleus–noradrenaline system in younger adults but not in older adults. Nat Hum Behav 2, 356–366 (2018).

Lee, Y. et al. Molecular basis of β-arrestin coupling to formoterol-bound β1-adrenoceptor. Nature 583, 862–866 (2020).

Lee, Y. J., Kim, N.-Y., Suh, Y.-A. & Lee, C. Involvement of ROS in Curcumin-induced Autophagic Cell Death. Korean J Physiol Pharmacol 15, 1–7 (2011).

Leidal, A. M. et al. The LC3-conjugation machinery specifies the loading of RNA-binding proteins into extracellular vesicles. Nat Cell Biol 22, 187–199 (2020).

Lemon, N., Aydin-Abidin, S., Funke, K. & Manahan-Vaughan, D. Locus coeruleus activation facilitates memory encoding and induces hippocampal LTD that depends on beta-adrenergic receptor activation. Cereb Cortex 19, 2827–2837 (2009).

Levine, B., Mizushima, N. & Virgin, H. W. Autophagy in immunity and inflammation. Nature 469, 323–335 (2011).

Li, A. et al. Mitochondrial autophagy: molecular mechanisms and implications for cardiovascular disease. Cell Death Dis 13, 1–15 (2022).

Li, J. et al. Regulation and function of autophagy in pancreatic cancer. Autophagy 17, 3275–3296 (2021).

Li, X., He, S. & Ma, B. Autophagy and autophagy-related proteins in cancer. Mol Cancer 19, 12 (2020).

Li, Y. & Chen, Y. AMPK and Autophagy. in Autophagy: Biology and Diseases: Basic Science (ed. Qin, Z.-H.) 85–108 (Springer, Singapore, 2019). doi:10.1007/978-981-15-0602-4_4.

Liang, K. Y. et al. Exercise and Alzheimer's disease biomarkers in cognitively normal older adults. Ann Neurol 68, 311–318 (2010).

Lie, P. P. Y. & Nixon, R. A. Lysosome trafficking and signaling in health and neurodegenerative diseases. Neurobiol Dis 122, 94–105 (2019).

Lieberman, O. J. & Sulzer, D. The Synaptic Autophagy Cycle. J Mol Biol 432, 2589–2604 (2020).

Lim, E. P., Tan, C. H., Jay, T. M. & Dawe, G. S. Locus coeruleus stimulation and noradrenergic modulation of hippocampo-prefrontal cortex long-term potentiation. Int J Neuropsychopharmacol 13, 1219–1231 (2010)

Limanaqi, F., Busceti, C. L., Biagioni, F., Fornai, F. & Puglisi-Allegra, S. Autophagy-Based Hypothesis on the Role of Brain Catecholamine Response During Stress. Front. Psychiatry 11, (2020).

Liu, C. L., Chen, S., Dietrich, D. & Hu, B. R. Changes in Autophagy after Traumatic Brain Injury. J Cereb Blood Flow Metab 28, 674–683 (2008).

Liu, J. et al. Selective autophagy in cancer: mechanisms, therapeutic implications, and future perspectives. Mol Cancer 23, 22 (2024).

Llorca-Torralba, M. et al. Chemogenetic Silencing of the Locus Coeruleus-Basolateral Amygdala Pathway Abolishes Pain-Induced Anxiety and Enhanced Aversive Learning in Rats. Biol Psychiatry 85, 1021–1035 (2019).

Lou, G. et al. Mitophagy and Neuroprotection. Trends Mol Med 26, 8–20 (2020).

Lu, C., Yang, Y., Zhu, Y., Lv, S. & Zhang, J. An Intervention Target for Myocardial Fibrosis: Autophagy. BioMed Research International 2018, 6215916 (2018).

Lu, Z. et al. Locus-specific DNA methylation of Mecp2 promoter leads to autism-like phenotypes in mice. Cell Death Dis 11, 1–11 (2020).

Luo, X. et al. Axonal autophagic vesicle transport in the rat optic nerve in vivo under normal conditions and during acute axonal degeneration. Acta Neuropathologica Communications 12, 82 (2024).

Lw, S. & Bk, H. The central adrenergic system. An immunofluorescence study of the location of cell bodies and their efferent connections in the rat utilizing dopamine-beta-hydroxylase as a marker. J Comp Neurol 163 (1975).

Maday, S. & Holzbaur, E. L. F. Autophagosome biogenesis in primary neurons follows an ordered and spatially regulated pathway. Dev Cell 30, 71–85 (2014).

Maday, S. & Holzbaur, E. L. F. Compartment-Specific Regulation of Autophagy in Primary Neurons. J Neurosci 36, 5933–5945 (2016).

Maday, S., Wallace, K. E. & Holzbaur, E. L. F. Autophagosomes initiate distally and mature during transport toward the cell soma in primary neurons. J Cell Biol 196, 407–417 (2012).

Maejima, I. et al. Autophagy sequesters damaged lysosomes to control lysosomal biogenesis and kidney injury. The EMBO Journal 32, 2336–2347 (2013).

Maity, S., Rah, S., Sonenberg, N., Gkogkas, C. G. & Nguyen, P. V. Norepinephrine triggers metaplasticity of LTP by increasing translation of specific mRNAs. Learn. Mem. 22, 499–508 (2015).

Martinelli, S. et al. Stress-primed secretory autophagy promotes extracellular BDNF maturation by enhancing MMP9 secretion. Nat Commun 12, 4643 (2021).

Masiero, E. et al. Autophagy is required to maintain muscle mass. Cell Metab 10, 507–515 (2009).

Mather, M., Clewett, D., Sakaki, M. & Harley, C. W. Norepinephrine ignites local hotspots of neuronal excitation: How arousal amplifies selectivity in perception and memory. Behav Brain Sci 39, e200 (2016).

Matsui, T. et al. Autophagosomal YKT6 is required for fusion with lysosomes independently of syntaxin 17. J Cell Biol 217, 2633–2645 (2018).

Mauthe, M. et al. Chloroquine inhibits autophagic flux by decreasing autophagosome-lysosome fusion. Autophagy 14, 1435–1455 (2018).

Mazarati, A. M., Baldwin, R. A., Sankar, R. & Wasterlain, C. G. Time-dependent decrease in the effectiveness of antiepileptic drugs during the course of self-sustaining status epilepticus. Brain Res 814, 179–185 (1998).

Mazarati, A., Lu, X., Shinmei, S., Badie-Mahdavi, H. & Bartfai, T. Patterns of seizures, hippocampal injury and neurogenesis in three models of status epilepticus in galanin receptor type 1 (GalR1) knockout mice. Neuroscience 128, 431–441 (2004).

McCall, J. G. et al. CRH Engagement of the Locus Coeruleus Noradrenergic System Mediates Stress-Induced Anxiety. Neuron 87, 605–620 (2015).

McCall, J. G. et al. Locus coeruleus to basolateral amygdala noradrenergic projections promote anxiety-like behavior. eLife 6, e18247.

McGinley, M. J. et al. Waking State: Rapid Variations Modulate Neural and Behavioral Responses. Neuron 87, 1143–1161 (2015).

Minton, K. How lysosomes SNARE autophagosomes. Nat Rev Mol Cell Biol 14, 65 (2013).

Mizushima, N. & Levine, B. Autophagy in mammalian development and differentiation. Nat Cell Biol 12, 823–830 (2010).

Mizushima, N., Levine, B., Cuervo, A. M. & Klionsky, D. J. Autophagy fights disease through cellular self-digestion. Nature 451, 1069–1075 (2008).

Mizushima, N., Yamamoto, A., Matsui, M., Yoshimori, T. & Ohsumi, Y. In vivo analysis of autophagy in response to nutrient starvation using transgenic mice expressing a fluorescent autophagosome marker. Mol Biol Cell 15, 1101–1111 (2004).

Monti, J. M. & Jantos, H. The roles of dopamine and serotonin, and of their receptors, in regulating sleep and waking. Prog Brain Res 172, 625–646 (2008).

Mostany, R. & Portera-Cailliau, C. A craniotomy surgery procedure for chronic brain imaging. J Vis Exp 680 (2008) doi:10.3791/680.

Mou, W. & Cui, Y. Enhancing neuronal reticulophagy: a strategy for combating aging and APP toxicity. Autophagy 20, 2819–2820 (2024).

Mouton, P. R., Pakkenberg, B., Gundersen, H. J. & Price, D. L. Absolute number and size of pigmented locus coeruleus neurons in young and aged individuals. J Chem Neuroanat 7, 185–190 (1994).

Nakamura, S. & Yoshimori, T. New insights into autophagosome–lysosome fusion. J Cell Sci 130, 1209–1216 (2017).

Nakamura, Y., Sawai, T., Kakiuchi, K. & Arawaka, S. Neuronal activity promotes secretory autophagy for the extracellular release of α-synuclein. J Biol Chem 300 (2024).

Nakatogawa, H., Suzuki, K., Kamada, Y. & Ohsumi, Y. Dynamics and diversity in autophagy mechanisms: lessons from yeast. Nat Rev Mol Cell Biol 10, 458–467 (2009).

Nambiar, A. & Manjithaya, R. Driving autophagy - the role of molecular motors. J Cell Sci 137, jcs260481 (2024).

Neisch, A. L., Neufeld, T. P. & Hays, T. S. A STRIPAK complex mediates axonal transport of autophagosomes and dense core vesicles through PP2A regulation. J Cell Biol 216, 441–461 (2017).

Nguyen, P. V. & Connor, S. A. Noradrenergic Regulation of Hippocampus-Dependent Memory.

Nguyen, T. A. & Debnath, J. Control of Unconventional Secretion By The Autophagy Machinery. Current Opinion in Physiology (2022).

Nieves Torres, D. & Lee, S. H. Inter-neuronal signaling mediated by small extracellular vesicles: wireless communication? Front. Mol. Neurosci. 16, (2023).

Nikolac Perkovic, M. et al. Association between the brain-derived neurotrophic factor Val66Met polymorphism and therapeutic response to olanzapine in schizophrenia patients. Psychopharmacology 231, 3757–3764 (2014).

Nikoletopoulou, V., Sidiropoulou, K., Kallergi, E., Dalezios, Y. & Tavernarakis, N. Modulation of Autophagy by BDNF Underlies Synaptic Plasticity. Cell Metab 26, 230–242.e5 (2017).

Nishimura, T. & Tooze, S. A. Emerging roles of ATG proteins and membrane lipids in autophagosome formation. Cell Discov 6, 1–18 (2020).

Nixon, R. A. The role of autophagy in neurodegenerative disease. Nat Med 19, 983–997 (2013).

Okerlund, N. D. et al. Bassoon Controls Presynaptic Autophagy through Atg5. Neuron 93, 897–913.e7 (2017).

Olli-Lähdesmäki, T., Kallio, J. & Scheinin, M. Receptor Subtype-Induced Targeting and Subtype-Specific Internalization of Human α2-Adrenoceptors in PC12 Cells. J Neurosci 19, 9281–9288 (1999).

Overhoff, M. et al. Autophagy regulates neuronal excitability by controlling cAMP/protein kinase A signaling at the synapse. EMBO J 41, e110963 (2022).

Öz-Arslan, D., Durer, Z. A. & Kan, B. G protein-coupled receptor-mediated autophagy in health and disease. British Journal of Pharmacology (n.d.).

Öz-Arslan, D., Yavuz, M. & Kan, B. Exploring orphan GPCRs in neurodegenerative diseases. Front. Pharmacol. 15, (2024).

Palikaras, K., Lionaki, E. & Tavernarakis, N. Mechanisms of mitophagy in cellular homeostasis, physiology and pathology. Nat Cell Biol 20, 1013–1022 (2018).

Pang, K. & Rose, G. M. Differential effects of norepinephrine on hippocampal complex-spike and theta-neurons. Brain Res 425, 146–158 (1987).

Pankiv, S. et al. FYCO1 is a Rab7 effector that binds to LC3 and PI3P to mediate microtubule plus end-directed vesicle transport. J Cell Biol 188, 253–269 (2010).

Picca, A., Faitg, J., Auwerx, J., Ferrucci, L. & D'Amico, D. Mitophagy in human health, ageing and disease. Nat Metab 5, 2047–2061 (2023).

Piletic, K., Alsaleh, G. & Simon, A. K. Autophagy orchestrates the crosstalk between cells and organs. EMBO reports 24, e57289 (2023).

Ponpuak, M. et al. Secretory autophagy. Curr Opin Cell Biol 35, 106–16 (2015).

Rajkowski, J., Kubiak, P. & Aston-Jones, G. Locus coeruleus activity in monkey: phasic and tonic changes are associated with altered vigilance. Brain Res Bull 35, 607–616 (1994).

Rajkowski, J., Majczynski, H., Clayton, E. & Aston-Jones, G. Activation of monkey locus coeruleus neurons varies with difficulty and performance in a target detection task. J Neurophysiol 92, 361–371 (2004).

Ramesh, V. et al. Disrupted sleep without sleep curtailment induces sleepiness and cognitive dysfunction via the tumor necrosis factor-α pathway. J Neuroinflammation 9, 91 (2012).

Reggio, A. et al. Role of FAM134 paralogues in endoplasmic reticulum remodeling, ER-phagy, and Collagen quality control. EMBO Rep 22, e52289 (2021).

Reimer, J. et al. Pupil fluctuations track rapid changes in adrenergic and cholinergic activity in cortex. Nat Commun 7, 13289 (2016).

Rinetti, G. V. & Schweizer, F. E. Ubiquitination Acutely Regulates Presynaptic Neurotransmitter Release in Mammalian Neurons. J. Neurosci. 30, 3157–3166 (2010)

Robbins, T. W. Cortical noradrenaline, attention and arousal. Psychol Med 14, 13–21 (1984).

Ross, J. A. & Van Bockstaele, E. J. The Locus Coeruleus–Norepinephrine System in Stress and Arousal: Unraveling Historical, Current, and Future Perspectives. Front Psychiatry 11, 601519 (2020).

Ross, J. A. & Van Bockstaele, E. J. The Locus Coeruleus–Norepinephrine System in Stress and Arousal: Unraveling Historical, Current, and Future Perspectives. Front Psychiatry 11, 601519 (2021).

Rubinsztein, D. C., Codogno, P. & Levine, B. Autophagy modulation as a potential therapeutic target for diverse diseases. Nat Rev Drug Discov 11, 709–730 (2012).

Rubinsztein, D. C., Gestwicki, J. E., Murphy, L. O. & Klionsky, D. J. Potential therapeutic applications of autophagy. Nat Rev Drug Discov 6, 304–312 (2007).

Samuels, J. F. et al. Prevalence and correlates of hoarding behavior in a community-based sample. Behav Res Ther 46, 836–844 (2008).

Sara, S. J. & Bouret, S. Orienting and Reorienting: The Locus Coeruleus Mediates Cognition through Arousal. Neuron 76, 130–141 (2012).

Sara, S. J. The locus coeruleus and noradrenergic modulation of cognition. Nat Rev Neurosci 10, 211–223 (2009).

Sato, S. et al. Loss of autophagy in dopaminergic neurons causes Lewy pathology and motor dysfunction in aged mice. Sci Rep 8, 2813 (2018).

Saunders, C. & Limbird, L. E. Localization and trafficking of alpha2-adrenergic receptor subtypes in cells and tissues. Pharmacol Ther 84, 193–205 (1999).

Scherer, J., Yi, J. & Vallee, R. B. PKA-dependent dynein switching from lysosomes to adenovirus: a novel form of host-virus competition. J Cell Biol 205, 163–177 (2014).

Schmidt, O. & Teis, D. The ESCRT machinery. Curr Biol 22, R116–R120 (2012).

Schwarz, L. A. & Luo, L. Organization of the locus coeruleus-norepinephrine system. Curr Biol 25, R1051–R1056 (2015).

Se, L. Functional neuroanatomy of the central noradrenergic system. Journal of psychopharmacology (Oxford, England) 27, (2013).

Sesack, S. R., Deutch, A. Y., Roth, R. H. & Bunney, B. S. Topographical organization of the efferent projections of the medial prefrontal cortex in the rat: an anterograde tract-tracing study with Phaseolus vulgaris leucoagglutinin. J Comp Neurol 290, 213–242 (1989).

Shaner, N. C. et al. A bright monomeric green fluorescent protein derived from Branchiostoma lanceolatum. Nat Methods 10, 407–409 (2013).

Shehata, M., Matsumura, H., Okubo-Suzuki, R., Ohkawa, N. & Inokuchi, K. Neuronal Stimulation Induces Autophagy in Hippocampal Neurons That Is Involved in AMPA Receptor Degradation after Chemical Long-Term Depression. J. Neurosci. 32, 10413–10422 (2012).

Singh, R. et al. Autophagy regulates lipid metabolism. Nature 458, 1131–1135 (2009).

Smith, M. D. et al. CCPG1 Is a Non-canonical Autophagy Cargo Receptor Essential for ER-Phagy and Pancreatic ER Proteostasis. Dev Cell 44, 217–232.e11 (2018).

Solvik, T. et al. Autophagy cargo receptors are secreted via extracellular vesicles and particles in response to endolysosomal inhibition or impaired autophagosome maturation. bioRxiv (2021).

Soukup, S.-F. et al. A LRRK2-Dependent EndophilinA Phosphoswitch Is Critical for Macroautophagy at Presynaptic Terminals. Neuron 92, 829–844 (2016).

Starke, K. & Majewski, H. Role of Presynaptic and Postsynaptic Adrenoceptors in Cardiac Function. In Catecholamines and the Heart (eds. Delius, W. et al.) 29–38. Springer, 1981.

Starr, T., Ng, T. W., Wehrly, T. D., Knodler, L. A. & Celli, J. Brucella Intracellular Replication Requires Trafficking Through the Late Endosomal/Lysosomal Compartment. Traffic 9, 678–694 (2008).

Stavoe, A. K. H. & Holzbaur, E. L. F. Autophagy in Neurons. Annu Rev Cell Dev Biol 35, 477–500 (2019).

Stickgold, R. & Walker, M. P. Sleep-dependent memory triage: evolving generalization through selective processing. Nat Neurosci 16, 139–145 (2013).

Suárez-Pereira, I. et al. The Role of the Locus Coeruleus in Pain and Associated Stress-Related Disorders. Biol Psychiatry 91, 786–797 (2022).

Swift, K. M. et al. Abnormal Locus Coeruleus Sleep Activity Alters Sleep Signatures of Memory Consolidation and Impairs Place Cell Stability and Spatial Memory. Current Biology 28, 3599–3609.e4 (2018).

Szymusiak, R. & McGinty, D. Hypothalamic regulation of sleep and arousal. Ann N Y Acad Sci 1129, 275–286 (2008).

Takáts, S. et al. Interaction of the HOPS complex with Syntaxin 17 mediates autophagosome clearance in Drosophila. Mol Biol Cell 25, 1338–1354 (2014).

Takeuchi, T. et al. Locus coeruleus and dopaminergic consolidation of everyday memory. Nature 537, 357–362 (2016).

Tan, S. C., Scherer, J. & Vallee, R. B. Recruitment of dynein to late endosomes and lysosomes through light intermediate chains. MBoC 22, 467–477 (2011).

Tanida, I., Ueno, T. & Kominami, E. LC3 and Autophagy. In Methods Mol Biol 445, 77–88 (2008).

Tartar, J. L. et al. Experimental sleep fragmentation and sleep deprivation in rats increases exploration in an open field test of anxiety while increasing plasma corticosterone levels. Behavioural Brain Research 197, 450–453 (2009).

Terešak, P. et al. Regulation of PRKN-independent mitophagy. Autophagy 18, 24–39 (2022).

Theofilas, P. et al. Locus coeruleus volume and cell population changes during Alzheimer's disease progression: A stereological study in human postmortem brains with potential implication for early-stage biomarker discovery. Alzheimers Dement 13, 236–246 (2017).

Thurston, T. L. M., Wandel, M. P., von Muhlinen, N., Foeglein, Á. & Randow, F. Galectin 8 targets damaged vesicles for autophagy to defend cells against bacterial invasion. Nature 482, 414–418 (2012).

Tian, J.-H. et al. The Role of Snapin in Neurosecretion: Snapin Knock-Out Mice Exhibit Impaired Calcium-Dependent Exocytosis of Large Dense-Core Vesicles in Chromaffin Cells. J Neurosci 25, 10546–10555 (2005).

Tillage, R. P. et al. Elimination of galanin synthesis in noradrenergic neurons reduces galanin in select brain areas and promotes active coping behaviors. Brain Struct Funct 225, 785–803 (2020).

Tsuboyama, K. et al. The ATG conjugation systems are important for degradation of the inner autophagosomal membrane. Science 354, 1036–1041 (2016).

Tsuruoka, M., Matsutani, K., Maeda, M. & Inoue, T. Coeruleotrigeminal inhibition of nociceptive processing in the rat trigeminal subnucleus caudalis. Brain Research 993, 146–153 (2003).

Tumbarello, D. A. et al. Autophagy receptors link myosin VI to autophagosomes to mediate Tom1-dependent autophagosome maturation and fusion with the lysosome. Nat Cell Biol 14, 1024–1035 (2012).

Uhlířová, H. et al. "There's plenty of room at the bottom": deep brain imaging with holographic endo-microscopy. Neurophotonics 11, S11504 (2024).

Uytterhoeven, V. et al. Hsc70-4 Deforms Membranes to Promote Synaptic Protein Turnover by Endosomal Microautophagy. Neuron 88, 735–748 (2015).

Valentino, R. J. & Van Bockstaele, E. Convergent regulation of locus coeruleus activity as an adaptive response to stress. Eur J Pharmacol 583, 194–203 (2008).

van Oostrum, M. et al. The proteomic landscape of synaptic diversity across brain regions and cell types. Cell 186, 5411–5427.e23 (2023).

Vargas, J. N. S., Hamasaki, M., Kawabata, T., Youle, R. J. & Yoshimori, T. The mechanisms and roles of selective autophagy in mammals. Nat Rev Mol Cell Biol 24, 167–185 (2023).

Wagatsuma, A. et al. Locus coeruleus input to hippocampal CA3 drives single-trial learning of a novel context. Proc Natl Acad Sci U S A 115, E310–E316 (2018).

Wahis, J. & Holt, M. G. Astrocytes, Noradrenaline, α1-Adrenoreceptors, and Neuromodulation: Evidence and Unanswered Questions. Front Cell Neurosci 15, 645691 (2021).

Wairkar, Y. P. et al. Unc-51 controls active zone density and protein composition by downregulating ERK signaling. J Neurosci 29, 517–528 (2009).

Waites, C. L. et al. Bassoon and Piccolo maintain synapse integrity by regulating protein ubiquitination and degradation. EMBO J 32, 954–969 (2013).

Wakamatsu, K. et al. Norepinephrine and its metabolites are involved in the synthesis of neuromelanin derived from the locus coeruleus. J Neurochem 135, 768–776 (2015).

Wallace, B. G. Agrin-induced specializations contain cytoplasmic, membrane, and extracellular matrix-associated components of the postsynaptic apparatus. J. Neurosci. 9, 1294–1302 (1989).

Wallace, D. M., Magnuson, D. J. & Gray, T. S. The amygdalo-brainstem pathway: Selective innervation of dopaminergic, noradrenergic and adrenergic cells in the rat. Neurosci Lett 97, 252–258 (1989).

Wan, D.-F., Pan, S.-S., Tong, Y.-S. & Huang, Y. Exercise Preconditioning Promotes Autophagy to Cooperate for Cardioprotection by Increasing LC3 Lipidation-Associated Proteins. Front. Physiol. 12, (2021).

Wang, K. Autophagy and apoptosis in liver injury. Cell Cycle 14, 1631–1642 (2015).

Wang, Q. & Limbird, L. E. Regulated interactions of the alpha 2A adrenergic receptor with spinophilin, 14-3-3zeta, and arrestin 3. J Biol Chem 277, 50589–50596 (2002).

Wang, Q. & Limbird, L. E. Regulation of alpha2AR trafficking and signaling by interacting proteins. Biochem Pharmacol 73, 1135–1145 (2007).

Wang, S., Li, H., Yuan, M., Fan, H. & Cai, Z. Role of AMPK in autophagy. Front Physiol 13 (2022).

Washburn, M. & Moises, H. C. Electrophysiological correlates of presynaptic alpha 2-receptor-mediated inhibition of norepinephrine release at locus coeruleus synapses in dentate gyrus. J Neurosci 9, 2131–2140 (1989).

Weber, A. et al. Analysis of transmission-related third-generation cephalosporin-resistant Enterobacterales by electronic data mining and core genome multi-locus sequence typing. Journal of Hospital Infection 140, 96–101 (2023).

Wei, X. et al. A switch from lysosomal degradation to secretory autophagy initiates osteogenic bone metastasis in prostate cancer. Journal of Extracellular Vesicles 13, (2024).

Weingarten, J. et al. The proteome of the presynaptic active zone from mouse brain. Mol Cell Neurosci 59, 106–118 (2014).

Wijdeven, R. H. et al. Cholesterol and ORP1L-mediated ER contact sites control autophagosome transport and fusion with the endocytic pathway. Nat Commun 7, 11808 (2016).

Wild, P. et al. Phosphorylation of the Autophagy Receptor Optineurin Restricts Salmonella Growth. Science (2011).

Wild, P., McEwan, D. G. & Dikic, I. The LC3 interactome at a glance. J Cell Sci 127, 3–9 (2014).

Winckler, B. et al. The Endolysosomal System and Proteostasis: From Development to Degeneration. J. Neurosci. 38, 9364–9374 (2018).

Wong, Y. C. & Holzbaur, E. L. F. Optineurin is an autophagy receptor for damaged mitochondria in parkin-mediated mitophagy that is disrupted by an ALS-linked mutation. Proc Natl Acad Sci U S A 111, E4439–4448 (2014).

Woolfrey, K. M. & Dell'Acqua, M. L. Coordination of Protein Phosphorylation and Dephosphorylation in Synaptic Plasticity. J Biol Chem 290, 28604–28612 (2015).

Wozniak, A. L., Long, A., Jones-Jamtgaard, K. N. & Weinman, S. A. Hepatitis C virus promotes virion secretion through cleavage of the Rab7 adaptor protein RILP. Proceedings of the National Academy of Sciences 113, 12484–12489 (2016).

Wu, L. et al. Rapamycin Upregulates Autophagy by Inhibiting the mTOR-ULK1 Pathway, Resulting in Reduced Podocyte Injury. PLoS One 8, e63799 (2013).

Wu, M.-Y., Li, Z.-W. & Lu, J.-H. Molecular Modulators and Receptors of Selective Autophagy: Disease Implication and Identification Strategies. Int J Biol Sci 20, 751–764 (2024).

Wu, X. et al. Autophagy regulates Notch degradation and modulates stem cell development and neurogenesis. Nat Commun 7, 10533 (2016).

Xie, H., Cui, Y., Deng, F. & Feng, J. Connexin: a potential novel target for protecting the central nervous system? Neural Regen Res 10, 659 (2015).

Xie, L. et al. Sleep drives metabolite clearance from the adult brain. Science 342, 373–377 (2013).

Xie, Y. et al. Association between white matter alterations and domain-specific cognitive impairment in cerebral small vessel disease: A meta-analysis of diffusion tensor imaging. Front. Aging Neurosci. 14, (2022).

Xie, Y. et al. Posttranslational modification of autophagy-related proteins in macroautophagy. Autophagy 11, 28–45 (2015).

Xu, B. et al. Brain-derived neurotrophic factor regulates energy balance downstream of melanocortin-4 receptor. Nat Neurosci 6, 736–742 (2003).

Xu, H.-T., Pan, F., Yang, G. & Gan, W.-B. Choice of cranial window type for in vivo imaging affects dendritic spine turnover in the cortex. Nat Neurosci 10, 549–551 (2007).

Xu, J., Camfield, R. & Gorski, S. The interplay between exosomes and autophagy – partners in crime. J Cell Sci 131 (2018).

Yamada, K. et al. Extended-synaptotagmin 1 engages in unconventional protein secretion mediated via SEC22B+ vesicle pathway in liver cancer. Proceedings of the National Academy of Sciences 119, e2202730119 (2022).

Yamaguchi, H., Hopf, F. W., Li, S.-B. & de Lecea, L. In vivo cell type-specific CRISPR knockdown of dopamine beta hydroxylase reduces locus coeruleus evoked wakefulness. Nat Commun 9, 5211 (2018).

Yang, G., Pan, F., Parkhurst, C. N., Grutzendler, J. & Gan, W.-B. Thinned-skull cranial window technique for long-term imaging of the cortex in live mice. Nat Protoc 5, 201–208 (2010).

Yang, S. et al. Presynaptic autophagy is coupled to the synaptic vesicle cycle via ATG-9. Neuron 110, 824–840.e10 (2022).

Yizhar, O., Fenno, L. E., Davidson, T. J., Mogri, M. & Deisseroth, K. Optogenetics in neural systems. Neuron 71, 9–34 (2011).

Zerbi, V. et al. Rapid Reconfiguration of the Functional Connectome after Chemogenetic Locus Coeruleus Activation. Neuron 103, 702–718.e5 (2019).

Zhang, W.-J. et al. A 16-channel fiber array-coupled superconducting single-photon detector array with average system detection efficiency over 60% at telecom wavelength. Opt. Lett. 46, 1049 (2021).

Zhang, Y., Chen, Y., Xin, Y., Peng, B. & Liu, S. Norepinephrine system at the interface of attention and reward. Prog Neuropsychopharmacol Biol Psychiatry 125, 110751 (2023).

Zhang, Y., Morgan, M. J., Chen, K., Choksi, S. & Liu, Z. Induction of autophagy is essential for monocyte-macrophage differentiation. Blood 119, 2895–2905 (2012).

Zhao, Q. et al. Calpain 2-mediated autophagy defect increases susceptibility of fatty livers to ischemia–reperfusion injury. Cell Death Dis 7, e2186 (2016).

Zucca, F. A. et al. Neuromelanin organelles are specialized autolysosomes that accumulate undegraded proteins and lipids in aging human brain and are likely involved in Parkinson's disease. NPJ Parkinsons Dis 4, 17 (2018).

Zuluaga-Ramirez, V., Rom, S. & Persidsky, Y. Craniula: A cranial window technique for prolonged imaging of brain surface vasculature with simultaneous adjacent intracerebral injection. Fluids Barriers CNS 12, 1–10 (2015).

6. List of Abbreviations

AD – Alzheimer’s Disease
AMBRA1 – Activating Molecule in Beclin-1-Regulated Autophagy
AMPARs – α-Amino-3-hydroxy-5-methyl-4-isoxazolepropionic acid receptors
AMPK – AMP-activated protein kinase
AP2 – Adaptor Protein complex 2
AR – Adrenergic Receptor
ATG – Autophagy-related gene/protein
ATG101 – Autophagy-related protein 101
ATG13 – Autophagy-related protein 13
ATG14L – Autophagy-related protein 14-like
ATG5/7/12/16L1 – Specific autophagy-related genes involved in autophagy pathways
ATG9 – Autophagy-related protein 9
ATP – Adenosine triphosphate
AVs – Autophagic Vesicles
BCL2L13 – BCL2-like protein 13
BDNF – Brain-Derived Neurotrophic Factor
Becn1 – Beclin-1
BLA – Basolateral Amygdala
Bsn – Bassoon, an active zone scaffolding protein
cAMP – Cyclic Adenosine Monophosphate
CASM – Conjugation of ATG8 to Single Membranes
cDNA – Complementary DNA
CHIP – Carboxyl terminus of HSC70-interacting protein
CHMP4B – Charged multivesicular body protein 4B
CMA – Chaperone-mediated autophagy
CNS – Central Nervous System
CRF – Corticotropin-Releasing Factor
DA – Dopamine
DCTN1 – Dynactin subunit 1 (p150^Glued^)
DCV – Dense-Core Vesicle
DIC – Dynein Intermediate Chain
DNABJ1 – Heat shock protein 40 (Hsp40) also known as DNABJ1
DUSP1/MKP1 – Dual Specificity Phosphatase 1
DYNC – Dynein Complex
EAL – Endosome-Autophagosome-Lysosome (pathways)
EE – Early Endosomes
EndoA – Endophilin A
ER – Endoplasmic Reticulum
ER-phagy – Endoplasmic reticulum–specific autophagy
ERK – Extracellular Signal-Regulated Kinase
ESCRT – Endosomal sorting complex required for transport
EVs – Extracellular Vesicles
FAD – Familial Alzheimer’s Disease
FAM134A/RETREG2 – ER-phagy receptor FAM134A/RETREG2
FAM134B/RETREG1 – ER-phagy receptor FAM134B/RETREG1
FAM134C/RETREG3 – ER-phagy receptor FAM134C/RETREG3
FIP200 – Focal adhesion kinase family-interacting protein of 200 kDa
FKBP8 – FK506-binding protein 8
FRET – Förster Resonance Energy Transfer
FYCO1 – FYVE and Coiled-Coil Domain-Containing Protein 1
GABA – Gamma-Aminobutyric Acid
GANE – Glutamate Amplifies Noradrenergic Effects

GAPs – GTPase-Activating Proteins
GCaMP8 – Genetically Encoded Calcium Indicator
GPCR – G-Protein-Coupled Receptor
GPR50 – G protein–coupled receptor 50
GTPase – Guanosine Triphosphatase
Gαi/o – Inhibitory G-alpha protein subunit
Gαs – Stimulatory G-alpha protein subunit
HMGB1 – High Mobility Group Box 1
HOPS – Homotypic Fusion and Protein Sorting Complex
Hsc70-4 – Drosophila Hsc70 variant
Hsc70/HSPA8 – Heat shock cognate protein 70 (HSPA8)
HSP – Heat shock protein
Hsp40 (DNABJ1) – Heat shock protein 40 (also known as DNABJ1)
IL-1β – Interleukin-1 beta
ILV – Intraluminal vesicles
IP – Immuno-Precipitation
JIP1 (MAPK8IP1/JIP1) – JNK-interacting protein 1
JIP3 – JNK-interacting protein 3 (also known as Sunday Driver/UNC-16)
JIP4 – JNK-interacting protein 4
JNK – c-Jun N-terminal Kinase
KFERQ – Pentapeptide motif for CMA substrate recognition
KIF5 – Kinesin family member 5 (Kinesin-1 heavy chain)
KLC-NE – Kinesin Light Chain (neuronal)
LAMP1 – Lysosome-associated membrane protein 1
LAMP2A – Lysosome-associated membrane protein 2A
LAMP2B – Lysosome-associated membrane protein 2B
LC – Locus Coeruleus
LC-BLA – Locus Coeruleus–Basolateral Amygdala (pathway)
LC-NE – Locus Coeruleus–Norepinephrine (system/neurons)
LC-PFC – Locus Coeruleus–Prefrontal Cortex (circuitry)
LC3 – Microtubule-associated protein 1 light chain 3
LC3B – Microtubule-associated protein 1 light chain 3 B
LC3B+ – Microtubule-associated protein 1 light chain 3 B positive
LDCV – Large Dense-Core Vesicle
LDELS – LC3-dependent Exosome-Like Structures
LIANA+ – Ligand–Receptor Interactions Analysis
LTD – Long-Term Depression
LTP – Long-Term Potentiation
MAO – Monoamine Oxidase
mTOR – Mechanistic target of rapamycin
mTORC1 – Mechanistic target of rapamycin complex 1
Munc13 – Unc-13/Munc13 protein
MVB – Multivesicular body
NA – Noradrenaline
NBR1 – Neighbor of BRCA1 gene 1
NDP52 (CALCOCO2) – Nuclear dot protein 52 (CALCOCO2)
NM – Neuromelanin
NMDARs – N-Methyl-D-Aspartate receptors
NMJ – Neuromuscular Junction
NREM – Non-Rapid Eye Movement
NSCs – Neural stem cells
OB – Olfactory bulb
OPTN – Optineurin
PE – Phosphatidylethanolamine

PFC – Prefrontal Cortex
PI(4,5)P2 – Phosphatidylinositol 4,5-bisphosphate
PI3P – Phosphatidylinositol 3-phosphate
PKA – Protein Kinase A
PLEKHG5 – Pleckstrin Homology and RhoGEF Domain Containing G5
PSEN1 – Presenilin 1
Psmb4 – Proteasome subunit beta type 4
RAB10 – Ras-related protein Rab-10
Rab26 – Rab26, a small GTPase involved in targeting synaptic vesicles to phagophores
RAB27A –a small GTPase involved in exocytosis
Rab7 – Ras-related protein Rab7
RAB8 – Ras-related protein Rab-8
RE – Recycling Endosomes
RILP – Rab-Interacting Lysosomal Protein
SAP102/Dlg3 – Synapse-associated protein 102/Discs large homolog 3
SARs – Selective autophagy receptors
Sec22 – a SNARE protein of the Sec22 family
Sec22b – an R-SNARE involved in unconventional secretion and secretory autophagy
SEC62 – EC62, an ER-phagy receptor
SIPA1L2 – signal induced proliferation associated 1 like 2
SNAP – Synaptosomal-associated protein
SNAP23 – Synaptosomal-Associated Protein 23
SNAP29 – Synaptosomal-Associated Protein 29
SNAP47 – Synaptosomal-Associated Protein 47
SNAPIN – SNAP-associated protein
SNARE – Soluble N-ethylmaleimide-sensitive factor attachment protein receptor
SPA – Secretory Pathway Autophagy
SQSTM1/p62 – Sequestosome 1
STX1 – Syntaxin 1
STX17 – Syntaxin 17
STX18 – Syntaxin 18
STX3 – Syntaxin 3
STX4 – Syntaxin 4
STX7 – Syntaxin 7
TAX1BP1 – Tax1 binding protein 1
TFRC – Transferrin Receptor
TH – Tyrosine Hydroxylase
TRIM – Tripartite Motif-containing Protein
TTX – Tetrodotoxin
Ub – Ubiquitin
α1AR – Alpha-1 Adrenergic Receptor
α2AR – Alpha-2 Adrenergic Receptor
β2AR- Beta-2 Adrenergic Receptor